

MASTER'S THESIS

---

# Phase Behavior of Ionic Colloidal Crystals

---

*Author:*

Dennis VAN DEN BERG

*Supervisor:*

Dr. René VAN ROIJ



UTRECHT UNIVERSITY  
INSTITUTE FOR THEORETICAL PHYSICS





# Abstract

Based on DLVO theory, and using Madelung calculations and Helmholtz free energy models, we studied which crystalline structures are formed out of a colloidal fluid consisting of binary, oppositely charged particles suspended in an electrolyte. Characterized by colloidal sizes and charges, screening length, mixing ratio, packing fraction and temperature, the system has a very large parameter space, which we have been able to chart for a considerable part. For the zero-temperature ground state we found a large variety of stable crystal structures, several of which have not been predicted before. In particular, its phase diagram for size ratio 0.65 can be considered completely new. Finite-temperature phase diagrams reveal the same stable structures as predicted by Monte Carlo simulations, although we find a quantitative discrepancy in the temperature dependence. Finally, we briefly discuss potential improvements of our model and the relevance of this research for other fields.



# Acknowledgements

First of all, I would like to thank my supervisor René. Not only did he provide me with insightful comments and ideas in cases where I didn't really see how to proceed, he also has an inspiring way of talking about doing research itself. I remember numerous times that I left his room feeling far more enthusiast and reassured than I entered, although - I have to admit - this feeling would not always stay indefinitely.. To be honest, during this research project I have seen my motivation reach highs but certainly also a number of quite deep lows. Realizing that I have not shown myself from my best side in this respect, partly because of other things that I have been doing (let's call it a sub-optimal choice of priorities), I also want to genuinely thank René for his patience.

Furthermore, I like to thank Antti-Pekka, for sharing his Madelung energy program with me, which served as a basis for my first calculations, Markus, for his help with one particular theoretical part of this thesis, Jaap, for reading and commenting on the preliminary version without even being asked to, and Joke, for giving me some very useful pieces of advice.

In particular, I really must thank Nard, who reminded me again of the meaning of altruism, since he spent a lot of his time on helping me make progress.

The question remains what would have become of this thesis if it hadn't been for André, whom I owe a very great deal of gratitude for sacrificing a considerable amount of his spare time and energy. Not only did he manage to persuade me into making a number of tough decisions, I suspect that he has also taught me more about myself than I could have foreseen.

Finally, I am very glad to have many friends who have often been curious how things were going, who encouraged me and who have given me practical advice. I am not going to mention names, because those I am addressing will know who I mean: house mates, fellow board members, my high school friends, study friends, etc. And last but not least, a special thank you to Berry and Marenne, who have kept up with complaints and grievances for so long.

Let me close off with something completely different, something I found out to be true, namely *Hofstadter's Law* [1]:

It always takes longer than you expect, even when you take into account Hofstadter's Law.

Dennis van den Berg  
Utrecht, April 16, 2009

# Contents

<b>1</b>	<b>Introduction</b>	<b>1</b>
1.1	Ionic Colloidal Crystals . . . . .	2
1.2	Previous research . . . . .	4
1.3	Scope of this thesis . . . . .	5
<b>2</b>	<b>Colloidal interactions</b>	<b>7</b>
2.1	The system . . . . .	7
2.2	Important and negligible effects . . . . .	8
2.3	DLVO theory . . . . .	9
2.3.1	Electrostatic double layer . . . . .	9
2.3.2	Interacting double layers . . . . .	13
2.4	Accuracy of DLVO potential . . . . .	14
<b>3</b>	<b>The Ground State</b>	<b>17</b>
3.1	Madelung energy . . . . .	17
3.2	Methods . . . . .	21
3.2.1	Crystal structures . . . . .	21
3.2.2	Numerical calculations . . . . .	21
3.2.3	Coexisting phases . . . . .	23
3.3	Results . . . . .	25
3.3.1	Phase diagrams for fixed size ratios . . . . .	25
3.3.2	Influence of parameters on phase behavior . . . . .	29
3.3.3	Comparison to other research . . . . .	33
3.4	Conclusions . . . . .	35

<b>4</b>	<b>Finite temperature symmetric case</b>	<b>37</b>
4.1	Helmholtz free energies . . . . .	38
4.1.1	Crystal phase . . . . .	39
4.1.2	Fluid phase . . . . .	44
4.2	Methods . . . . .	50
4.2.1	Relevant parameters . . . . .	50
4.2.2	Lindemann criterion . . . . .	51
4.2.3	Common Tangent Construction . . . . .	52
4.3	Results and discussion . . . . .	53
4.3.1	Mobility of single colloids . . . . .	54
4.3.2	Gas-liquid binodal . . . . .	56
4.3.3	NaCl-CsCl boundary in $K - Q$ diagram . . . . .	58
4.3.4	Phase diagrams in $\eta - T^*$ plane . . . . .	61
4.3.5	CsCl-CuAu phase transition . . . . .	64
4.3.6	Variable cell volume . . . . .	65
4.4	Conclusions . . . . .	67
<b>5</b>	<b>Summary and outlook</b>	<b>71</b>
5.1	Summary . . . . .	71
5.2	Future research . . . . .	72
5.3	Potential applications . . . . .	73
<b>A</b>	<b>Notations and symbols</b>	<b>75</b>
A.1	Notations . . . . .	75
A.2	Symbols . . . . .	75
<b>B</b>	<b>Mathematical identities and special functions</b>	<b>79</b>
B.1	Identities . . . . .	79
B.2	Special functions . . . . .	79
<b>C</b>	<b>Derivations</b>	<b>81</b>
C.1	Solving the spherically symmetric linear Poisson-Boltzmann equation . . . . .	81
C.2	Partition function derived from microscopic level . . . . .	81
C.3	Symmetric version of Ffluid3 . . . . .	83



---

C.4 Truncated Boltzmann factor . . . . .	85
C.5 Better Ansatz . . . . .	86
<b>D Mansoori potential</b>	<b>89</b>



# Chapter 1

## Introduction

In 1861 the Scottish scientist Thomas Graham was working on a suspension that was characterized by a low diffusion rate and lack of crystallinity. From these characteristics he estimated that the sizes of the individual components of the system were between a nano- and a micrometer. He named these particles ‘colloids’, after the word ‘ $\kappa\omicron\lambda\lambda\alpha$ ’, meaning ‘glue’ in Greek. To be precise, we define colloids today as particles with sizes in the nano- to micrometer range that are dispersed in a solvent, and that display Brownian motion due to collisions with the solvent molecules [2].

Colloid science describes a broad range of systems with particles of this kind dispersed in another substance. Solids dispersed in liquids (sols, or usually just called colloidal suspensions), liquids in liquids (colloidal emulsions), gasses in solids (colloidal foams), liquids or solids in gas (aerosols) are all colloidal dispersions. One can imagine that many biological and natural materials like blood, viruses or even muddy clay are categorized as colloidal materials. Industrial applications include paints, inks, glues and food products such as ice cream or chocolate milk, to mention a few.

From a fundamental point of view, colloidal suspensions can now be regarded as very nice model systems, in which multi-particle interactions and their large scale phase behavior can be studied quantitatively. Although these systems generally exhibit quite complex behavior, advances in experimental technologies and techniques have made it possible to tweak the system such that many unwanted effects are cancelled and interesting phenomena can be singled out. Or, alternatively, an even more complex system can be constructed from more complex components, displaying more complex behavior [3]. Of course theoretical tools and models have always been necessary companions of experiments and during the last few decades computer simulations have also become increasingly important in colloid science.

Contrary to what Graham observed in the 19<sup>th</sup> century, it is precisely the crystallization, occurring in some colloidal suspensions, that has become one of the most interesting aspects of colloid science. In fact, that is what this whole thesis is about.

## 1.1 Ionic Colloidal Crystals

This thesis will focus on specific systems called Ionic Colloidal Crystals (ICCs) of oppositely charged particles. ICCs are crystalline structures, formed out of a binary mixture of colloidal particles, that are suspended in a solution of salt ions. Each colloidal species consists of approximately monodisperse (equally sized) spherical particles, but both species need not have particles of the same size or absolute charge, as long as those charges are of opposite signs. In most cases the system is only partly crystallized, such that the crystals still coexist with the original colloidal suspension, which can be in a gas, liquid or fluid phase.

ICCs are stabilized by the long range attractions between unlike particles, but their precise configuration is of major importance for their stability, because the like-charge repulsions will, in most circumstances, have large contributions as well.

Crystal structures being formed this way are often the colloidal analogues of atomic scale structures that we know from normal salts, metals, alloys, etc., but obviously there are some major differences. We are investigating colloids in the micrometer size range, so the lattice spacings of their crystals are typically 4 orders of magnitude larger than those of ordinary crystals. This has the benefit that they can be observed in real space and time, for example using confocal microscopy. Also, for these large lattice spacings, Bragg reflection is manifested in the visible wavelength regime.

The interaction potential of these charged colloids has a spherical symmetry, which is definitely not the case for covalently bonded atoms in metals, for instance. Quantum effects can be considered irrelevant, again due to the large sizes. In this respect the interactions look more like ordinary ionic bonds, hence the name ICC.

The salt ions in the solution form a charged layer around each colloid that reduces the effective colloidal charge and change the shape of the interaction potential. In chapter 2 it becomes clear that this surrounding layer ensures charge neutrality for the whole system. This implies that all the colloids together, i.e without the ions, can have an excess charge while still giving a stable crystal structure, which is by the way not the case in atomic ionic crystals. The latter require approximately equal amounts of positive and negative charges in order for the crystals not be driven apart by their long-range unscreened Coulomb interaction potentials.

ICCs can be tuned in many different ways. The relative particle sizes of both colloidal species have large implications for the packing and entropy of the system, whereas the charges of the different components influence the interactions at larger distances. Note that these are essentially continuous parameters, contrary to what is the case in atomic crystals. Furthermore, the range at which these interactions act is governed by the salt concentration. Changing the interaction strength turns out to be equivalent to changing the temperature (see chapters 2 and 4) and has also great consequences for the phase behavior, but this is of course true for all chemical systems.

It is not surprising that this large parameter space has enough room for a whole variety of crystal structures [4], that could pave the way to new applications. One of the most

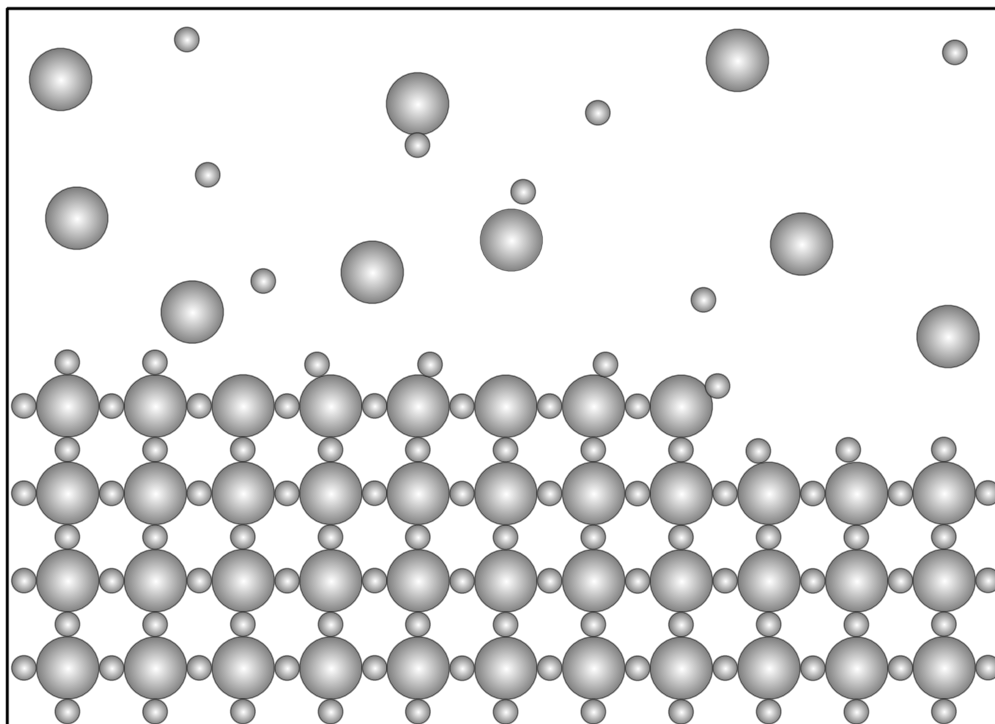


Figure 1.1: A schematic 2-dimensional slice of an Ionic Colloidal Crystal coexisting with a colloidal gas phase. The colloids carry opposite charges and are suspended in a solution of salt (not depicted here). This particular crystal structure has stoichiometry (i.e. large vs. small ratio) 1 : 3 and corresponds to a (100) intersection of a  $\text{ReO}_3$  lattice. Observe that it is dense-packed, since all neighbors are touching, and nevertheless it has a fairly low packing fraction.

promising is the fabrication of 3D photonic crystals with a complete photonic band gap in the optical wavelengths [5, 6]. These photonic band gap materials can be considered the optical analogues of electronic semiconductors and will be of great interest to both fundamental and applied research. For example, one can think of the development of ultrafast optical switches and miniature lasers.

Because ICCs have such a large tunability range, it becomes much easier to produce self-assembled structures like the one displayed in figure 1.1, that possess large surface areas and at the same time provide small diffusion lengths for liquid or gaseous substances filling the space in between the colloids. These crystals could be used as substrates in the field of chemical catalysis, as drug releasing systems in pharmaceuticals or for filtering purposes.

## 1.2 Previous research

The topic of Ionic Colloidal Crystals is really quite new. Until a few years ago, experiments in this area were either done on binary colloidal systems displaying hard-sphere-like [7, 8, 9], long-range repulsive [9, 10], short-range attractive [10, 11] and dipolar [9] interactions or, in case of long range attractive interactions, failed to generate stable colloidal crystals because of heterocoagulation [12]. This means that contact forces are so big that, once in contact, individual particles with opposite charges stick onto each other to form irreversible highly-disordered aggregates. The lack of mobility in such an aggregate then prevents individual particles to rearrange themselves into a crystalline structure.

Also, due to the many procedures in the synthesis of the colloids, the charges on the colloidal surfaces are not so easy to control precisely, especially when dealing with a binary mixture of oppositely charged particles [13]. This makes it even harder to obtain a stable ICC, because larger charges are more likely to cause heterocoagulation.

In 2005 however, there was a breakthrough on these issues, according to publications by Leunissen *et al.* [13] and, to a lesser extent, Bartlett & Campbell [14]. The latter managed to produce self-assembled ICCs out of weakly-charged colloids of different sizes, at high density. By increasing the charges they showed that the crystal structures could be transformed from a random hexagonal close-packed crystal (rhcp, also observed in binary hard-sphere experiments), via a CsCl lattice structure, to a NaCl lattice structure.

Leunissen *et al.* did several experiments on ICCs, both for equally sized particles and with size ratio 0.31. For the equally sized system they also found the CsCl structure and they arrived at the rhcp structure by adding salt, thus decreasing the screening length. Furthermore, applying an electric field proved that the crystallization behavior could be reversed. In the case of dissimilarly sized particle species some new structures, called  $LS_6$  and  $LS_8^1$ , were found. When the smallest particles were left almost uncharged, this resulted in a phase coexistence of the NaCl and NiAs structures.

The same article showed the results of extensive Monte Carlo computer simulations and theoretical calculations of Madelung energies. These results predicted a large variety of known and unknown crystal structures, among which the experimentally observed ones. An important part of our research here is based on this kind of Madelung energy calculations and we will therefore compare many of our own results to the article by Leunissen *et al.* and to other publications by Hynninen *et al.* [15, 16, 17].

In the same year a PhD thesis came out by G.R. Maskaly, who had been using a combination of Madelung energy calculations, Brownian Dynamics and Monte Carlo simulations to study ICCs theoretically [18, 19]. In addition, some preliminary experiments seemed to show crystalline behavior, but only very locally.

---

<sup>1</sup>We adopt the notation  $LS_k$  for a specific crystal structure with stoichiometry  $1 : k$ , meaning that it has  $k$  colloids of the smallest species (S) for each one of the largest species (L). In the special case that both colloidal species have equal size we continue to use this notation, since the structure itself remains of course the same.

Besides the above publications, no other major theoretical research on ICCs has been performed that is relevant to our main topic of investigation, as far as we are aware.

## 1.3 Scope of this thesis

The goal of this thesis is to set up a theoretical model for the thermodynamic energies of binary colloidal crystals and mapping a large part of their phase behavior, that takes place in a fairly large parameter space. The idea is that this model will enable us to calculate pretty quickly, i.e. much faster than through Monte Carlo or Molecular Dynamics computer simulations, which crystal structures are (meta-)stable<sup>2</sup> in a certain region of parameter space. Since we are only investigating the bulk phase behavior, we will not take into account any interfacial or nucleation effects.

The main part of this thesis is divided into 3 chapters, of which the first (chapter 2) is purely theoretical in nature and the others (chapters 3 and 4) consist of both theory and numerical calculations and actually contain newly found results. It is structured in such a way that each chapter builds upon the previous one, starting simple and extending the theory step by step. This also enables us to compare intermediate results to previous research, as was mentioned in section 1.2.

In chapter 2 we will give a clear physical description of the system that we are investigating and the different interactions between individual particles. We will give a short derivation of the DLVO pair potential, which will be used throughout the rest of this thesis.

Chapter 3 deals with the special case of vanishing temperature and pressure, which we will call the ground state of the system. This implies neglecting all effects of entropy and considering only hard-sphere repulsions and electrostatic interactions. The stability of crystal structures is therefore determined from their Madelung energies. We impose no further restrictions on the symmetry of the system, for example by fixing size or charge ratios (as is done in chapter 4).

In chapter 4 we extend the theory to incorporate entropic contributions as well, but restrict ourselves to what we call the symmetric system, which constitutes of equally sized, equally (but oppositely) charged particle species, having equal particle numbers. In order to calculate the Helmholtz free energies (in the  $NVT$  ensemble), we devise a cell-like model for the crystal phase, whereas for the fluid we use thermodynamic perturbation theory. In fact it can be considered the most important part of this research project, since it is investigated in most detail.

---

<sup>2</sup>By ‘stable’ I do not mean the same thing as some people [12] use as a convention, i.e. stable versus unstable structures corresponding to regular versus irregular aggregates of colloidal particles respectively. As a matter of fact I define a stable crystal to be the energetically most favored structure, with the lowest free energy. Correspondingly, unstable implies that the crystal free energy is higher than that of the suspension itself (i.e. the crystal tends to fall apart), and metastable means that the free energy is in between that of the suspension and the stable crystal.

The final chapter summarizes the applied theories/models and lists the most important conclusions of this research project. It concludes by giving a short outlook on future research on this topic.

As a last practical remark, we want to note that there are some comments about notations and symbols in appendix A, which might prove useful in reading the next chapters.



# Colloidal interactions

Before diving into the theory explaining the interaction potential between charged colloids, we will first give a proper description of the system and some of the assumptions that we make.

The interaction potential is then derived using the solution of the linearized Poisson-Boltzmann equation, followed by a brief discussion about its relevance and accuracy.

## 2.1 The system

As mentioned in chapter 1, the system we describe consists of 2 species of spherical colloids, carrying opposite charges and suspended in a salty solution. The particles are usually produced from synthetic materials such as polymethylmethacrylate (PMMA) or silica, sterically stabilized or coated with an extra layer in order to make them behave like nearly perfect hard spheres [20]. Fabrication methods allow for low polydispersities, with size ranges usually varying less than 5% [13, 14].

The solution of salt ions has a two-fold purpose. In the first place, the colloidal charges are screened by the ions surrounding them. We will say more about this in the next section. Perhaps more interestingly, *Leunissen et al.* found that adding salt to a system of the right materials can be used very conveniently to change the surface charge of the particles. This way it has become relatively easy to generate differently or even oppositely charged species of colloids. This charge inversion technique is not very accurate, because each batch of particles turns out to be different due to the many steps in the synthetization process and also because the charges are not measured during the time that salt is being added.

In our calculations we consider the colloids to be perfect monodisperse hard spheres that are impenetrable to ions and assume that the majority of their charges are distributed homogeneously over the surface, although the theory would not be fundamentally different if charges were located inside the colloidal volumes. Due to electrostatic and thermodynamic

interactions each colloid is surrounded by a double layer of salt ions, consisting of a very thin Stern layer of oppositely charged ions that adhere to the surface and a more dilute layer of both ion species. For simplicity salt ions are assumed to be monovalent and the solution contains equal concentrations of positive and negative ions.

We denote the particle sizes by  $a_A$ ,  $a_B$  and their charges as  $+Z_A e$ ,  $-Z_B e$ , where each of the two species is represented by a subscript  $A$  or  $B$ . Charges are always chosen to be of opposite sign, such that charge numbers  $Z_A$  and  $Z_B$  remain positive. Needless to say,  $e$  is just the elementary charge.

$Z_A$  and  $Z_B$  are in fact the colloidal charge numbers including all the ions attached to the surface, so the Stern layer is considered as a part of the colloid, for that matter. Later on we will see that it is more convenient to represent the colloids as point particles with a certain effective charge (not for the hard-sphere part of the interaction, of course).

The dilute ion layer has a thickness measured by the Debye screening length  $\kappa^{-1}$ , which is closely related to salt concentration and temperature. The meaning of this parameter becomes clear from subsection 2.3.1. To be precise,  $\kappa^{-1}$  can be expressed as

$$\kappa^{-1} \equiv (8\pi\lambda_B n v^2)^{-\frac{1}{2}}, \quad (2.1)$$

where  $n$  is the salt concentration,  $v$  the ion valence (which will later be set to  $v = 1$  because we assume monovalent ions) and  $\lambda_B$  the Bjerrum length

$$\lambda_B \equiv \frac{e^2}{4\pi\epsilon k_B T}, \quad (2.2)$$

the latter being a (temperature dependent) measure for the electrostatic interaction strength, and  $\epsilon$  the electric permittivity. In other words: a solvent with low salt concentration, or equivalently, a system with high temperature, gives little screening of the colloidal charges, which implies long range interactions and therefore small  $\kappa$ .

The particles that we investigate are approximately micrometer sized, which makes the ion sizes essentially negligible, as there is a difference of about 4 orders of magnitude. Charge numbers are roughly  $10^2$ . The precise value of this parameter is highly important for coagulation, together with temperature. Furthermore, we consider screening values in the range of  $1 \lesssim 2\kappa a \lesssim 15$ , thus producing relatively short ranged interactions.

## 2.2 Important and negligible effects

Not surprisingly, most experiments have been done under the influence of gravity and this can have a significant effect on the system. Besides some practical benefits, such as higher crystallization rates due to sedimentation, it might also result in different crystal structures being formed than in the case without gravity. For instance, the broken symmetry in the gravitational direction might cause layering or other anisotropic effects. Additionally, gravitational forces could keep a dense structure in a certain low energy configuration that might

not necessarily be the ground state but only a local minimum. Experiments in microgravity, for example, show that hard-sphere systems at high densities slowly convert their structure from rhcp to fcc [21], which is indeed predicted by the theory, but this behavior seems to be restricted when gravity plays a role and thermal energies are not sufficiently high to overcome this. In our calculations we assume that gravity plays no role whatsoever and in practice one can achieve this by simply matching the densities of solvent and colloidal material.

A second kind of forces that we neglect are Van der Waals interactions. These are caused by dipoles fluctuating in synchrony with one another and can have relatively long ranges. In experimental setups one can minimize them by matching not the densities, but this time the refractive indices of solvent and colloid. This means that dielectric permittivity is fairly constant throughout the system, such that the contribution of induced or fluctuating dipoles to the interaction potential will be practically zero in this dielectric continuum.

Furthermore, we assume that the only kinetic phenomenon playing a role in the system is Brownian motion, caused primarily by colloids colliding with each other and to a lesser extent by solvent molecules acting on colloids. Under normal circumstances this motion can even be observed visually, using confocal microscopy [13]. One could argue that this is the driving force behind the formation of colloidal crystals, because without it dense amorphous structures would not be able to rearrange themselves into the thermodynamically most favorable configuration. We will discuss these thermal motions somewhat further in chapter 4, when entropy is incorporated into the theory.

Other effects, such as small scale hydrodynamic flows due to colloids moving around, are said to be of no importance. In experiments one lets the suspension come to rest in order to form crystallites, which eventually can take hours, days or even months for sufficiently large patches of crystal [13, 14], so larger scale flows are irrelevant anyway.

## 2.3 DLVO theory

Our calculations in the next chapters will be based on a theory by Derjaguin, Landau [22], Verwey and Overbeek [23], the so called DLVO theory, which describes the interaction pair potential between charged spherical colloids suspended in a solution of salt ions. In this section we derive a part of this theory.

### 2.3.1 Electrostatic double layer

The shape of the dilute part of the electrostatic double layer, i.e. the concentrations of positive and negative salt ions as a function of the distance from the colloidal center, can be determined by solving the Poisson-Boltzmann equation and applying the correct boundary conditions. From this we will derive a Yukawa potential with the appropriate prefactor.

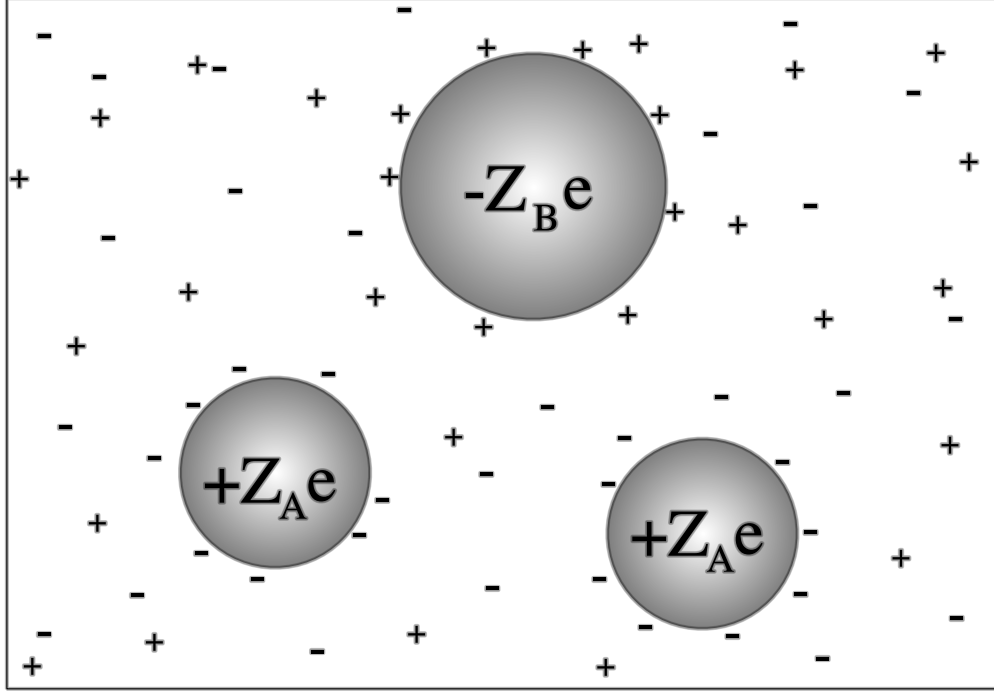


Figure 2.1: Double layers of salt ions around charged spherical colloids, which cannot be penetrated.

Using Maxwell's equations in a linear medium with permittivity  $\epsilon = \epsilon_r \epsilon_0$  assumed spatially constant

$$\nabla \cdot \mathbf{E} = \frac{\rho}{\epsilon}, \quad (2.3)$$

and the definition of the electric field  $\mathbf{E}$  in terms of the electrostatic potential  $\psi$

$$\mathbf{E} \equiv -\nabla\psi, \quad (2.4)$$

we arrive at the well-known Poisson's equation

$$\nabla^2\psi = -\frac{\rho}{\epsilon}, \quad (2.5)$$

which holds for a general charge distribution  $\rho[\mathbf{r}]$ .

Whereas inside the colloid we imposed that the charges are fixed and cannot move, outside we have the salt ions floating around under the influence of the local potential, which is again generated by the charge distribution. Since the (theoretical) colloids we describe are not penetrable, all colloid-ion interactions will take place at  $r > a$  and we will therefore disregard the precise charge distribution in the region  $r \leq a$ . Instead, it is sufficient to assume that the charge density inside the colloid has a spherical symmetry, making the whole distribution spherically symmetric:

$$\rho[\mathbf{r}] = \begin{cases} \text{fixed} & \text{for } |\mathbf{r}| \leq a \\ \rho_+[|\mathbf{r}|] - \rho_-[|\mathbf{r}|] & \text{for } |\mathbf{r}| > a. \end{cases} \quad (2.6)$$

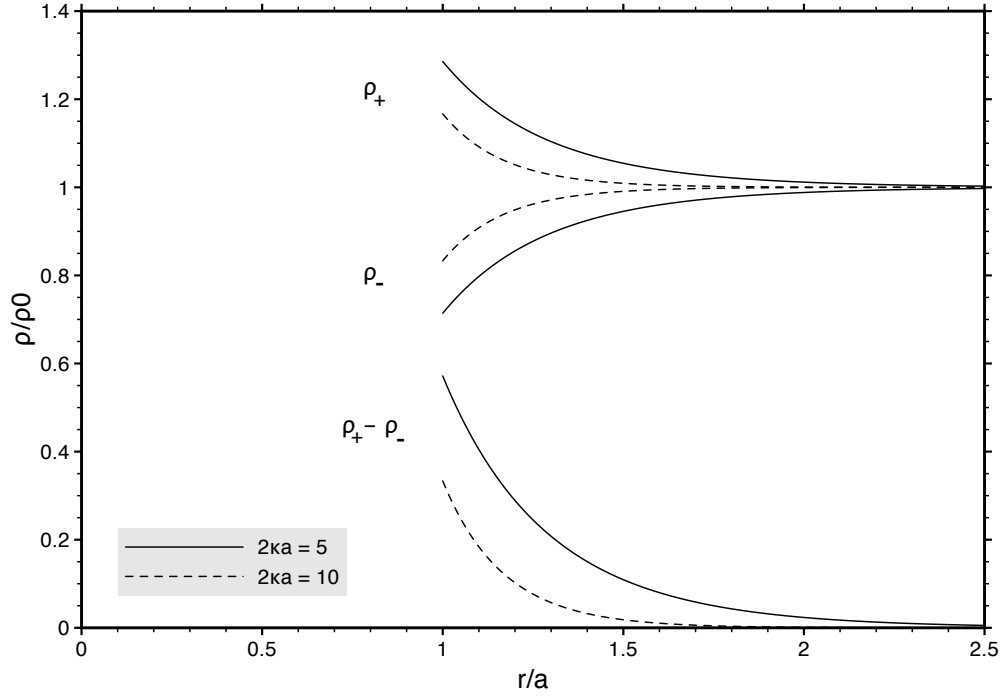


Figure 2.2: Charge densities  $\rho_+$ ,  $\rho_-$  and excess charge density  $\rho_+ - \rho_-$  in the double layer surrounding a negatively charged colloid with charge  $Q = -100e$ , as function of distance to the center. In the situation with higher screening (dashed lines) we see a faster decaying excess charge density than with lower screening (solid lines). Note that the screening length depends on temperature through the relation  $\kappa^{-1} \propto T^{1/2}$ . The normalization constant  $\rho_0$  depends on  $\kappa$ , so comparing the absolute charge densities for different  $\kappa$  is not very useful in this diagram. All charge densities have been computed using the linearized PB equation and, quite conveniently, in this linear approximation the electrostatic potential  $\psi(r)$  is proportional to  $-(\rho_+ - \rho_-)$ , as follows from equation (2.15). Integrating  $\rho_+ - \rho_-$  gives a total excess charge of  $-Q$  according to equation (2.16), thereby satisfying charge neutrality.

Here, the local charge densities  $\rho_+$ ,  $\rho_-$  depend on the electrostatic potential according to a Boltzmann distribution:

$$\rho_{\pm} = n_{\pm}^0 v_{\pm} e \exp \left[ \frac{\mp v_{\pm} e \psi}{k_B T} \right], \quad (2.7)$$

with  $v_+$ ,  $v_-$  the valencies of the positive and negative ions respectively, and  $n_+^0$ ,  $n_-^0$  denoting the average ion densities of the solution, i.e. describing the homogeneous ion distributions in absence of or far away from colloidal charges.

As mentioned in section 2.1 we only consider the case that the 2 species of salt ions have equal valencies and their number densities are equal at large distances from the colloid ( $v_+ = v_- \equiv v$ ;  $n_+^0 = n_-^0 \equiv n$ ), such that combining the previous equations leads to the nonlinear Poisson-Boltzmann equation:

$$\nabla^2 \psi = \frac{2nve}{\epsilon} \sinh \left[ \frac{ve\psi}{k_B T} \right]. \quad (2.8)$$

For small  $\psi$  we may approximate the sinh-function in order to obtain a linearized PB differential equation that can be solved analytically:

$$\nabla^2 \psi \approx \kappa^2 \psi, \quad (2.9)$$

with inverse Debye screening length

$$\kappa = \sqrt{\frac{2ne^2 v^2}{\epsilon k_B T}}, \quad (2.10)$$

which corresponds to the definition of  $\kappa$  in equations (2.1) and (2.2).

As we show in appendix C.1, it is easy to derive the solution of equation (2.9) for a spherically symmetric system. Additionally, requiring  $\lim_{r \rightarrow \infty} \psi[r]$  to be finite, for obvious physical reasons, we find a Yukawa potential:

$$\psi[r] = c \frac{\exp[-\kappa r]}{r}. \quad (2.11)$$

To determine the value of the prefactor  $c$ , we write down a second (Von Neumann) boundary condition. By subsequently using spherical symmetry, Gauss's theorem (see appendix B) and Poisson's equation (2.5), we obtain:

$$\begin{aligned} \lim_{r \downarrow a} \frac{\partial \psi}{\partial r}[r] &= \frac{1}{4\pi a^2} \oint_{S_{\text{colloid}}} \nabla \psi[r] \cdot d\mathbf{s} = \frac{1}{4\pi a^2} \int_{V_{\text{colloid}}} \nabla^2 \psi[r] d\mathbf{r} = -\frac{1}{4\pi \epsilon a^2} \int_{V_{\text{colloid}}} \rho[\mathbf{r}] d\mathbf{r} \\ &= -\frac{Q}{4\pi \epsilon a^2}, \end{aligned} \quad (2.12)$$

where  $Q \equiv Ze$  is the colloidal charge.

Combining the last two equations finally leads us to the desired expression:

$$\boxed{\psi[r] = \frac{Q}{4\pi\epsilon} \frac{\exp[\kappa a]}{1 + \kappa a} \frac{\exp[-\kappa r]}{r} \quad \text{for } r > a.} \quad (2.13)$$

From this result we see that each finite-sized colloid can be represented as a point particle with effective charge:

$$Q' \equiv Q \frac{\exp[\kappa a]}{1 + \kappa a}, \quad (2.14)$$

such that this point charge  $Q'$  yields the same electrostatic potential as a colloid with charge  $Q$  and radius  $a$ , at least in the region  $r > a$ .

Once the electrostatic potential is known, it is straightforward to calculate the (linearly approximated) charge density

$$\rho = -\epsilon \nabla^2 \psi \approx -\epsilon \kappa^2 \psi, \quad (2.15)$$

using equations (2.5) and (2.9). As an aside, we integrate this charge density, yielding:

$$\begin{aligned} \int_{|\mathbf{r}|>a} \rho[\mathbf{r}] d\mathbf{r} &\approx -\epsilon \kappa^2 \int_{|\mathbf{r}|>a} \psi[\mathbf{r}] d\mathbf{r} = -\epsilon \kappa^2 \int_a^\infty 4\pi r^2 \left( \frac{Q}{4\pi\epsilon} \frac{\exp[\kappa a]}{1 + \kappa a} \frac{\exp[-\kappa r]}{r} \right) dr \\ &= -Q \frac{\kappa^2 \exp[\kappa a]}{1 + \kappa a} \int_a^\infty r \exp[-\kappa r] dr = -Q, \end{aligned} \quad (2.16)$$

with partial integration in the last step showing that the integral nicely cancels its prefactor. This means that in the linear approximation the charges on a colloidal particle exactly match the excess charge in the oppositely charged layer around it. In fact, this property of charge neutrality is a direct consequence of the boundary condition in equation (2.12).

A plot of the resulting charge densities  $\rho_+$  and  $\rho_-$ , based on the above solution of the linearized PB equation, can be seen in figure 2.2). Close to the colloidal surface there is a large excess charge density  $\rho$  that decays with distance, in a Yukawa-like fashion.

We notice that  $\kappa$  can be considered as a measure for screening. A larger  $\kappa$  implies a quicker decay of  $\psi[r]$  (or equivalently:  $\rho$ ) and therefore a shorter range of the potential. In other words, the counterions are concentrated in a thinner layer around the colloid. This is why we already called  $\kappa$  the inverse screening length. Obviously it depends on temperature. At higher temperatures the larger entropy associated with this drives the counterions further away, such that they are distributed more evenly over space. The balance of electric and entropic forces is maintained that way.

### 2.3.2 Interacting double layers

The interaction between two spherical double layers was first described in detail by Derjaguin & Landau [22] and Verwey & Overbeek [23] during the 1940's. We refer to these two

publications for a thorough derivation of the so called DLVO potential energy:

$$\beta V_{ij}[r] = \begin{cases} Z_i Z_j \lambda_B \frac{\exp[\kappa(a_i + a_j)]}{(1 + \kappa a_i)(1 + \kappa a_j)} \frac{\exp[-\kappa r]}{r} & \text{for } r \geq a_i + a_j \\ \infty & \text{for } r < a_i + a_j \end{cases}, \quad (2.17)$$

which has been widely used in colloid science ever since. Here, we already added the hard sphere potential to prevent overlapping colloids at  $r < a_i + a_j$ . This is the expression that we will continue to apply in the rest of this thesis.

In fact, equation (2.17) is identical to the potential energy of a point charge  $Q'_j$  situated in the one-particle Yukawa potential  $\psi_i[r]$  generated by a point charge  $Q'_i$ :

$$V_{ij}[r] = Q'_j \psi_i[r] = \frac{Q'_i Q'_j}{4\pi\epsilon} \frac{\exp[-\kappa r]}{r}, \quad (2.18)$$

under the assumption that the potential  $\psi_i[r]$  is not affected by point charge  $Q'_j$ . This similarity is quite remarkable, since this assumption does not necessarily hold for this two-particle system, certainly not in case of approximately similar charges.

As a final comment, we note that a vanishing  $\kappa$  causes the DLVO potential indeed to reduce to the unscreened  $1/r$  Coulomb potential, because of  $Q' \rightarrow Q$  and  $\exp[-\kappa r] \rightarrow 1$ .

## 2.4 Accuracy of DLVO potential

In subsection 2.3.1 we imposed the Debye-Hückel approximation which is used to linearize the Poisson-Boltzmann equation. Considering only monovalent salt ions is one of the restrictions that increases the accuracy of this approximation. On the other hand, it also requires  $\beta\psi$  to be small, so it becomes inaccurate particularly at low temperatures and high densities. This is something we should keep in mind when applying the DLVO potential to colloidal crystals.

According to previous research however, the DLVO potential appears to give good results for like charged particles, but the question remains how accurate it is for the case of oppositely charged ones [13]. For alternative descriptions of the colloidal pair interaction we refer to HHF theory [24] or the Wiese-Healy model [25], that also look deeper at dissimilarly charged colloids.

Furthermore, it is reasonable to ask whether it is sufficient to describe the system solely as the sum of pair interactions. If multi-particle interactions cannot be neglected, the ion cloud around a certain particle is affected by the charge on a neighboring particle, which again influences other nearby particles. This means that the DLVO pair potential would be a bad approximation in such situations. In reality, one should add terms for the interaction of 3, 4, etc particles, but this becomes incredibly difficult, certainly for 2 different particle species. Investigating this kind of problems using numerical techniques such as PB-equation solvers,



has shown that multi-particle interactions can in fact play a role in certain circumstances, especially for  $\kappa a \ll 1$  [26, 27]<sup>1</sup>. To prevent this, we will focus our calculations on larger screening values.

---

<sup>1</sup>Reference [27] later turned out to be based on an invalid method, so its results are in fact highly questionable [28].



## The Ground State

Now that we have discussed colloidal interactions and looked closer at the DLVO potential in chapter 2, it is time to proceed to the actual research part of this thesis and apply the interaction potential to the binary colloidal mixture as a whole, in order to determine its phase behavior.

As said before, we want to start off slowly and first restrict ourselves to the ground state of the system, i.e. the special case for which the temperature  $T$  and osmotic pressure  $p$  are both vanishing.

### 3.1 Madelung energy

In the ground state the system behavior is governed only by electrostatic interactions and hard-sphere repulsions between colloidal particles, while entropy plays no role due to the requirement that  $T = 0$ . This also manifests itself in the fact that Helmholtz free energy  $F \equiv U - TS$  and Gibbs free energy  $G \equiv U - TS + pV$  are automatically reduced to  $U = F = G$ , where  $U$  is the total electrostatic energy of the system.

We consider  $N_A$  colloids of type  $A$  (radius  $a_A$ , charge  $Z_A e$ ) and  $N_B$  colloids of type  $B$  (radius  $a_B$ , charge  $Z_B e$ ) in an electrolyte characterized by screening length  $\kappa^{-1}$  and Bjerrum length  $\lambda_B$ . The particles possess no thermal energy and are therefore located at fixed positions in space, having no additional degrees of freedom. As one can imagine in a system of oppositely charged particles, the total potential energy depends greatly on their specific configuration.

In order to calculate the potential energy of the system, we will apply the DLVO pair potential that we recall from the previous chapter:

$$\beta V_{ij}[r] = \begin{cases} Z_i Z_j \lambda_B \frac{\exp[\kappa(a_i + a_j)]}{(1 + \kappa a_i)(1 + \kappa a_j)} \frac{\exp[-\kappa r]}{r} & \text{for } r \geq a_i + a_j \\ \infty & \text{for } r < a_i + a_j \end{cases} \quad (3.1)$$

and apply it to different crystalline structures. Here, we adopt the notation  $Z_i = Z_A, Z_B$  and  $a_i = a_A, a_B$  for  $i \in \mathcal{A}, \mathcal{B}$ . The total number of particles is denoted  $N \equiv N_A + N_B$ . At this point we also introduce some notations for the set of all particles, its subsets containing only the A- or the B-particles and the ones in the standard unit cell:

$$\mathcal{N} \equiv \{1, 2, \dots, N\} \quad (3.2)$$

$$\mathcal{A} \equiv \{i \in \mathcal{N} | \text{particle } i \text{ is of species A}\} \quad (3.3)$$

$$\mathcal{B} \equiv \{i \in \mathcal{N} | \text{particle } i \text{ is of species B}\} \quad (3.4)$$

$$\mathcal{U} \equiv \{i \in \mathcal{N} | \text{particle } i \text{ is in standard unit cell}\}, \quad (3.5)$$

where  $\mathcal{A}$ ,  $\mathcal{B}$  and  $\mathcal{U}$  have  $N_A$ ,  $N_B$  and  $n$  elements respectively. To complete this notation, the corresponding sets describing their positions are denoted by:

$$\{\mathbf{r}\}_{\mathcal{N}} \equiv \{\mathbf{r}_1, \mathbf{r}_2, \dots, \mathbf{r}_N\} \quad (3.6)$$

$$\{\mathbf{r}\}_{\mathcal{A}} \equiv \{\mathbf{r}_i | i \in \mathcal{A}\} \quad (3.7)$$

$$\{\mathbf{r}\}_{\mathcal{B}} \equiv \{\mathbf{r}_i | i \in \mathcal{B}\} \quad (3.8)$$

$$\{\mathbf{r}\}_{\mathcal{U}} \equiv \{\mathbf{r}_i | i \in \mathcal{U}\}. \quad (3.9)$$

The total energy  $U$  of a general configuration is just the sum of all electrostatic pair potentials:

$$U[\{\mathbf{r}\}_{\mathcal{N}}] \equiv \frac{1}{2} \sum_{i \in \mathcal{N}} \sum_{j \in \mathcal{N} \setminus \{i\}} V_{ij}[r_{ij}]. \quad (3.10)$$

For the particular case that all colloids are positioned at a crystal lattice  $\{\mathbf{R}\}_{\mathcal{N}}$  we define the Madelung energy  $U_M$  of the whole crystal [29]:

$$\begin{aligned} U_M \equiv U[\{\mathbf{R}\}_{\mathcal{N}}] &= \frac{1}{2} \sum_{i \in \mathcal{N}} \sum_{j \in \mathcal{N} \setminus \{i\}} V_{ij}[R_{ij}] \\ &= \frac{1}{2} \sum_{i \in \mathcal{A}} \sum_{j \in \mathcal{A} \setminus \{i\}} V_{AA}[R_{ij}] + \sum_{i \in \mathcal{A}} \sum_{j \in \mathcal{B}} V_{AB}[R_{ij}] + \frac{1}{2} \sum_{i \in \mathcal{B}} \sum_{j \in \mathcal{B} \setminus \{i\}} V_{BB}[R_{ij}] \end{aligned} \quad (3.11)$$

where we use the more convenient notations  $V_{AA}, V_{AB} = V_{BA}$  and  $V_{BB}$  for the pair potentials  $V_{ij}$  with  $i, j \in \mathcal{A}, \mathcal{B}$ . In principle the lattice is extending infinitely far in all directions, such that the summations are infinite as well. Therefore a more practical quantity will be the Madelung energy per particle:

$$u_M \equiv \frac{U_M}{N}. \quad (3.12)$$

In order to apply the above summation to a crystal we need to define the unit cell. As can be seen in figure 3.1, each lattice structure is characterized by:

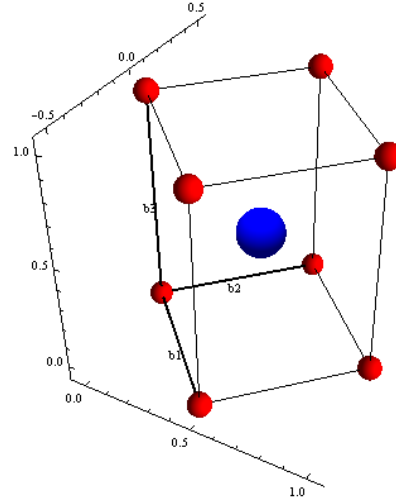


Figure 3.1: Defining the unit cell of a CuAu isostructure. The lattice vectors  $b_1, b_2, b_3$  define its shape and the positions of the particles are then given in terms of these vectors. Particles are located at  $v_1 = (0, 0, 0)_{\text{latt}}$  and  $v_2 = (1/2, 1/2, 1/2)_{\text{latt}}$  in this case. The number  $n_A = 1$  tells us that  $v_1$  corresponds to species  $A$  and  $v_2$  to species  $B$ .

- The lattice vectors  $\mathbf{b}_1, \mathbf{b}_2, \mathbf{b}_3$ . These determine the dimensions of the unit cell. For simpler notations we will use the  $3 \times 3$  matrix  $B_{\text{latt}}$ :

$$B_{\text{latt}} \equiv \begin{pmatrix} b_{11} & b_{21} & b_{31} \\ b_{12} & b_{22} & b_{32} \\ b_{13} & b_{23} & b_{33} \end{pmatrix}, \quad (3.13)$$

having the lattice vectors as columns, as an easy basis to work in.

- The particle locations  $\mathbf{v}_1, \mathbf{v}_2, \dots, \mathbf{v}_n$  of the  $n$  particles in the unit cell, expressed relative to the lattice vectors (such that  $\mathbf{v}_1, \mathbf{v}_2, \dots, \mathbf{v}_n$  are dimensionless). Now, the position of particle  $m \in \{1, 2, \dots, n\}$  in Cartesian coordinates equals

$$\mathbf{r}_m = B_{\text{latt}} \cdot \mathbf{v}_m. \quad (3.14)$$

- The number of  $A$ -particles in the unit cell:  $n_A$ . This tells us that the first  $n_A$  particles belong to species  $A$  ( $1, 2, \dots, n_A \in \mathcal{A}$ ) and the rest to species  $B$  ( $n_A + 1, n_A + 2, \dots, n \in \mathcal{B}$ ).

Extrapolating this unit cell generates the complete lattice (in Cartesian coordinates):

$$\begin{aligned} \{\mathbf{R}\}_{\mathcal{N}} &\equiv \{(v_{m1} + i)\mathbf{b}_1 + (v_{m2} + j)\mathbf{b}_2 + (v_{m3} + k)\mathbf{b}_3 \mid (i, j, k) \in \mathbb{Z}^3, m \in \{1, 2, \dots, n\}\} \\ &= \left\{ B_{\text{latt}} \cdot \left( \mathbf{v}_m + \begin{pmatrix} i \\ j \\ k \end{pmatrix} \right) \mid (i, j, k) \in \mathbb{Z}^3, m \in \{1, 2, \dots, n\} \right\}, \end{aligned} \quad (3.15)$$

where  $m$  runs over all  $n$  particles within the unit cell and  $(i, j, k)$  over all cells. Its subsets  $\{\mathbf{R}\}_A$  or  $\{\mathbf{R}\}_B$  can be obtained by simply replacing  $m \in \{1, 2, \dots, n\}$  with  $m \in \{1, 2, \dots, n_A\}$  or  $m \in \{n_A + 1, n_A + 2, \dots, n\}$ , reminding the reader that  $n$  is the number of particles in the unit cell.

Note that by defining the lattice we fixed the density  $\rho_{\text{latt}} \equiv \frac{N}{V_{\text{latt}}} = \frac{n}{|\det[B_{\text{latt}}]|}$  and therefore also the packing fraction

$$\eta_{\text{latt}} \equiv \frac{4\pi}{3} \frac{N_A a_A^3 + N_B a_B^3}{V} = \frac{4\pi}{3} ((1-x)a_A^3 + x a_B^3) \rho_{\text{latt}} \quad (3.16)$$

where we introduced the mixing ratio  $x \equiv N_B/N$  of the colloidal mixture. Distances  $\mathbf{R}_{ij}$  scale as  $(\frac{V}{N})^{1/3} = \rho^{-1/3} \propto \eta^{-1/3}$ . That is why we use a scaling factor  $\left(\frac{\eta}{\eta_{\text{latt}}}\right)^{-1/3}$  for different packing fractions:

$$\begin{aligned} U_M[\eta] = & \frac{1}{2} \sum_{l,m=1}^{n_A} \sum_{\substack{i,j,k \in \mathbb{Z} \\ (i,j,k) \neq \mathbf{0} \text{ if } l=m}} V_{AA} \left[ \left( \frac{\eta}{\eta_{\text{latt}}} \right)^{-1/3} B_{\text{latt}} \cdot \left( \mathbf{v}_l - \mathbf{v}_m + \begin{pmatrix} i \\ j \\ k \end{pmatrix} \right) \right] \\ & + \sum_{l=1}^{n_A} \sum_{m=n_A+1}^n \sum_{i,j,k \in \mathbb{Z}} V_{AB} \left[ \left( \frac{\eta}{\eta_{\text{latt}}} \right)^{-1/3} B_{\text{latt}} \cdot \left( \mathbf{v}_l - \mathbf{v}_m + \begin{pmatrix} i \\ j \\ k \end{pmatrix} \right) \right] \\ & + \frac{1}{2} \sum_{l,m=n_A+1}^n \sum_{\substack{i,j,k \in \mathbb{Z} \\ (i,j,k) \neq \mathbf{0} \text{ if } l=m}} V_{BB} \left[ \left( \frac{\eta}{\eta_{\text{latt}}} \right)^{-1/3} B_{\text{latt}} \cdot \left( \mathbf{v}_l - \mathbf{v}_m + \begin{pmatrix} i \\ j \\ k \end{pmatrix} \right) \right] \end{aligned} \quad (3.17)$$

Applying the DLVO potential (3.1) for the pair interactions shows us that the Madelung energy  $U_M$  depends not only on the structure  $\{\mathbf{R}\}_N$ , but on all the parameters  $\kappa$ ,  $a_A$ ,  $a_B$ ,  $Z_A$ ,  $Z_B$ ,  $\lambda_B$ ,  $N_A$ ,  $N_B$ ,  $V$  as well. Fortunately, we can reduce the number of parameters by introducing the dimensionless quantities:

$$K \equiv \kappa(a_A + a_B) \quad (3.18)$$

$$Q \equiv -\frac{Z_A}{Z_B} \quad (3.19)$$

$$q \equiv \frac{a_B}{a_A} \quad (3.20)$$

$$\eta \equiv \frac{4\pi}{3} \frac{N_A a_A^3 + N_B a_B^3}{V} \quad (3.21)$$

$$x \equiv \frac{N_B}{N}, \quad (3.22)$$

which represent the (dimensionless) inverse screening length, charge ratio, size ratio, packing fraction and the mixing ratio respectively. As it turns out these 5 parameters determine the complete phase behavior, as long as we keep considering only the ground state.

## 3.2 Methods

### 3.2.1 Crystal structures

In theory there is an endless number of crystal structures that we could investigate, especially when we allow for arbitrarily large unit cells, but time and effort limit us to making a selection of candidate structures.

The majority of our candidate structures are just the colloidal analogues of well-known ordinary crystals. We will call these so-called isostructures by the names of their atomic counterparts, such as NaCl, CsCl, etc. We selected the 2-component ones with  $\lesssim 10$  particles per unit cell from the U.S. Navy Center for Computational Materials Science's database of crystal structures [30], whose stoichiometries (i.e.  $N_A:N_B$  ratios) ranged in effect from 1:1 to 1:7. In addition we investigated a few quasi-atomic structures, such as the doped fullerenes  $A_2C_{60}$ ,  $A_3C_{60}$ ,  $A_4C_{60}$ ,  $A_6C_{60}$ ,  $A_{10}C_{60}$  and  $A_{11}C_{60}$  [31, 32, 33], and some new structures that have no atomic counterpart, called LS,  $LS_2$ , ...  $LS_8$  [17]. In total we looked at more than 50 different crystals.

Colloidal charge neutrality, represented by  $(1-x)Z_A + xZ_B = 0$ , is not required because of screening by salt ions, so we did not use that as a restriction for choosing candidate structures. This also means that for fixed charge ratio, it still makes sense to perform the Madelung energy calculations with all candidates, although structures with a large excess charge are not likely to be stable with respect to all the other ones.

The candidate structures were either entered manually into our program by directly defining the lattice vectors  $\mathbf{b}_1, \mathbf{b}_2, \mathbf{b}_3$ , the position vectors  $\mathbf{v}_1, \mathbf{v}_2, \dots, \mathbf{v}_n$  and the number  $n_A$ , or they were loaded from standard xyz-files containing only the particles' Cartesian coordinates. In the latter case, the generated unit cell is also Cartesian and is therefore not necessarily the primitive unit cell. These larger unit cells make calculations a little slower in general, which is the main reason for entering simple structures manually.

### 3.2.2 Numerical calculations

Instead of straightforwardly using equation (3.17) for the calculation of  $U_M$  we make this numerical calculation much more efficient by setting up 3 tables containing separation distances between particles and the number of times that they occur, for the  $AA$ ,  $AB$  and  $BB$  interactions respectively. This initialization procedure of counting close neighbors needs to be executed only once for each structure and therefore saves a lot of processor time. Performing computations at different packing fractions  $\eta$  requires scaling these distances by the previously mentioned scaling factor  $(\eta/\eta_{\text{latt}})^{-1/3}$  and doing the summation again. Furthermore, it seems a logical step to take advantage of the symmetries that crystal lattices possess per definition. The eight-fold symmetry of the cubic NaCl structure (see figure 3.8(a)), for instance, makes computations roughly 8 times faster this way.

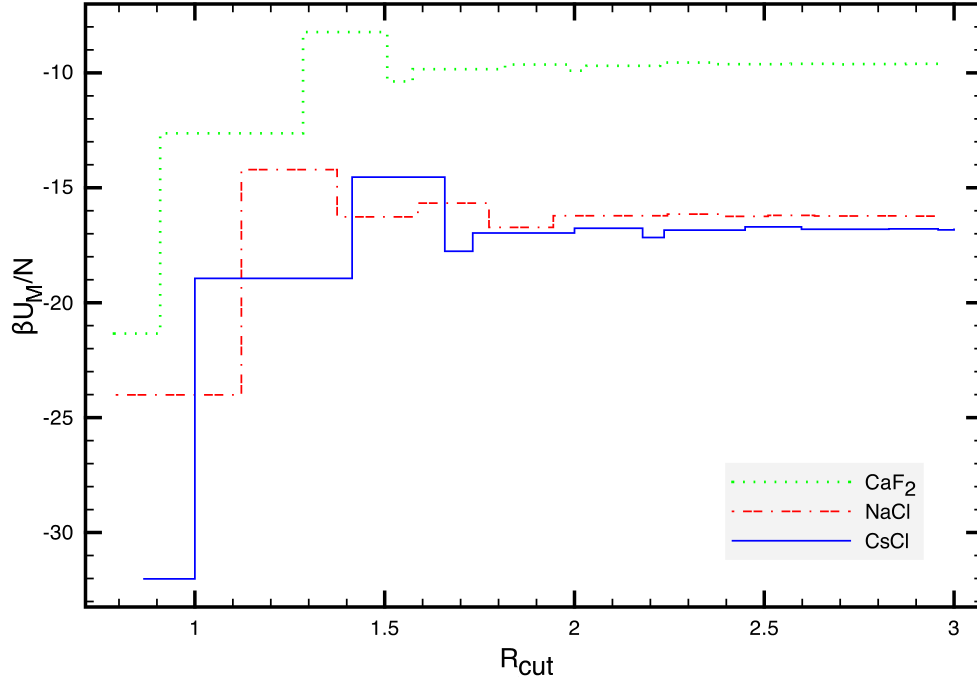


Figure 3.2: Madelung energies  $\beta U_M/N$  of the  $\text{CaF}_2$ ,  $\text{NaCl}$  and  $\text{CsCl}$  isostructures as a function of the dimensionless cutoff distance  $R_{\text{cut}}$  for  $K = 3$ ,  $Q = 1$ ,  $q = 1$  and  $\eta = \eta_{\text{max}}$ . Notice that  $R_{\text{cut}}$  needs to be at least 3 for this case, such that the Madelung summations converge to reach a reasonable accuracy level. The jumps in the  $\beta U/N$  coincide with the separation distances between close neighbors, that are suddenly taken into account when  $R_{\text{cut}}$  exceeds these distances.

Note that the Madelung summation (3.11) converges better for shorter screening lengths (i.e. larger  $K$ ). In the limit of  $K \rightarrow 0$  the DLVO potential reduces to the unscreened  $1/r$  Coulomb potential, whose summation converges very poorly. For this reason we introduce a dimensionless cutoff distance that only takes into account the lattice points with separation distances

$$R_{ij} \leq R_{\text{cut}} \rho^{-1/3} \quad (3.23)$$

and subsequently set

$$R_{\text{cut}}[K] = \max[15/K, 1.5]. \quad (3.24)$$

The factor 15 is chosen somewhat heuristically, such that the relative error in  $U_M$  is of the order of magnitude of  $10^{-6}$ . The minimum of 1.5 serves to prevent  $R_{\text{cut}}$  from becoming so small that there are no neighbors left to sum over. Figure 3.2 illustrates nicely how the Madelung sum converges for sufficiently large  $R_{\text{cut}}$ , for several crystal structures.

This being said, we now compute  $U_M[\eta]$  at a fixed point  $(q, K, Q)$  in parameter space and minimize this for  $\eta \in [0, \eta_{\text{max}}]$ , where  $\eta_{\text{max}}$  is the packing fraction of the densest packed



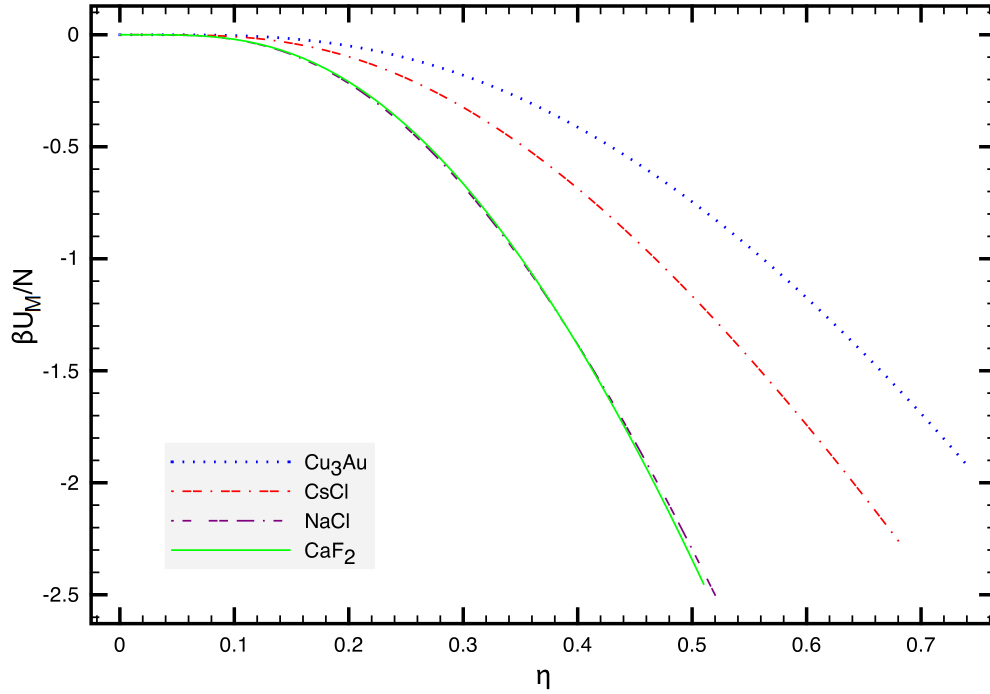


Figure 3.3: Madelung energies  $\beta U_M/N$  as function of packing fraction  $\eta$ , for parameter values  $K = 6$ ,  $Q = 3$  and  $q = 1$ . Notice that both packing considerations (through  $\eta_{\max}$ ) and electrostatic contributions are of major importance to  $U_M^{\min}$ .

crystal. As it turns out, most (meta-)stable crystals (i.e. with negative  $U_M$ ) reach their lowest Madelung energy  $U_M^{\min}$  at  $\eta = \eta_{\max}$  (see figure 3.3). We repeat this for several different structures and compare energies  $U_M^{\min}$  in order to find coexisting phases.

### 3.2.3 Coexisting phases

When comparing the Madelung energies of different structures, it does not suffice to simply declare the one with the lowest  $u_M$  to be the most stable structure. We also have to take their stoichiometries and the system's overall mixing ratio  $x$  into account. For example, a structure of the  $AB_2$  stoichiometry may approximately have the same  $u_M$  as an  $AB$  structure, but it needs one extra B-particle per A-particle. Hence less unit cells can be formed out of a 1 : 1 colloidal suspension, causing the system's total energy to be much lower than  $Nu_M$ , because half of the A-particles are not even crystallized.

We will therefore derive the correct method for determining the stability and coexistence of two different structures  $\alpha$  and  $\beta$ , which have stoichiometries  $A_iB_j$  and  $A_kB_l$  respectively. For simplicity, we write  $x^\alpha \equiv j/(i + j)$  and  $x^\beta \equiv l/(k + l)$ <sup>1</sup> for the particle fractions

<sup>1</sup>Greek letters in superscript do not indicate exponentiation here, but serve only to distinguish crystal structures  $\alpha$  and  $\beta$

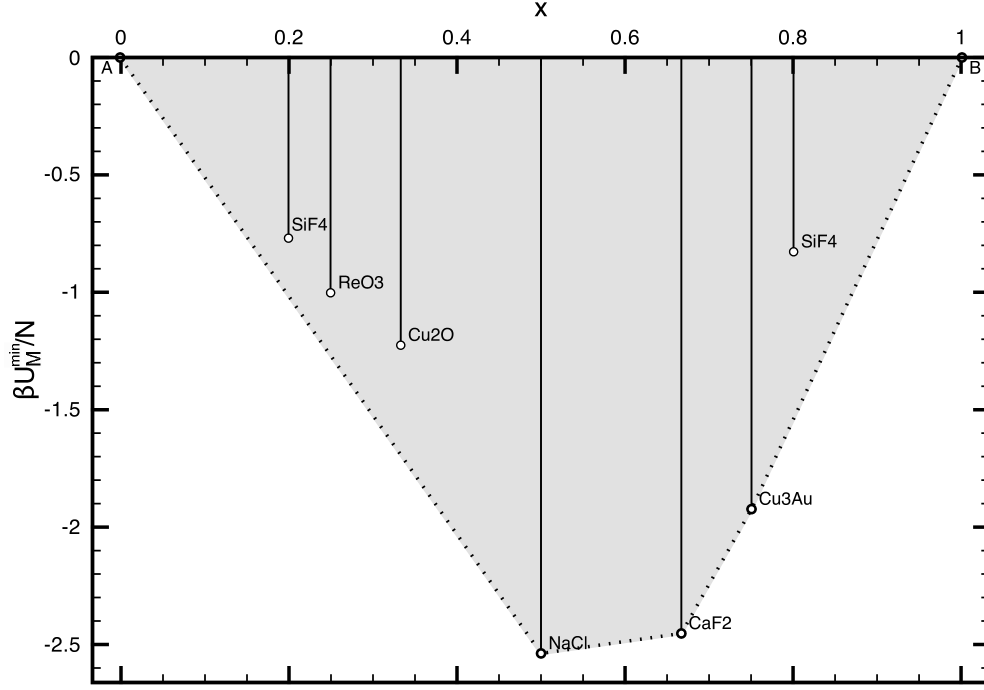


Figure 3.4: Madelung energies  $\beta U_M^{\min}/N$  versus mixing ratios  $x$  of several crystal structures with different stoichiometries. This plot, taken at  $K = 6$ ,  $Q = 3$  and  $q = 1$ , shows stable NaCl, CaF<sub>2</sub> and Cu<sub>3</sub>Au structures and metastable SiF<sub>4</sub>, ReO<sub>3</sub> and Cu<sub>2</sub>O ones. The dotted lines represent coexistence between the stable phases and the infinitely dilute gasses of A- or B-particles, shown as points (0,0) and (1,0). Note that SiF<sub>4</sub> appears twice as a metastable structure, once as the regular AB<sub>4</sub> phase at  $x = 4/5$  and once as A<sub>4</sub>B, which is obtained by interchanging the A- and B-particles or, equivalently, by setting  $Q' \rightarrow 1/Q$  and  $q' \rightarrow 1/q$ .

of both structures and we will call  $\alpha$  the structure with the lowest particle fraction, i.e.  $0 < x^\alpha \leq x^\beta < 1$ .

Let us consider the regime where there is an abundance of A-particles, i.e.  $N_A/N_B > i/j > k/l$  or, equivalently,  $x \leq x^\alpha \leq x^\beta$ . Here it is the number of B-particles that restricts the maximum number of A<sub>i</sub>B<sub>j</sub> units (called  $N^\alpha$  or  $N^\beta$ ) to be formed, such that the total Madelung energy of that structure becomes

$$U_{\text{TOT}}^\alpha = N^\alpha(i+j)u_M^\alpha = \frac{N_B}{j}(i+j)u_M^\alpha = xN\frac{i+j}{j}u_M^\alpha = \frac{x}{x^\alpha}Nu_M^\alpha \quad \text{for } x \leq x^\alpha \leq x^\beta \quad (3.25)$$

and similarly for  $U_{\text{TOT}}^\beta$ . Since the structure with the lowest total Madelung energy is stable, this means we should compare energies  $u_M^i/x^i$  instead of  $u_M^i$ . In figure 3.4 this manifests itself, for example, as NaCl being more stable than CaF<sub>2</sub> for mixing ratios  $x \leq 1/2$ , since the former has a lower  $u_M^i/x^i$  or, in other words, a steeper slope to point A.

For the upper regime, in which  $x^\alpha \leq x^\beta \leq x$ , we find in the same way that

$$U_{\text{TOT}}^\alpha = \frac{1-x}{1-x^\alpha} N u_M^\alpha \quad \text{for } x \geq x^\beta \geq x^\alpha \quad (3.26)$$

and we see that the structure with the lowest  $u_M^i/(1-x^i)$  is stable. Now figure 3.4 shows us that  $\text{CaF}_2$  is more stable than  $\text{NaCl}$  for  $x \geq 2/3$ , this time because it has a steeper slope to point B.

From this it is easy to deduce what happens in the intermediate regime, when  $x^\alpha \leq x \leq x^\beta$ . Suppose that a large number of particles is crystallized into the  $\alpha$  structure, such that the mixing ratio of the particles still in suspension is exceeding  $x^\beta$ , so the uncrystallized part of the system is effectively in the upper regime. Then, according to what was found above and because of  $u_M^\beta/(1-x^\beta) < u_M^\alpha/(1-x^\alpha)$ , the system would prefer to (partly) crystallize into a  $\beta$  structure or even turn an  $\alpha$  unit cell into a  $\beta$  unit cell in order to lower the total Madelung energy. We conclude that this leads to an equilibrium between structures  $\alpha$  and  $\beta$  in the intermediate regime. Extending this method to more than two different crystal structures will always generate a convex ‘body’ of connected points (the shaded part in figure 3.4) in a diagram of  $\beta U/N$  versus  $x$ .

The above argumentation shows that the dotted lines in figure 3.4, connecting points A,  $\text{NaCl}$ ,  $\text{CaF}_2$ ,  $\text{Cu}_3\text{Au}$  and B, should be interpreted as coexistence lines, meaning that a system with fixed mixing ratio always splits into a linear combination of the 2 nearest coexisting phases, except of course when  $x$  exactly equals the particle fraction  $x^\alpha$  of a stable structure. The points A and B represent the pure A and pure B gas phases, which are infinitely dilute at zero pressure because of their repelling charges and therefore both have energies  $u = 0$ .

In fact this method of constructing coexistence diagrams can be seen as a discrete equivalent of the normal common-tangent construction in an  $x$ - $G$  diagram, with  $p = 0$  and  $T = 0$  causing the Gibbs free energy  $G$  to equal the Madelung energy  $U$ , as we mentioned in the beginning of this chapter.

## 3.3 Results

### 3.3.1 Phase diagrams for fixed size ratios

Since we are dealing with 4 independent parameters  $q$ ,  $K$ ,  $Q$  and  $x$ , it would be quite time consuming to calculate the complete 4D phase diagram and, besides that, not so easy to depict it in the form of 2D diagrams. We therefore determine a number of intersections that span a large part of the total phase diagram, in order to gain more understanding of the effects that are manifested and such that the intermediate parts can be more or less extrapolated.

We have investigated 3 different size ratios:  $q = 1$  (equal sizes),  $q = 0.65$  and  $q = 0.31$ . The results for each of these cases are shown in figures 3.5 to 3.7. The (a) and (b) diagrams in

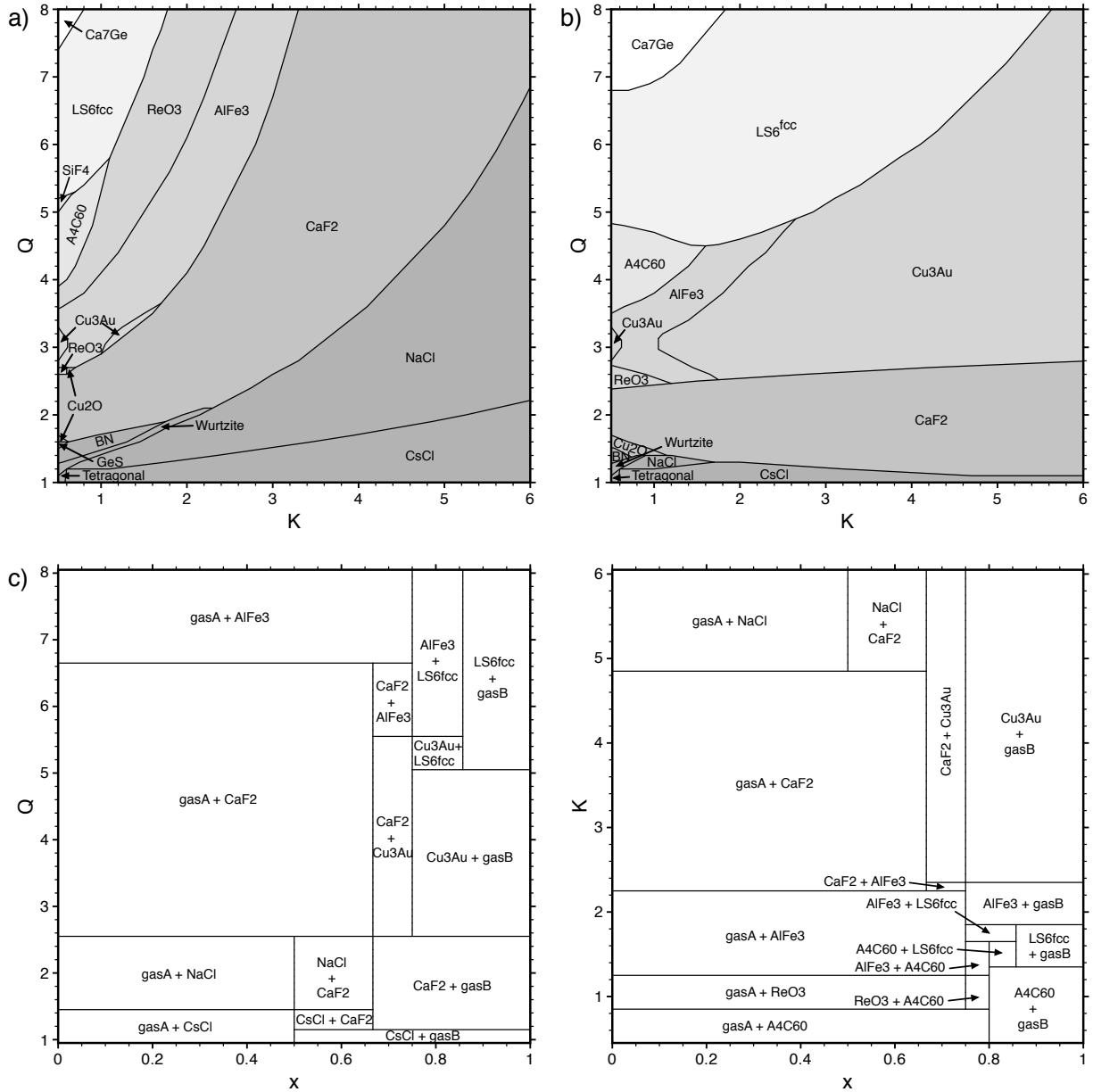


Figure 3.5: Phase diagrams for equally sized particles, based on Madelung energies. Diagrams (a) and (b) show the crystal structures that are coexisting with a dilute gas of only A-particles and only B-particles respectively, as a function of  $Q$  and  $K$ . Shading is used to mark different stoichiometries. Note that the point  $K = 6$ ,  $Q = 3$  corresponds to the situation in figure 3.4, in which NaCl coexists with gas phase A and  $\text{Cu}_3\text{Au}$  with gas phase B, whereas the intermediate  $\text{CaF}_2$  structure coexists with both NaCl and  $\text{Cu}_3\text{Au}$  and is not displayed in these  $QK$  diagrams. Diagram (c) is a fixed-screening intersection of the  $q = 1$  phase diagram with  $K = 3$ , showing the pairs of coexisting phases in each region, where tie lines between phases should be drawn horizontally. The dilute gas phases of pure A- or B-particles are denoted by gasA and gasB respectively. Note that the  $x \downarrow 0$  and  $x \uparrow 1$  parts correspond to the  $K = 3$  intersections of (a) and (b). (d) is a similar diagram, but this time for fixed charge ratio  $Q = 4.5$ .

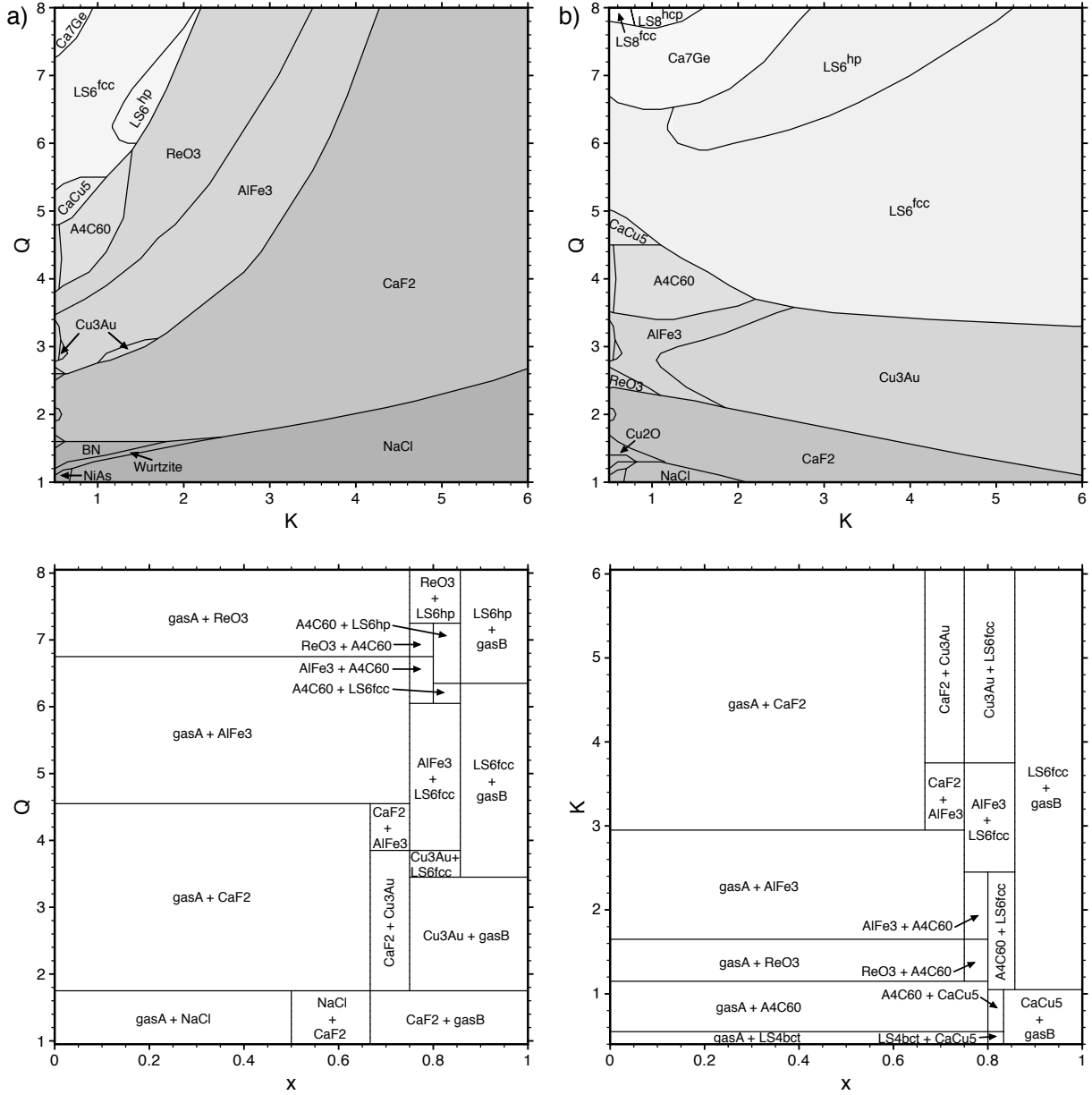


Figure 3.6: Phase diagrams based on Madelung energies, similar to figure 3.5, but for size ratio  $q = 0.65$ . (a) The unmarked structures at  $K = 0.5$  are (from high to low  $Q$ )  $LS_4^{bct}$ ,  $LS_3$ ,  $ReO_3$ ,  $Cu_2O$ ,  $LS_2$ ,  $Cu_2O$  and  $GeS$ . (b) The unmarked structures near  $K = 0.5$  are (from high to low  $Q$ )  $LS_4^{bct}$ ,  $LS_3$ ,  $Cu_3Au$ ,  $LS_2$ ,  $BN$ ,  $Wurtzite$  and  $NiAs$ .

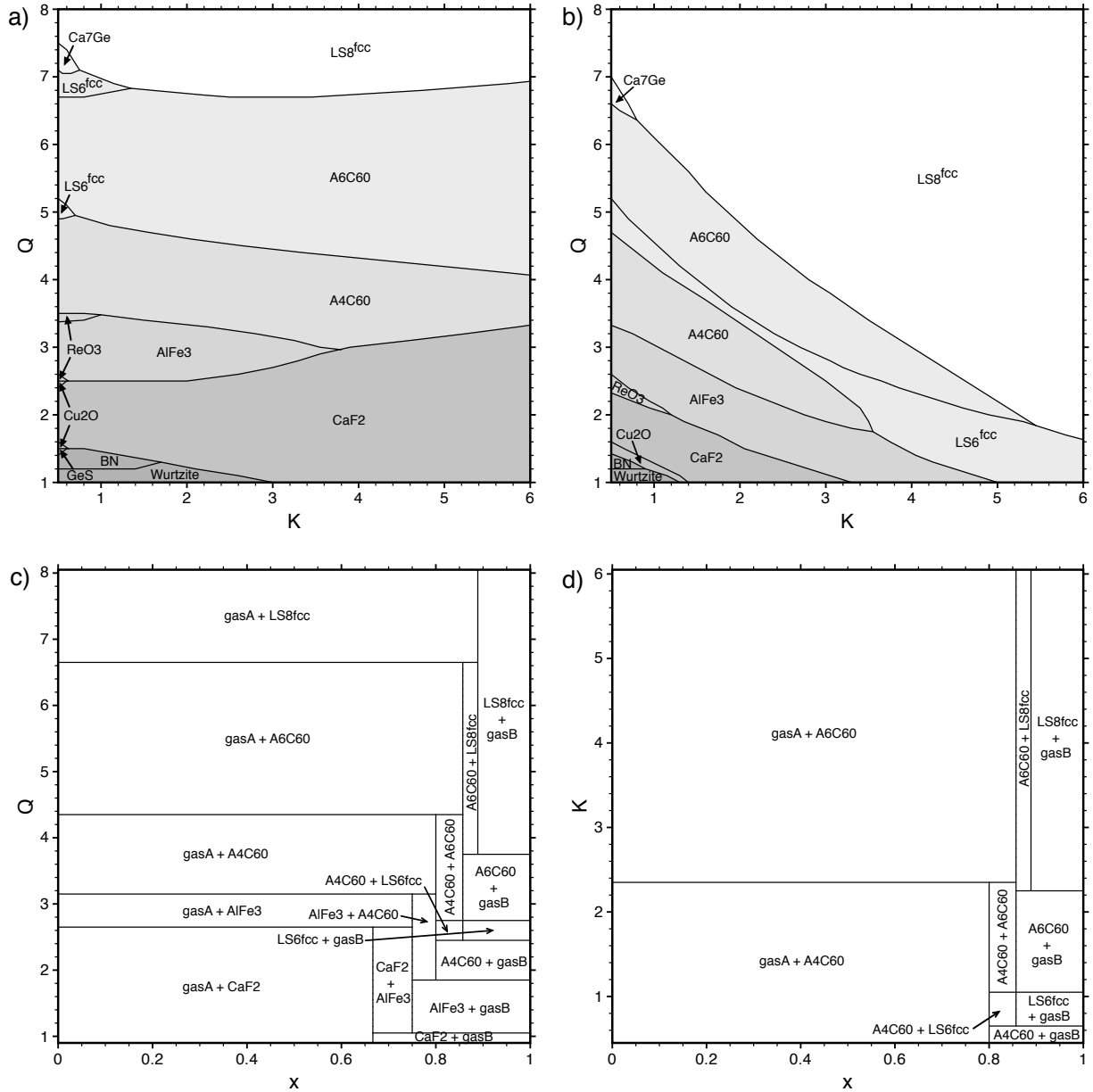


Figure 3.7: Phase diagrams based on Madelung energies, similar to figures 3.5 and 3.6, but for size ratio  $q = 0.31$ . Note that the large stability region for  $LS_8$  in diagram (b) is probably misleading, because other (not investigated) structures with higher stoichiometries are likely to be stable there (not  $A_{10}C_{60}$  and  $A_{11}C_{60}$  however, which we did in fact include in our calculations).

figures 3.5 to 3.7 can be regarded as the  $x \downarrow 0$  and  $x \uparrow 1$  intersections of the fixed  $q$  phase diagram (see also figure 3.4), so they show us which phases are coexisting directly with a dilute phase of only A-particles (a) or only B-particles (b).

Although they contain a lot of information about the phase behavior, the intermediate  $x$  structures that are only coexisting with other crystal phases, are not visible. Notice that the phase diagrams for  $x = 1/2$  (not displayed) would be exactly the same as the  $x \downarrow 0$  diagrams, because all structures with stoichiometries less than 1 : 1 (those left of the  $x = 1/2$  line in figure 3.4, for example) turn out to be metastable. Increasing the mixing ratio from  $x = 1/2$  to  $x = 1$  gradually changes the phase diagrams from the (a) to the (b) diagrams. Displaying an intermediate  $x$  intersection would not be very insightful and that is why we draw x-Q (c) and x-K intersections (d) instead.

We found a large number of stable crystal structures, although many of them are only present in very small regions near  $K = 0.5$ . These crystal structures are displayed in figure 3.8 and described in more detail in table 3.3.1.

The  $A_{10}C_{60}$  and  $A_{11}C_{60}$  lattices were not found to be stable anywhere within the investigated parameter ranges, contrary to what we had expected. It still remains likely though that other structures with the same stoichiometries will be discovered for  $q = 0.31$ .

### 3.3.2 Influence of parameters on phase behavior

In order to gain more insight into the phase behavior, we describe some of the effects that are exhibited and how they relate to the system parameters  $Q$ ,  $K$ ,  $x$  and  $q$ .

The most striking phenomena that we notice when looking at the  $QK$  diagrams in figures 3.5 to 3.7, are the effects of charge neutrality and screening. For low screening it is obvious from all 6 diagrams 3.5(a), 3.5(b), 3.6(a), 3.6(b), 3.7(a) and 3.7(b) that the charge ratio dominates the phase behavior. Structures with stoichiometries that do not match the system's charge ratio are hardly ever stable in this region, so in general the most stable structures for  $Q = m$  are of the form  $AB_m$ . (The only exception seems to be the absence of an  $AB_5$  structure in the  $q = 0.31$  diagram.) This is due to the long range of the pair interactions, which makes long range repulsions dominant in crystals with an excess charge, such that these crystals become less stable.

Of course, charge neutrality was already familiar from ordinary ionic crystals, but our system allows us to increase the screening parameter, which gradually releases this restriction, as can be seen in the higher  $K$  regions of the diagrams. Here the phase behavior is governed by short range interactions, which tend to favor lattices with higher coordination numbers, i.e. with more oppositely charged nearest neighbors, irrespective of their particular long range structure. We find a smaller variety of crystals in this region.

The influence of the system's mixing ratio is also quite clear from the phase diagrams. Increasing  $x$  causes structures with higher stoichiometries to become more abundant, except for the low  $K$  region. We have already elaborated on this in section 3.2.3.

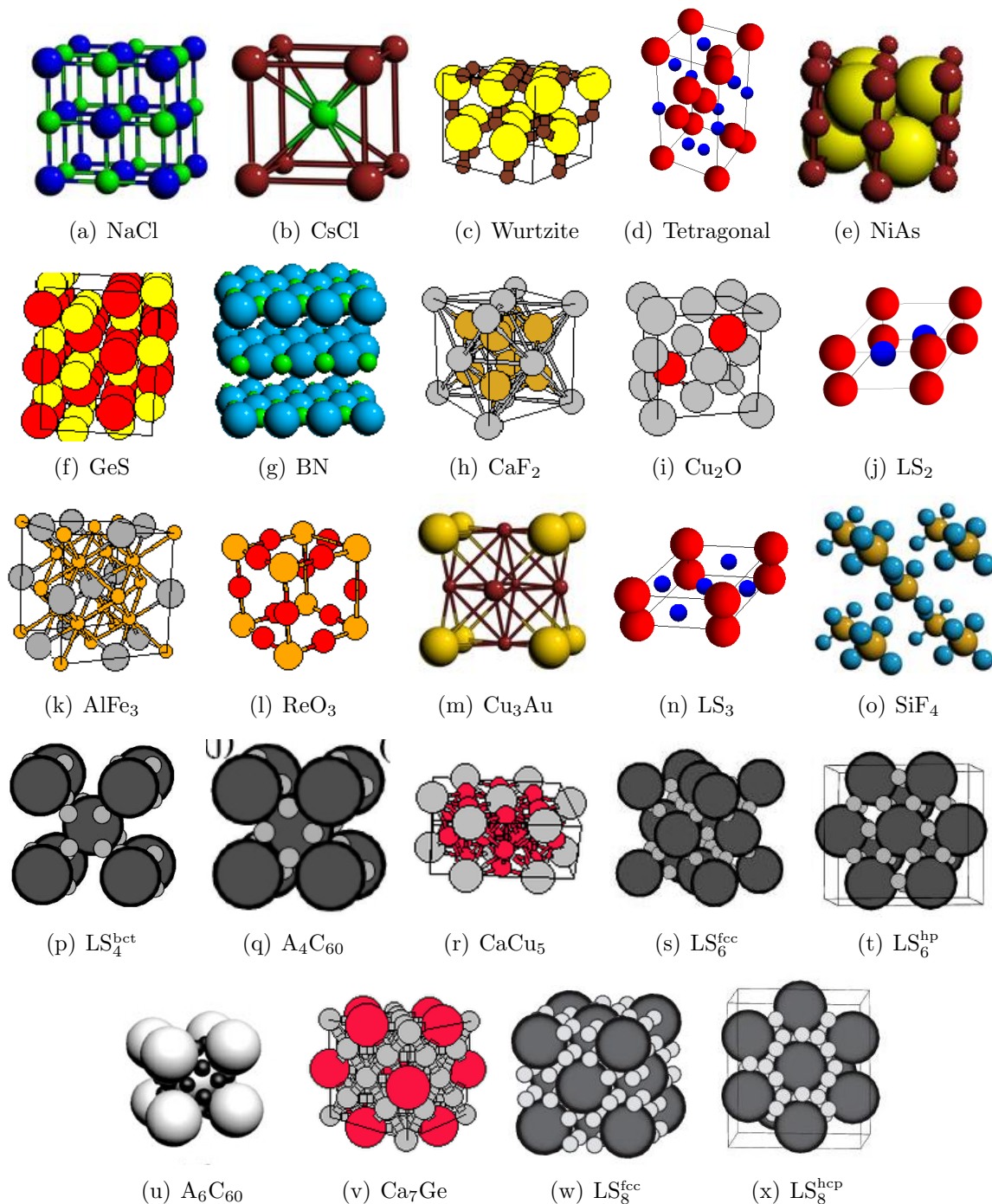


Figure 3.8: All crystal structures that were found to be stable, shown in order of increasing stoichiometry. (Pictures (p), (q), (s), (t), (w) and (x) provided by Hynninen [17], (u) taken from Forro *et al.* [32], (d), (j) and (n) drawn by ourselves and the remaining pictures were taken from the Crystal Lattice Structures Web page, <http://cst-www.nrl.navy.mil/lattice/>, provided by the Center for Computational Materials Science of the United States Naval Research Laboratory.)



Structure	L sub-lattice	S sub-lattice	Overall lattice	Remarks
NaCl	fcc	fcc	sc	3D chess board pattern
CsCl	sc	sc	bcc	
Wurtzite	hcp	hcp		
Tetragonal				
NiAs	hcp	trigonal		Binary version of hex. diamond structure
GeS				Unit cell consists of two stacked fcc cells
BN				Very open structure; hard to describe; distorted NaCl structure [34]
CaF <sub>2</sub>	fcc	sc		ABA-stacked hcp-like sublattices, but elongated in z-direction, thus forming layers
Cu <sub>2</sub> O	bcc	fcc		
LS <sub>2</sub>	trigonal	honey-comb		
AlFe <sub>3</sub>	fcc		fcc	
ReO <sub>3</sub>	sc	fcc		Relatively open, cubic-like structure
Cu <sub>3</sub> Au	sc	bct	fcc	
LS <sub>3</sub>	trigonal	kagome		
SiF <sub>4</sub>	bcc			
LS <sub>4</sub> <sup>bct</sup>	bct			Low density crystal; each large particle is connected to a tetrahedron of small ones
A <sub>4</sub> C <sub>60</sub>	bcc			Small particles form squares in plane between 4 neighboring large colloids
CaCu <sub>5</sub>	trigonal			Similar to LS <sub>4</sub> <sup>bct</sup> , but squares of small colloids rotated 45 degrees
LS <sub>6</sub> <sup>fcc</sup>	fcc			Hex. ring of small colloids around each large one; additional kagome layer in between
LS <sub>6</sub> <sup>hcp</sup>	hcp			Small colloids in 2 layers with kagome pattern, one in the same layer as the large particles and one layer in between
A <sub>6</sub> C <sub>60</sub>	bcc			Small colloids in 2 layers with kagome pattern, above and below each hexagonal layer of large ones
Ca <sub>7</sub> Ge	fcc		fcc	4 Small colloids situated on plane between 2 neighboring large ones
LS <sub>8</sub> <sup>fcc</sup>	fcc			Each hole between large colloids filled by cube of 8 small particles
LS <sub>8</sub> <sup>hcp</sup>	hcp			
				Honeycomb structure of small colloids in hex plane of large ones; two additional kagome pattern layers, above and below

Table 3.1: Lattice geometries of all stable structures (see figure 3.8), given for sublattices of large particles (L), small particles (S) and combined (overall). Complicated (sub)lattices have not been named.

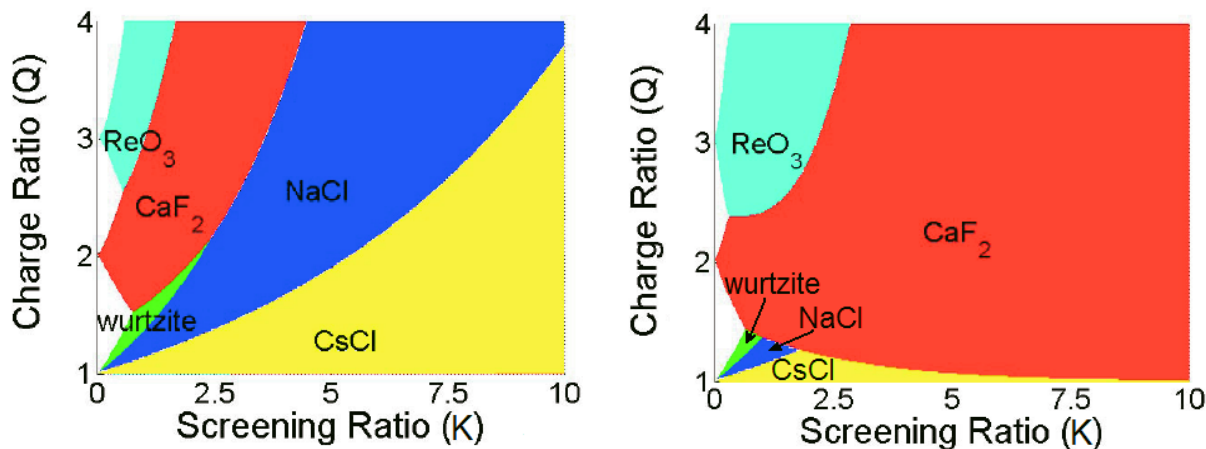


Figure 3.9: Theoretical phase diagrams for  $q = 1$ , as calculated by Maskaly. Images borrowed from reference [18] (parameter range  $Q < 1$  discarded because of obsolete results).

A final issue is the effect of size ratio, whose main consequence is the particular packing of a crystalline structure. Small  $q$  generally means that structures with more B-particles can be packed in a denser crystal and may therefore have more electrostatic energy, depending on their short range geometry, whereas 1:1 structures are packed very inefficiently in this case. Furthermore, we see in figure 3.3 that energy curves  $U_M[\eta]$  tend to become steeper at higher packing fractions, implying that a crystal that is only slightly more optimally packed will have a relatively large decrease of its Madelung energy, so this amplifies the sensitivity to size ratio. Again, we recognize this effect in the phase diagrams, where the higher stoichiometries also become more dominant with decreasing size ratio.

We have to keep in mind that this method of investigating crystal structures is not exhaustive: one can never be certain that there exist no other structures that have even lower Madelung energies than the investigated ones, even for specific conditions. We tried to lower that risk by investigating as many lattices as possible, given time and effort constraints.

Before we move on to compare our results to those of others, we pause to note that these diagrams are theoretical results that only display the stable equilibrium structures, towards which the system evolves. In an experimental situation, factors such as crystal nucleation or interfacial effects may at first cause slightly metastable structures to be formed. Given that the observation time is long enough and colloidal mobility is large enough, these structures are eventually expected to restructure into the one with the lowest Madelung energy. Experimentally, it is therefore possible to observe some metastable structures that have not been displayed in our results [35].

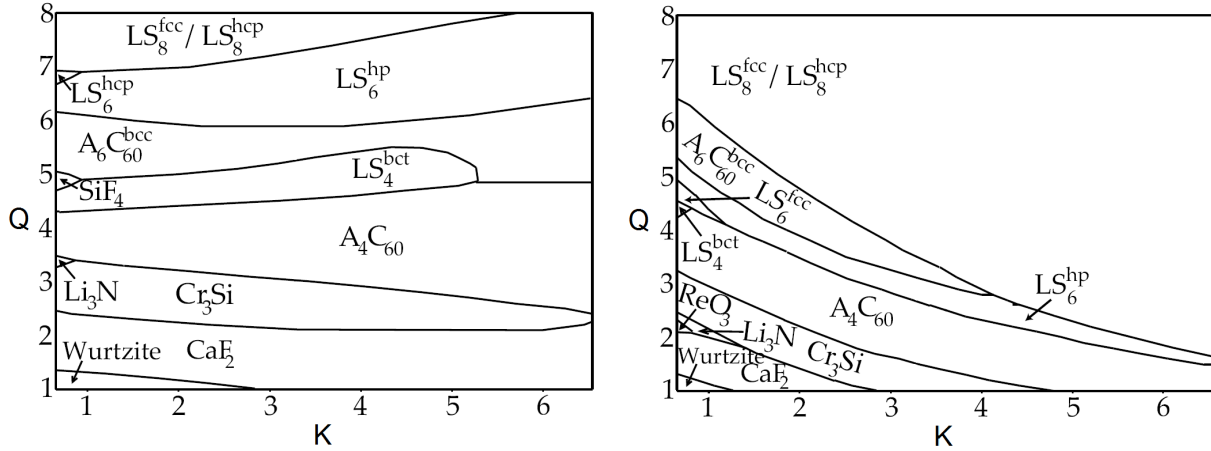


Figure 3.10: Theoretical phase diagrams for  $q = 0.31$ , as calculated by Hynninen. Images borrowed from reference [17] (K-axis rescaled in order to arrive at the same definition of the screening parameter).

### 3.3.3 Comparison to other research

Our phase diagrams for the equally sized particle case (figures 3.5a and b) agree perfectly with the numerical calculations done by Maskaly (see figure 3.9) [18, 19], which is not surprising, because the Madelung summations were performed in the same manner. However, since we investigated a larger variety of crystal structures in a larger region of parameter space, we find an even richer phase diagram with more stable structures. In some regions the structures found by Maskaly, in particular  $\text{ReO}_3$  and  $\text{CaF}_2$ , turn out to be metastable with respect to newly investigated ones, such as  $\text{AlFe}_3$  and  $\text{Cu}_3\text{Au}$ . The NaCl-CsCl boundary line for this case was also calculated by Leunissen *et al.* [13] and gives results identical to our findings.

Instead of performing new numerical calculations for systems of other size ratios, Maskaly only refers to Pauling's rules[36] to predict the general phase behavior in these situations. Applying Pauling's rules gives the range of size ratios for which a certain lattice structure can exist, based on packing criteria. The CsCl structure, for instance, has quite inefficient packing properties for  $q < 0.73$  and we found that this causes the NaCl-CsCl boundary line of figure 3.5a to retreat towards the line  $Q = 1$  when the size ratio  $q$  is decreased. At  $q \lesssim 0.73$ , CsCl becomes metastable everywhere with respect to NaCl, which explains the absence of CsCl in diagrams 3.6 and 3.7. Other structures are affected by Pauling's rules as well, but we have to realize that these rules only give a first idea of which structures are not likely to be stable, and in fact do not determine which ones are.

Comparing the  $q = 0.31$  phase diagrams to the theoretical results obtained by Hynninen *et al.* (figure 3.10) [17, 16], we notice that the general shapes of the  $QK$ -diagrams are very similar, but also that certain structures are partly or in a few occasions even completely replaced by other structures of the same stoichiometry. For example, we find larger regions of stability for  $\text{CaF}_2$  and  $\text{A}_6\text{C}_{60}$ , the latter contributing to the fact that  $\text{LS}_6^{\text{hp}}$  and  $\text{LS}_4^{\text{bct}}$  become

metastable everywhere. The major cause of these differences is most likely the specific choice for the lattice parameters of the  $LS_n$  and  $A_nC_{60}$  structures. Whereas Hynninen *et al.* have optimized the lattice parameters for every point in parameter space in order to obtain a minimal Madelung energy, our method limits us to doing this only once for each structure. In this respect we consider our method to be somewhat less accurate. Furthermore, the newly found structure  $AlFe_3$  is expected to be stable in a reasonable part of the diagram, thereby replacing the  $Cr_3Si$  found by Hynninen.

So far we have only made comparisons to other theoretical results, but the real acid test comes from actual experimental data. Leunissen *et al.* observed a dense-packed  $CsCl$  structure for approximate parameters  $q = 0.92$  (i.e. close to unity),  $Q = 1.5$ ,  $K = 7.3$  and  $x = 1/2$ , which is precisely what we would expect from Madelung energy calculations (cf. diagram 3.5a, although the particular phase point falls just outside the plotted region). However, at  $K = 10.6$  and  $Q = 1.5$  the random hexagonal close packed (rhcp) structure was found. We expect this to be due to weak electrostatic interactions because of large screening, such that entropic contributions become more important.

Bartlett and Campbell [14] investigated a system of nearly equal size particle species as well, with parameters  $q = 0.93$ ,  $Q \approx 2.8$ ,  $K = 3.7$  and  $x = 1/2$ . They observed the rhcp structure and, upon increasing the charges, subsequently  $CsCl$  and  $NaCl$ , the latter two being almost dense-packed. Since they do not mention the precise charge ratios after increasing the charges, we are unable to make a precise comparison with our results, although it is clear from diagram 3.5a that both  $NaCl$  and  $CsCl$  are stable in that specific region. If we assume that the charges were increased proportionally in order to keep their ratio constant, this would imply that the phase changes are driven by entropic contributions and that higher charges (or equivalently, lower temperatures) would favor  $NaCl$  over  $CsCl$ . For the specific phase point  $K = 3.7$ ,  $Q = 2.8$ , we indeed expect to find  $NaCl$  for higher charges, since this brings the system closer to the ground state, but we do not know yet if  $CsCl$  is stable at that point for higher temperatures. This will be the issue of investigation in section 4.3.3.

Dense packing was expected for these structures, because  $U_M[\eta]$  is found to be minimal for  $\eta = \eta_{\max}$ , as in figure 3.3. Note that entropy might change this (see chapter 4).

Experimental results for size ratio  $q = 0.31$  were also obtained by Leunissen and Hynninen *et al.* [13, 16], this time for parameters  $x = 8/9$ ,  $K \approx 6$  and unknown  $Q$ . Several structures were observed, namely  $LS_6$ ,  $A_6C_{60}$ ,  $LS_8^{\text{fcc}}$  and  $LS_8^{\text{hcp}}$ . Again, absence of precise information on  $Q$  and  $K$  makes an accurate comparison with our results impossible, although obviously the first three structures are fairly abundant in diagram 3.7b. Our calculations show that  $LS_8^{\text{hcp}}$  is only a little less stable than  $LS_8^{\text{fcc}}$ , so this is accounted for as well. In fact, estimating the charge ratio to be  $Q \lesssim 3$  would give quite good agreements between theory and experiment.

## 3.4 Conclusions

Using Madelung energy calculations, we determined phase diagrams of the ground state of an ICC for different size ratios. These results span a large part of the whole parameter space.

Our calculations for equally sized colloids included considerably more crystal structures than similar calculations done by other people and consequently this led to more diverse and more detailed phase diagrams with a broader parameter range. Exploring the phase diagrams for size ratio  $q = 0.65$  has yielded completely new results, since this case has not been investigated before by anyone, as far as we are aware of. The final case we looked at was size ratio  $q = 0.31$ , which had already been investigated, but nevertheless there were a number of additional finds.

We found a large variety of crystal structures, among which several ones that were not known to be stable until now. The newly discovered (theoretically) stable structures are  $\text{AlFe}_3$ ,  $\text{Cu}_3\text{Au}$ ,  $\text{Ca}_7\text{Ge}$ ,  $\text{CaCu}_5$ ,  $\text{Cu}_2\text{O}$ ,  $\text{BN}$ ,  $\text{GeS}$ , Tetragonal,  $\text{NiAs}$ ,  $\text{LS}_3$  and  $\text{LS}_2$ , although the latter 7 can only be found in tiny regions of the phase diagram with long range interactions.

Furthermore, we gave a short explanation of the general phase behavior in terms of the effects of screening, charge neutrality, packing and composition, which are (directly or indirectly) associated with the screening parameter  $\kappa(a_1 + a_2)$ , charge ratio  $Z_1/Z_2$ , size ratio  $a_2/a_1$  and mixing ratio  $N_2/N$ .

Comparing our results to other theoretical and experimental research, we found reasonable agreements, as far as the data allowed us to make a fair comparison. Nevertheless, some experimental results are not explained by our calculations and may require taking entropic contributions into account. Incidentally, this is also the topic of the next chapter.



## Finite temperature symmetric case

In the previous chapter we investigated the phase behavior as caused only by electrostatic interactions and hard-sphere repulsions. We noticed that in most circumstances the colloidal crystals were close-packed, i.e. with neighboring colloids touching one another. However, experiments seem to suggest that the spatial degrees of freedom, in other words entropy, will also play an important role. For example, particle motion of colloids around their lattice positions has been clearly observed using confocal microscopy methods [13]. In this chapter we will therefore look at the behavior of colloidal crystals at finite temperatures, thereby analyzing the influence of entropy.

At nonzero temperatures the electrostatic forces, which essentially have an overall attractive effect, are counteracted by repulsive entropic forces. The latter are likely to decrease the packing fraction of a crystal coexisting with a vapor, such that the individual particles have a larger volume at their disposal. We derive a cell-like model for the Helmholtz free energy of the crystal phase, whose potential energy part relies again on the Madelung summation method and whose contribution from entropy is determined from the volume in which colloids are able to move. By examining different versions of this model we eventually propose a fairly realistic version which can be used for further research.

Instead of assuming that the crystal phases coexist with dilute gas phases at vanishingly small pressure  $p$ , as we did in chapter 3, we will now consider the more realistic situation of coexistence with a finite pressure fluid phase. We will also explore a few different models for the fluid (see diagram 4.2), varying from an oversimplified Madelung-like version for the Helmholtz free energy to expressions that are derived using thermodynamic integration. Both of these approaches are based on well-known expressions for the hard-sphere fluid, and the latter treats the electrostatic interactions as additional perturbations.

In the introductory chapter we already mentioned that this would be the most important part of this thesis, mainly because it contains most of the new research done during this project, but also because of the more detailed investigation. It is a bit more difficult than other chapters as well, since we have to deal with more possible models to describe the

additional degrees of freedom generated by entropy. And of course, each model has its own assumptions and region of validity or, correspondingly, benefits and disadvantages, which implies extra attention when choosing the most suitable one.

The major goal of this thesis was to determine phase diagrams that describe which structures are stable, metastable or unstable in certain parts of parameter space. That is after all what we are interested in. Nevertheless, in this chapter we sometimes make decisions that lead to sub-investigations on a side track from the main line of research, some of which will be presented in the results and discussion section. These sub-investigations, for example about colloid mobility, the gas-liquid binodal, or the CsCl-CuAu phase transition, are usually still very relevant to the main topic and are often also quite interesting due to their more detailed description of certain phenomena.

All calculations will be done in the canonical ensemble, with fixed particle numbers  $N_A$ ,  $N_B$ , volume  $V$  and temperature  $T$ . Now we specifically use the restriction that both particle species are of equal size, (absolute) charge and number ( $a_A = a_B$ ,  $Z_A = -Z_B$  and  $N_A = N_B$ ). This situation, which we call the ‘symmetric case’, will make it easier for us to investigate the ICCs at finite temperatures, whereas we do not have to deal with any osmotic forces (yet), since the particle numbers are fixed.

## 4.1 Helmholtz free energies

Investigating colloidal crystals at nonzero temperatures requires us to determine the Helmholtz free energies of both the crystal phase and the fluid, with which the crystal is in coexistence. Our calculation starts with the Hamiltonian of the system:

$$H = \sum_{i \in \mathcal{N}} \frac{\mathbf{p}_i^2}{2m_i} + U[\{\mathbf{r}\}_{\mathcal{N}}], \quad (4.1)$$

with  $U[\{\mathbf{r}\}_{\mathcal{N}}]$  again being the total potential energy of a general configuration of colloidal particles including the hard core part, as defined in equation (3.10). This leads to a general partition function:

$$Z = \frac{1}{(\Lambda^*)^{3N}} \int d\mathbf{r}^{\mathcal{N}} \exp[-\beta U[\{\mathbf{r}\}_{\mathcal{N}}]], \quad (4.2)$$

where the prefactor represents the evaluated momentum integral for all  $N$  particles in 3 dimensions, that contains the (mass-dependent) constant

$$\Lambda^* \equiv \left( \prod_{i \in \mathcal{N}} \sqrt{\frac{\hbar}{2\pi m_i k_B T}} \right)^{1/N}, \quad (4.3)$$

that can be regarded as the average thermal wavelength for colloids with different masses. A rigorous, though not very relevant, treatment of this partition function derived from the Hamiltonian for microscopic particles of which the colloids consist, is given in appendix C.2.



Once we will have written down specific expressions for  $Z$ , we will mainly work with their corresponding Helmholtz free energies:

$$\beta F = -\log[Z], \quad (4.4)$$

but first we need to look at a few different models for the crystal and later for the fluid phase.

### 4.1.1 Crystal phase

In order to determine the Helmholtz free energy of a certain crystal structure, we consider the situation where all colloids are situated approximately on the lattice sites corresponding to this structure, such that we can in fact speak of a crystalline solid phase without any defects. This enables us to make a Taylor expansion of the potential energy  $U[\{\mathbf{r}\}_{\mathcal{N}}]$  around the lattice coordinates  $\{\mathbf{R}\}_{\mathcal{N}}$ , such that we get

$$U[\{\mathbf{r}\}_{\mathcal{N}}] \simeq U_M + \frac{1}{2} \sum_{i,j \in \mathcal{N}} \sum_{\sigma,\tau=1}^3 s_i^\sigma M_{ij}^{\sigma\tau} s_j^\tau \quad (4.5)$$

where we introduced the tensor of second derivatives of the potential energy:

$$M_{ij}^{\sigma\tau} \equiv \frac{\partial}{\partial r_i^\sigma} \frac{\partial}{\partial r_j^\tau} U[\{\mathbf{r}\}_{\mathcal{N}}] \Big|_{\{\mathbf{R}\}_{\mathcal{N}}} \quad (4.6)$$

and  $s_i^\sigma \equiv r_i^\sigma - R_i^\sigma$  being the  $x$ -,  $y$ - or  $z$ -coordinate (for  $\sigma = 1, 2, 3$  respectively) of the displacement vector  $\mathbf{r}_i - \mathbf{R}_i$  for particle  $i$ .

The zeroth order term in the expansion is just the electrostatic energy of the perfect crystal, so this gives again the Madelung energy, as calculated in chapter 3.

Whereas for most equilibrium systems in physics one expects to find particles located at or near a potential energy *minimum* and therefore having a vanishing linear term in its Taylor expansion, this is not automatically guaranteed in the system we are looking at. As it turns out, with few exceptions the lattice points actually constitute local *maxima* in the potential energy (see figure 4.4), because of the fact that a particle is likely to be surrounded by oppositely charged neighbors in a stable crystal. Of course, local maxima also imply a vanishing linear term and as long as the lattice is sufficiently symmetric, this is what happens.

The higher order terms can also be neglected, because the maximal displacements are quite small for relatively dense crystals. We will come back to that later in this chapter, when the mobility of colloids is investigated.

Using the above expansion we arrive at

$$Z_{\text{crystal}} \simeq \frac{\exp[-\beta U_M]}{(\Lambda^*)^{3N}} \int_{\mathcal{V}} d\mathbf{s}^{\mathcal{N}} \exp \left[ -\frac{\beta}{2} \sum_{i,j \in \mathcal{N}} \sum_{\sigma,\tau=1}^3 s_i^\sigma M_{ij}^{\sigma\tau} s_j^\tau \right]. \quad (4.7)$$

Here, the integration region  $\mathcal{V}$  is a  $3N$ -dimensional hyper-volume that takes the hard-sphere repulsions into account, thus making sure that colloids do not overlap when they have excursions  $\mathbf{s}_1, \mathbf{s}_2, \dots, \mathbf{s}_N$  such that  $(\mathbf{s}_1, \mathbf{s}_2, \dots, \mathbf{s}_N) \in \mathcal{V}$ .

However, this complicated integration region  $\mathcal{V}$  and second order derivative tensor  $M$  make it impossible to perform the integration in equation (4.7) analytically. For example, treating  $M$  as a  $3N \times 3N$  matrix and then applying a coordinate transformation in order to diagonalize it is pointless, because of the strange integration boundaries, even if we replace  $\mathcal{V}$  by a simpler version.

Basically, we now have different choices to approximate  $M$  and  $\mathcal{V}$ . In the next part we work out what we call our standard version of  $F_{\text{crystal}}$ . Thus being able to evaluate this integral in  $Z$ , we will show that its contribution to  $F_{\text{crystal}}$  can be written as an ‘effective volume term’. And after that, we will consider 2 alternative models  $F_{\text{crystal}}^{(0)}$ ,  $F_{\text{crystal}}^{(1)}$  that have somewhat different expressions for this effective volume term.

#### 4.1.1.1 Standard version: $F_{\text{crystal}}$

In our first approach, we are more or less bound to do two things: first, we treat the crystal in some sort of harmonic approximation:

$$F = U_M - TS \simeq U_M + \sum_{i \in \mathcal{N}} F_i^{\text{harm}}, \quad (4.8)$$

which assumes that colloids do not interact with each other besides through the Madelung energy. In other words, we allow a single particle to move around in a potential energy field generated by the other particles, which are fixed at their lattice sites. This approach is equivalent to neglecting all entries of  $M_{ij}^{\sigma\tau}$  with  $i \neq j$ .

Secondly, we approximate  $\mathcal{V}$  as the product of spherical regions  $v_k^{\text{RWS}} \subset \mathbb{R}^3$ , corresponding to the volumes in which each colloid can freely move about:

$$\mathcal{V} \simeq \mathcal{V}^{\text{RWS}} \equiv v_1^{\text{RWS}} \times v_2^{\text{RWS}} \times \dots \times v_N^{\text{RWS}}. \quad (4.9)$$

A precise definition of these volumes will be given later.

We have now effectively reduced the problem to  $N$  decoupled single-particle systems. In this respect the system resembles an Einstein crystal. There are two major differences though, namely, that the integral in equation (4.7) has finite boundaries and that lattice sites may correspond to local *maxima* in the potential energy. Both have already been mentioned.

An easy way to look at the shape of the local potential energy function of particle  $k$ , is to

explicitly calculate its second derivatives  $M_{kk}^{\sigma\tau}$ . Setting  $r_{ij} \equiv r_i - r_j$ , we obtain

$$\begin{aligned} M_{kk}^{\sigma\tau} &\equiv \left. \frac{\partial^2 U[\{\mathbf{r}\}_{\mathcal{N}}]}{\partial r_k^\sigma \partial r_k^\tau} \right|_{\{\mathbf{R}\}_{\mathcal{N}}} = \frac{1}{2} \frac{\partial^2}{\partial r_k^\sigma \partial r_k^\tau} \sum_{i \in \mathcal{N}} \sum_{j \in \mathcal{N} \setminus \{i\}} V_{ij}[r_{ij}] \Big|_{\{\mathbf{R}\}_{\mathcal{N}}} = \frac{\partial^2}{\partial r_k^\sigma \partial r_k^\tau} \sum_{j \in \mathcal{N} \setminus \{k\}} V_{ik}[r_{ik}] \Big|_{\{\mathbf{R}\}_{\mathcal{N}}} \\ &= \sum_{j \in \mathcal{N} \setminus \{k\}} V_{jk}[R_{jk}] \left( -\delta_{\sigma\tau} \left( \frac{\kappa}{R_{jk}} + \frac{1}{(R_{jk})^2} \right) + \frac{R_{jk}^\sigma R_{jk}^\tau}{(R_{jk})^2} \left( \kappa^2 + \frac{3\kappa}{R_{jk}} + \frac{3}{(R_{jk})^2} \right) \right) \end{aligned} \quad (4.10)$$

where we subsequently used equations (4.6), (3.10), the fact that  $\frac{\partial}{\partial r_k^\sigma} V_{ij}[r_{ij}] = 0$  for  $k \neq i, j$ , the symmetry of  $V_{ij}[r_{ij}]$  in  $i$  and  $j$ , before applying this to the DLVO potential (2.17).  $\delta_{\sigma\tau}$  represents the Kronecker delta, which equals 1 if  $\sigma = \tau$  and 0 otherwise.

Note that  $M_{ij}^{\sigma\tau}$  is symmetric in  $i$  and  $j$ , but also in  $\sigma$  and  $\tau$ . This implies that all  $3 \times 3$  submatrices  $M_{ij}$  are real and symmetric and therefore diagonalizable. Because the trace of a matrix is invariant under unitary transformations, we can use equation (4.10) to obtain the sum of the eigenvalues  $\lambda_k^\sigma$  of  $M_{kk}$ :

$$\sum_{\sigma=1}^3 \lambda_k^\sigma = \text{Tr}[M_{kk}] = \kappa^2 \sum_{j \in \mathcal{N} \setminus \{k\}} V_{jk}[R_{jk}] = 2\kappa^2 u_M^{(k)}. \quad (4.11)$$

Here it is convenient to introduce  $u_M^{(k)} \equiv \frac{1}{2} \sum_{j \in \mathcal{N} \setminus \{k\}} V_{jk}[R_{jk}]$  as the potential energy of particle  $k$ . The factor 1/2 again prevents double counting of interactions.

This outcome should not come as a surprise. In fact, an alternative and perhaps more appealing derivation of this trace could have been given directly, making use of the property that  $V_{ij}$  satisfies the linearized Poisson-Boltzmann equation (2.9):

$$\begin{aligned} \text{Tr}[M_{kk}] &= \nabla_{\mathbf{r}_k}^2 U[\{\mathbf{r}\}_{\mathcal{N}}] \Big|_{\{\mathbf{R}\}_{\mathcal{N}}} = \frac{1}{2} \nabla_{\mathbf{r}_k}^2 \left( \sum_{i \in \mathcal{N}} \sum_{j \in \mathcal{N} \setminus \{i\}} V_{ij}[r_{ij}] \right) \Big|_{\{\mathbf{R}\}_{\mathcal{N}}} = \sum_{j \in \mathcal{N} \setminus \{k\}} \nabla_{\mathbf{r}_k}^2 V_{jk}[r_{jk}] \Big|_{\{\mathbf{R}\}_{\mathcal{N}}} \\ &= \sum_{j \in \mathcal{N} \setminus \{k\}} \nabla_{\mathbf{r}_{jk}}^2 V_{jk}[r_{jk}] \Big|_{\{\mathbf{R}\}_{\mathcal{N}}} = \kappa^2 \sum_{j \in \mathcal{N} \setminus \{k\}} V_{jk}[R_{jk}] = 2\kappa^2 u_M^{(k)}. \end{aligned} \quad (4.12)$$

We know that  $u_M = \frac{1}{N} \sum_{k \in \mathcal{N}} u_M^{(k)}$  and because stable crystals are very likely to have negative  $u_M$  (certainly for  $T=0$ ), this implies that at least the dominant  $u_M^{(k)}$  are negative, if not all. This will be confirmed by the results of subsection 4.3.1. Equation (4.11) shows that the majority of the  $\lambda_k^\sigma$  is likely to be negative as well. Indeed, this means that the curvature of the potential energy is negative and that the lattice sites constitute local maxima. It is clear that this negative curvature prohibits us from choosing infinite integration boundaries, since this would lead to a diverging integral in equation (4.7).

We approximate the curvature of the potential energy such that it is equal in all directions:

$$\lambda_k^\sigma \simeq \bar{\lambda}_k \equiv \frac{2\kappa^2 u_M^{(k)}}{3} \quad \text{for } \sigma = 1, 2, 3. \quad (4.13)$$

This expression is exact for isotropic crystals<sup>1</sup>, such as NaCl and CsCl. In the case of highly non-isotropic crystals, this approximation will lead to an error, especially for low packing fractions. However, the Lindemann criterion of subsection 4.2.2 shows that such low packing fractions cause the crystal to be unstable anyway.

The integral in the partition sum (4.7) can now be written as the product of  $N$  integrals over spherical volumes:

$$\int_{\mathcal{V}^{\text{RWS}}} d\mathbf{s}^{\mathcal{N}} \exp \left[ -\frac{\beta}{2} \sum_{i,j \in \mathcal{N}} \sum_{\sigma, \tau=1}^3 s_i^{\sigma} M_{ij}^{\sigma\tau} s_j^{\tau} \right] = \prod_{k \in \mathcal{N}} \underbrace{\int_{v_k^{\text{RWS}}} d\mathbf{s}_k \exp \left[ -\frac{\beta}{2} \bar{\lambda}_k \mathbf{s}_k^2 \right]}_{v_k^*}, \quad (4.14)$$

where the effective volumes  $v_k^*$  are computed via partial integration:

$$\begin{aligned} v_k^* &\equiv \int_{v_k^{\text{RWS}}} d\mathbf{s} \exp \left[ -\frac{\beta}{2} \bar{\lambda}_k \mathbf{s}^2 \right] = \int_0^{l^{\text{RWS}}} ds \, 4\pi s^2 \exp \left[ -\frac{\kappa^2 \beta u_M^{(k)}}{3} s^2 \right] \\ &= \begin{cases} \left( \frac{3\pi}{\kappa^2 \beta u_M^{(k)}} \right)^{3/2} \text{erf} \left[ \sqrt{\frac{\kappa^2 \beta u_M^{(k)}}{3}} l^{\text{RWS}} \right] - \frac{6\pi l^{\text{RWS}}}{\kappa^2 \beta u_M^{(k)}} \exp \left[ -\frac{\kappa^2 \beta u_M^{(k)}}{3} (l^{\text{RWS}})^2 \right] & \text{for } u_M^{(k)} > 0 \\ - \left( \frac{3\pi}{-\kappa^2 \beta u_M^{(k)}} \right)^{3/2} \text{erfi} \left[ \sqrt{-\frac{\kappa^2 \beta u_M^{(k)}}{3}} l^{\text{RWS}} \right] - \frac{6\pi l^{\text{RWS}}}{\kappa^2 \beta u_M^{(k)}} \exp \left[ -\frac{\kappa^2 \beta u_M^{(k)}}{3} (l^{\text{RWS}})^2 \right] & \text{for } u_M^{(k)} = 0 \\ - \left( \frac{3\pi}{-\kappa^2 \beta u_M^{(k)}} \right)^{3/2} \text{erfi} \left[ \sqrt{-\frac{\kappa^2 \beta u_M^{(k)}}{3}} l^{\text{RWS}} \right] - \frac{6\pi l^{\text{RWS}}}{\kappa^2 \beta u_M^{(k)}} \exp \left[ -\frac{\kappa^2 \beta u_M^{(k)}}{3} (l^{\text{RWS}})^2 \right] & \text{for } u_M^{(k)} < 0 \end{cases} \end{aligned} \quad (4.15)$$

Now we turn our attention to the integration region. We have said that we choose a spherical region and we now take its volume to be equal to that of what we call the Reduced Wigner-Seitz cell (explained below).

The Wigner-Seitz cell of a certain particle  $i$  is defined as the locus of all points in space that are closer to that particular particle than to any other particle in the crystal. This way the complete crystal is covered by  $N$  Wigner-Seitz cells, each around a single lattice site:

$$v_i^{\text{WS}} \equiv \left\{ \mathbf{r} \in \mathbb{R}^3 \mid |\mathbf{r} - \mathbf{R}_i| \leq |\mathbf{r} - \mathbf{R}_j| \, \forall j \in \mathcal{N} \right\}. \quad (4.16)$$

By requiring that a particle with radius  $a$  can only move within a region  $v_i^{\text{RWS}}$  such that the *whole* particle is completely in  $v_i^{\text{WS}}$ , we make sure that neighboring particles do not overlap. We call this subregion the Reduced Wigner-Seitz cell:

$$v_i^{\text{RWS}} \equiv \left\{ \mathbf{r} \in v_i^{\text{WS}} \mid \mathbf{r} + \mathbf{d} \in v_i^{\text{RWS}} \, \forall \mathbf{d}, |\mathbf{d}| \leq a \right\}. \quad (4.17)$$

For sufficiently symmetric crystals with same particle sizes, we have Wigner-Seitz cells with equal volumes  $v^{\text{WS}} = V/N \equiv 1/\rho = \tilde{v}/\eta$ , where  $\tilde{v} \equiv \eta/\rho$  and  $\eta$  representing the packing

<sup>1</sup>By isotropic crystals we mean crystals with a cubic unit cell that are symmetric in  $x$ ,  $y$  and  $z$ .

fraction (as defined in equation 4.51). In structures with all neighboring particles at equal distances, the Reduced Wigner-Seitz volumes scale as

$$v^{\text{RWS}} = v^{\text{WS}}[\eta] \left( 1 - \left( \frac{\eta}{\eta_{\text{max}}} \right)^{1/3} \right)^3, \quad (4.18)$$

such that the corresponding radius becomes:

$$l^{\text{RWS}} \equiv \left( \frac{3v^{\text{RWS}}}{4\pi} \right)^{1/3} = \left( \frac{3\tilde{v}}{4\pi\eta} \right)^{1/3} \left( 1 - \left( \frac{\eta}{\eta_{\text{max}}} \right)^{1/3} \right). \quad (4.19)$$

The Reduced Wigner-Seitz cell can be regarded as a lower bound to the region in which particles can move. We expect the real region of mobility to be somewhat larger, implying that our method underestimates the entropic contribution to the partition function.

When the method of a spherical integration region is compared to cubic integration regions or a numerical integration over the exact Reduced Wigner-Seitz cell, it turns out that the free energy differences between these methods are generally  $\lesssim 0.01k_B T$ , for NaCl, CsCl and the Tetragonal structure. This seems to validate our choice of a spherical volume.

All this leads to our final expression

$$\beta F_{\text{crystal}} \simeq \beta U_M - N \log \left[ \frac{v^*}{(\Lambda^*)^3} \right] \quad (4.20)$$

$$\text{with } v^* \equiv \left( \prod_{k \in \mathcal{N}} v_k^* \right)^{1/N} = \prod_{q=1}^n \left( 4\pi \int_0^{l^{\text{RWS}}} ds s^2 \exp \left[ -\frac{\kappa^2 \beta u_M^{(k)}}{3} s^2 \right] \right)^{1/n} \quad (4.21)$$

where  $l^{\text{RWS}}[\eta]$  is given by equation (4.19). Here,  $u_M^{(k)}[K, T^*, \eta]$  is determined as an intermediate step for computing  $U_M[K, T^*, \eta]$  and  $\Lambda^*$  is in fact irrelevant as it constitutes an arbitrary offset.

For clarity, we briefly sum up the assumptions and approximations applied in this lengthy derivation. By considering the colloidal crystal as a system of decoupled oscillators, each of which can move within its own sperical Reduced Wigner-Seitz cell, we were able to arrive at equation (4.20) as an expression for the Helmholtz free energy. These special Wigner-Seitz cells require a sufficiently symmetric crystal with all nearest neighbors at equal distance such that this volume is scalable when the packing fraction changes, and furthermore we treated the crystal as if it were isotropic.

#### 4.1.1.2 Alternative versions: $F_{\text{crystal}}^{(0)}$ , $F_{\text{crystal}}^{(1)}$

In these alternative versions for the free energy of the crystal we chose a slightly different approach to determining the effective integration volume  $v^*$ . The two things that changed are:

- a) Taking spherical integration volumes based on nearest neighbor distances between colloids,
- b) Making the approximation that wiggling a colloid about its lattice position does not change its potential energy. This is essentially equivalent to setting  $M = 0$  in the partition function (4.7) and this makes the effective integration volume just equal to the integration volume itself.

For  $F_{\text{crystal}}^{(0)}$  we therefore have

$$v_{(0)}^* \equiv \prod_{q=1}^n \left( \frac{4\pi}{3} (d_q/2)^3 \right)^{1/n}, \quad (4.22)$$

with  $d_q$  the distance of particle  $q$  to its nearest neighbor. We explicitly note that this is the surface-to-surface distance between neighboring colloids:

$$d_q = \min_{i \in U} [|\mathbf{r}_i - \mathbf{r}_q| - a_i - a_q], \quad (4.23)$$

where  $|\mathbf{r}_i - \mathbf{r}_q|$  is always taken modulo the unit vectors that span the unit cell of the particular unit cell. Whereas the center-to-center distances simply scale with  $\eta^{-1/3}$ , the surface-to-surface distances require an extra calculation step when packing fraction is changed, because this could cause another neighbor to come closer than the original nearest neighbor.

$F_{\text{crystal}}^{(1)}$  mainly serves to compare the original  $F_{\text{crystal}}$  to  $F_{\text{crystal}}^{(0)}$  and takes only a) into account but not b), giving the effective volume:

$$v_{(1)}^* \equiv \prod_{q=1}^n \left( 4\pi \int_0^{d_q/2} dr r^2 \exp \left[ -\frac{\kappa^2 u_q}{3} r^2 \right] \right)^{1/n}. \quad (4.24)$$

### 4.1.2 Fluid phase

Since these colloidal crystals are formed out of a colloidal suspension, they have to be in coexistence with a colloidal fluid phase, whose Helmholtz free energy will be treated right now. We looked at several different models for this fluid free energy (see diagram 4.2), but the main two expressions that we will refer to are  $F_{\text{fluid}}^{(0)}$  and  $F_{\text{fluid}}^{(3)}$ . The former is a somewhat crude approximation which uses a Madelung-like term for the electrostatic interactions, and the latter is a more realistic version derived through thermodynamic integration. We will briefly refer to two other versions (Truncated Boltzmann and Better Ansatz) that are related to  $F_{\text{fluid}}^{(3)}$ , but these have not (yet) led to better results.

Both models are based on the Helmholtz free energy of a hard-sphere fluid as given by the Carnahan-Starling approximation for 2 particle species:

$$\frac{\beta F_{\text{fluid}}^{\text{HS}}}{N} = \log[\rho \Lambda^3] - 1 - \log[2] + \frac{4\eta - 3\eta^2}{(1 - \eta)^2}. \quad (4.25)$$

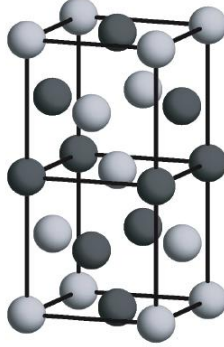


Figure 4.1: Tetragonal structure composed of symmetric AB mixture. The unit cell consists of two stacked FCC unit cells, but with  $A$  and  $B$ -particles at the proper lattice sites. Picture provided by A.-P. Hynninen[17]

The first two terms are just the ideal gas terms for equal particles and the  $-\log[2]$  term is associated with the entropy of mixing  $\sum_{i=A,B} x_i \log[x_i]$  for 2 different species, with  $N_A = N_B = N/2$ . The last one was added by Carnahan and Starling to account for the hard-sphere repulsions in the fluid, caused by the finite particle sizes [37].

#### 4.1.2.1 Simple approach: $F_{\text{fluid}}^{(0)}$

For our first and simplest model of the fluid, we assume that the nature of the electrostatic interactions resembles that in the crystal phase and that we are therefore allowed to add a single Madelung-like term to the hard-sphere expression (4.25) in order to obtain the Helmholtz free energy of the fluid phase:

$$\frac{\beta F_{\text{fluid}}^{(0)}}{N} = \frac{\beta F_{\text{fluid}}^{\text{HS}}}{N} + \frac{\beta U_M^{\text{Tetra}}}{N} = \log[\rho \Lambda^3] - 1 - \log[2] + \frac{4\eta - 3\eta^2}{(1 - \eta)^2} + \frac{\beta U_M^{\text{Tetra}}[\eta]}{N}, \quad (4.26)$$

where  $U_M^{\text{Tetra}}$  is the Madelung energy of a Tetragonal structure at the required  $\eta$ .

One can see that this has to be a reasonable approximation at least in the low temperature limit, because the electrostatic part of  $F = F^{\text{HS}} + F^{\text{ELEC}}$  reduces to

$$\lim_{T \downarrow 0} F^{\text{ELEC}} = U[\{\mathbf{r}\}_{\mathcal{N}}] \approx U_M \quad (4.27)$$

in that case, whereas the hard-sphere contribution vanishes altogether. Moreover, in the high temperature limit the electrostatic terms become irrelevant altogether, since the DLVO potential (2.17) is now vanishing for  $r \geq a_i + a_j$  (via a vanishing Bjerrum length), thereby equalling the hard-sphere potential:

$$\lim_{T \rightarrow \infty} \beta V_{ij}[r] = \begin{cases} 0 & \text{for } r \geq a_i + a_j \\ \infty & \text{for } r < a_i + a_j. \end{cases} \quad (4.28)$$

At intermediate temperature however, the  $-TS^{\text{ELEC}}$  term cannot be neglected and  $F_{\text{fluid}}^{(0)}$  is likely to become worse, but this is looked into when we compare this model to  $F_{\text{fluid}}^{(1)}$ , which is defined in the next subsection.

Actually, since this method is again based on Madelung energies it requires us to impose a certain structure on the fluid phase. The rather arbitrary looking choice of Tetragonal is justified by the fact that this is one of the most spherically symmetric structures that is possible. In the Tetragonal structure each particle is surrounded by a layer of 12 nearest neighbors, which are all located at the same distance, at least in the current case of equal particle sizes. As can be seen in figure 4.1, 8 of these nearest neighbors are of the opposite species and the other 4 belong to the same one. We expect that this first approximation comes fairly close to the real structure of the fluid.

A modified version of this model would be to use alternative structures instead of the default Tetragonal, and each time selecting the structure with minimal free energy. In principle this could mean an improvement of the theory and, in fact, we did some quick calculations that showed lower free energies for many circumstances, but nonetheless we decided not to pursue this method. Our main reason was that it would make it harder to compare different points in parameter space, if for each point it turned out there was a different optimal structure. It would also give some practical computational problems, for example when we are doing common tangent construction and  $F_{\text{fluid}}[\eta]$  does not behave smoothly due to the fact that it depends on different structures for different packing fractions.

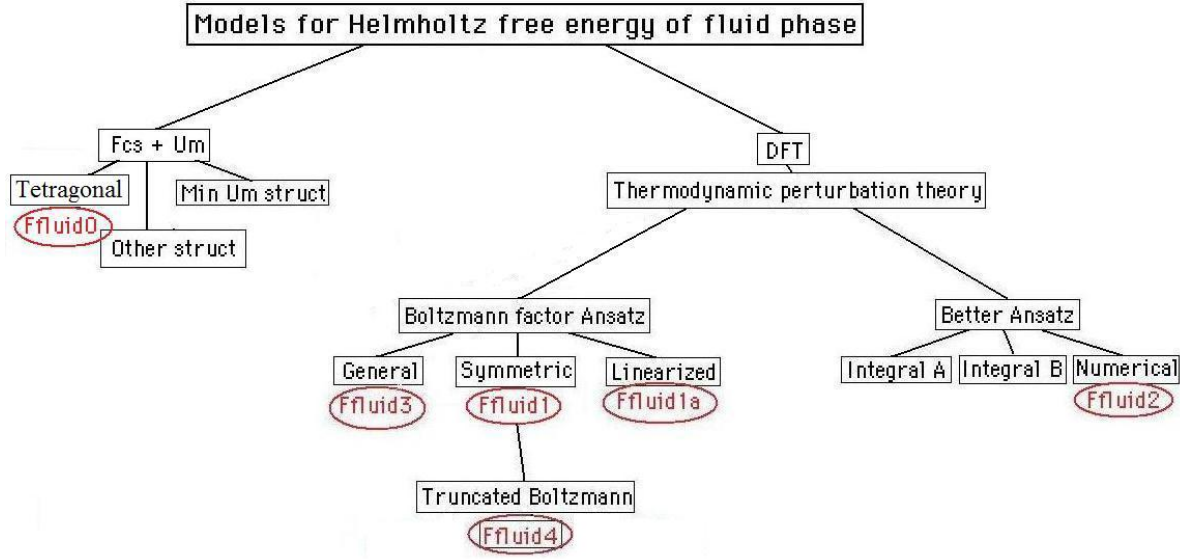
We have now constructed a very simple model that is easy to use and that allows to quickly calculate and compare Helmholtz free energies. We expect it not to give very accurate results but consider it as a good upper bound for the real fluid free energy (which also incorporates the neglected  $-TS^{\text{ELEC}}$  term and optimal fluid structure). In reality this would imply that the fluid is more stable than follows from our calculations and that it therefore also has a larger stability region than we will find. These discrepancies are expected to be largest for intermediate temperature and high packing fractions (in the latter case  $F_{\text{fluid}}$  depends more on the specific structure).

#### 4.1.2.2 Derive Thermodynamic Perturbation Theory method

$F_{\text{fluid}}^{(0)}$  may be a very simple and useful model, but during our research we found out that especially the intermediate temperature regime posed a problem for its accuracy. Though this will be discussed later when the results are presented, here we take a more thorough approach, that gives a much better theoretical basis than  $F_{\text{fluid}}^{(0)}$ .

First we use density functional theory to derive a method for thermodynamic perturbation theory and after that we will apply this to certain assumptions about the ‘structure’ of the colloidal fluid in order to arrive at specific Helmholtz free energies. Again, the idea is to obtain a model for the fluid that is based on the hard-sphere expression and an additional term accounting for electrostatic interactions.



Figure 4.2: Models for  $F_{\text{fluid}}$ 

We start off with a general free energy functional for the fluid:

$$\beta F[\rho] = \int d\mathbf{r} \sum_i \rho_i[\mathbf{r}] (\log[\rho_i[\mathbf{r}] \Lambda_i^3] - 1) + \beta F^{\text{DLVO}}[\rho] \quad (4.29)$$

that consists of a multi-component ideal gas part and a second term generated by the interaction potential. Taking the functional derivative with respect to the energy gives:

$$\begin{aligned} \frac{\delta \beta F^{\text{DLVO}}}{\delta \beta \phi_{ij}^{\text{DLVO}}[\mathbf{r}, \mathbf{r}']} &= -\frac{1}{Z} \frac{1}{(\Lambda^*)^{3N}} \int d\mathbf{r}^N \frac{\delta \exp \left[ -\frac{1}{2} \sum_{i \neq j} \beta \phi_{ij}^{\text{DLVO}}[\mathbf{r}_i, \mathbf{r}_j] \right]}{\delta \beta \phi_{ij}[\mathbf{r}, \mathbf{r}']} \\ &= \frac{1}{Z} \frac{1}{(\Lambda^*)^{3N}} \int d\mathbf{r}^N \frac{1}{2} \left( \sum_{i \neq j} \delta(\mathbf{r} - \mathbf{r}_i) \delta(\mathbf{r}' - \mathbf{r}_j) \right) \exp \left[ -\frac{1}{2} \sum_{i \neq j} \beta \phi_{ij}^{\text{DLVO}}[\mathbf{r}_i, \mathbf{r}_j] \right] \\ &= \frac{1}{2} \left\langle \sum_{i \neq j} \delta(\mathbf{r} - \mathbf{r}_i) \delta(\mathbf{r}' - \mathbf{r}_j) \right\rangle = \frac{1}{2} \rho_{ij}^{(2)}[\mathbf{r}, \mathbf{r}'] = \frac{1}{2} \rho_i[\mathbf{r}] \rho_j[\mathbf{r}'] g_{ij}[\mathbf{r}, \mathbf{r}']. \end{aligned} \quad (4.30)$$

In the last steps we made use of the definition of the correlation functions, as given in equations (A.21) and (A.22).

For clarity, we note that the regular DLVO potential from equation (2.17) is temporarily called  $\phi_{ij}^{\text{DLVO}}$  (sometimes abbreviated as  $\phi_{ij}$ ) instead of  $V_{ij}$  and we can divide it into a hard-

sphere part and an electrostatic part:

$$\phi_{ij}^{\text{DLVO}} = \phi_{ij}^{\text{HS}} + \phi_{ij}^{\text{ELEC}} \quad (4.31)$$

$$\beta\phi_{ij}^{\text{HS}}[\mathbf{r}_i, \mathbf{r}_j] \equiv \begin{cases} 0 & \text{for } r \geq a_i + a_j \\ \infty & \text{for } r < a_i + a_j \end{cases} \quad (4.32)$$

$$\beta\phi_{ij}^{\text{ELEC}}[\mathbf{r}_i, \mathbf{r}_j] \equiv \begin{cases} Z_i Z_j \lambda_B \frac{\exp[\kappa(a_i + a_j)]}{(1 + \kappa a_i)(1 + \kappa a_j)} \frac{\exp[-\kappa r]}{r} & \text{for } r \geq a_i + a_j \\ 0 & \text{for } r < a_i + a_j \end{cases} \quad (4.33)$$

Now we introduce a perturbation parameter  $\lambda$  and define the interaction potential

$$\phi_{ij,\lambda}^{\text{DLVO}} \equiv \phi_{ij}^{\text{HS}} + \lambda\phi_{ij}^{\text{ELEC}} \quad \text{with } \lambda \in [0, 1] \quad (4.34)$$

such that this system is tuned between hard-spheres ( $\lambda = 0$ ) and the charged colloidal suspension that we are investigating ( $\lambda = 1$ ). The Yukawa potential  $\phi^{\text{ELEC}}$  is thus considered as a perturbation to the hard-sphere system. Note that this new system is equivalent to our original one with colloidal charges  $Z_i$  substituted by  $\sqrt{\lambda}Z_i$ . We denote its free energy by  $F_\lambda^{\text{DLVO}}$ .

Writing  $F_\lambda^{\text{DLVO}}$  again as a free energy functional, its derivative to  $\lambda$  becomes:

$$\begin{aligned} \frac{d\beta F_\lambda^{\text{DLVO}}}{d\lambda} &= \int d\mathbf{r} \int d\mathbf{r}' \sum_{i,j} \left. \frac{\delta\beta F^{\text{DLVO}}}{\delta\beta\phi_{ij}^{\text{DLVO}}[\mathbf{r}, \mathbf{r}']} \right|_{\phi_\lambda^{\text{DLVO}}} \beta\phi_{ij}^{\text{ELEC}}[\mathbf{r}, \mathbf{r}'] \\ &= \frac{1}{2} \int d\mathbf{r} \int d\mathbf{r}' \sum_{i,j} \rho_i[\mathbf{r}] \rho_j[\mathbf{r}'] \beta\phi_{ij}^{\text{ELEC}}[\mathbf{r}, \mathbf{r}'] g_{ij}^\lambda[\mathbf{r}, \mathbf{r}'] \end{aligned} \quad (4.35)$$

where we used equation (4.30) for the second equality. Actually, this expression represents the expectation value  $\langle \beta F^{\text{ELEC}} \rangle_\lambda$ .

Now we see that  $F$  is given by:

$$F = \underbrace{F^{\text{IdealGas}} + F_{\lambda=0}^{\text{DLVO}}}_{F^{\text{HS}}} + \underbrace{\int_0^1 d\lambda \frac{\partial F_\lambda^{\text{DLVO}}}{\partial \lambda}}_{F^{\text{ELEC}}}, \quad (4.36)$$

with  $F^{\text{HS}}$  well-known from other research and  $F^{\text{ELEC}}$  is what we actually want to calculate.

Applying the restriction that we are considering a homogeneous system:

$$\rho_i = \text{constant}, \quad (4.37)$$

and making use of the fact that  $g[r]$  and  $\psi[r]$  are spherically symmetric and therefore depend only on the absolute argument  $|\mathbf{r} - \mathbf{r}'|$  (translational invariance), we arrive at the important expression:

$$\boxed{\beta F^{\text{ELEC}} = \int_0^1 d\lambda \frac{\partial F_\lambda^{\text{DLVO}}}{\partial \lambda} = 2\pi V \sum_{i,j=A,B} \rho_i \rho_j \int dr r^2 \beta\phi_{ij}^{\text{ELEC}}[r] \int_0^1 d\lambda g_\lambda^{ij}[r]}. \quad (4.38)$$

Here  $g_\lambda^{ij}[r]$  is the pair correlation function for colloids with charges  $\sqrt{\lambda}Z_i e$  and  $\sqrt{\lambda}Z_j e$ . For  $\lambda = 1$  it reduces to the regular pair correlation function  $g^{ij}[r]$  that describes the conditional probability density of finding a  $j$ -particle at  $\mathbf{r}$  given that there is an  $i$ -particle at the coordinate origin.

Our task is now to devise a realistic  $g_\lambda^{ij}[r]$ . This has to satisfy at least the properties

$$\lim_{r \rightarrow \infty} g_{kl}[r] = 1 \quad \forall k, l. \quad (4.39)$$

$$g_{AB}[r] = g_{BA}[r], \quad (4.40)$$

$$g[r] = 0 \quad \text{for } r < a_i + a_j \quad (4.41)$$

of which the first two follow from equation (A.22).

#### 4.1.2.3 Boltzmann factor Ansatz: $F_{\text{fluid}}^{(3)}$

So far, equation (4.38) represents an exact expression, at least for the homogenous fluid, but the precise  $g_{ij}[\mathbf{r}, \mathbf{r}']$  is unknown. Therefore we choose a mean field-like approach that assumes smeared out pair correlation functions  $g_{ij}[r]$  proportional to a Boltzmann factor:

$$\begin{aligned} g_{ij}^\lambda[r] &\equiv \exp \left[ -\beta \phi_{ij}^{\text{DLVO}, \lambda}[r] \right] = \exp \left[ -\beta \phi_{ij}^{\text{HS}}[r] \right] \exp \left[ -\lambda \beta \phi_{ij}^{\text{ELEC}}[r] \right] \\ &= \begin{cases} \exp \left[ -\lambda \beta \phi_{ij}[r] \right] & \text{for } r \geq a_i + a_j \\ 0 & \text{for } r < a_i + a_j. \end{cases} \end{aligned} \quad (4.42)$$

such that properties (4.39) and (4.41) are satisfied, the former because of  $\lim_{r \rightarrow \infty} \phi_{ij}^{\text{DLVO}}[r] = 0$ . Working out equation (4.38) we obtain:

$$\begin{aligned} \beta F^{\text{ELEC}} &= 2\pi V \sum_{i,j=A,B} \rho_i \rho_j \int_{a_i+a_j}^{\infty} dr r^2 \beta \phi_{ij}[r] \int_0^1 d\lambda \exp \left[ -\lambda \beta \phi_{ij}[r] \right] \\ &= 2\pi V \sum_{i,j=A,B} \rho_i \rho_j \int_{a_i+a_j}^{\infty} dr r^2 (1 - \exp \left[ \beta \phi_{ij}[r] \right]), \end{aligned} \quad (4.43)$$

making the total free energy:

$$\boxed{\beta F_{\text{fluid}}^{(3)} = \beta F_{\text{fluid}}^{\text{HS}} + V \sum_{i,j} \rho_i \rho_j B_{ij}} \quad (4.44)$$

where the second virial coefficient  $B_{ij}$  is defined in terms of the Mayer function  $f_{ij}$ :

$$B_{ij} \equiv -2\pi \int_{a_i+a_j}^{\infty} dr r^2 f_{ij}[r] \quad (4.45)$$

$$f_{ij}[r] \equiv \exp \left[ \beta \phi_{ij}[r] \right] - 1 \quad (4.46)$$

In our numerical calculations we use the Mansoori potential [38] for the hard-sphere term of  $F_{\text{fluid}}^{(3)}$ , since this is a generalization of the Carnahan-Starling expression of the fluid free energy (as can be easily derived from appendix D). This makes equation (4.44) valid for the asymmetric case as well.

In the symmetric case this free energy evaluates to what we call  $F_{\text{fluid}}^{(1)}$ :

$$\frac{\beta F_{\text{fluid}}^{(1)}}{N} = \log[\rho\Lambda^3] - 1 - \log[2] + \frac{4\eta - 3\eta^2}{(1 - \eta)^2} - 4\pi\rho \int_{2a}^{\infty} dr r^2 \sinh^2 \left[ \frac{\beta\phi[r]}{2} \right] \quad (4.47)$$

and for sufficiently high temperature it even reduces to:

$$\frac{\beta F_{\text{fluid}}^{(1a)}}{N} = \log[\rho\Lambda^3] - 1 - \log[2] + \frac{4\eta - 3\eta^2}{(1 - \eta)^2} - \frac{\pi\rho\lambda_B^2}{2\kappa} \left( \frac{Z}{1 + \kappa a} \right)^4 \quad \text{for } T^* \gg \frac{1}{2}. \quad (4.48)$$

as can be seen in appendix C.3.

For completeness we also refer to appendices C.4 and C.5 for two other approaches to calculate the fluid free energy ('Truncated Boltzmann' and 'Better Ansatz'), but eventually both of these were abandoned.

## 4.2 Methods

### 4.2.1 Relevant parameters

Including entropy in our calculations adds an extra temperature parameter to the system, compared to chapter 3. Theoretically, colloidal masses  $m_A$  and  $m_B$  contribute to the free energy as well, via their role in  $\Lambda^*$  (see equation (4.11)). However, this will only have influence on phase diagrams when we are comparing structures of different stoichiometries in the case of *unequal*  $m_A, m_B$ . Otherwise,  $\Lambda^*$  will just be an irrelevant constant, the same for all structures and phases.

The choice of only investigating the symmetric case will again drastically reduce the number of relevant parameters. Instead of considering the complete parameter space ( $\kappa, a \equiv a_A = a_B, Z \equiv Z_A = Z_B, N_A = N_B = N/2, V, \lambda_B[T], m \equiv m_A = m_B$ ) we only need to draw our attention to three dimensionless parameters:

$$K \equiv \kappa(a_A + a_B) = 2\kappa a \quad (4.49)$$

$$T^* \equiv \frac{(1 + \kappa a_A)(1 + \kappa a_B)(a_A + a_B)}{Z_A Z_B \lambda_B} = \frac{2a(1 + \kappa a)^2}{Z^2 \lambda_B} \quad (4.50)$$

$$\eta \equiv \frac{4\pi}{3} \frac{N_A a_A^3 + N_B a_B^3}{V} = \frac{4\pi a^3}{3} \frac{N}{V}. \quad (4.51)$$

where the new parameter  $T^*$  is called the reduced temperature. With the exception of subsection 4.3.3, in which  $Q \neq 1$ , all other reduced parameters are fixed by the symmetric case conditions:  $Q = 1, q = 1, x = 1/2$  and  $y \equiv m_A/(m_A + m_B) = 1/2$ .

Notice that the definition of the reduced temperature  $T^*$  is chosen such that it equals the inverse potential energy of 2 oppositely charged particles at contact:  $T^* = (\beta V_{AB}[a_A + a_B])^{-1}$ , which is a very nice property to work with. Since  $\lambda_B$  is proportional to the inverse temperature (recall equation (2.2)), it makes sense to call  $T^*$  a reduced temperature.

To be precise,  $\kappa$  depends on temperature as well, as can be seen from equations (2.1) and (2.2). Consequently, the same goes for  $K$ . In our calculations however, we impose a certain value for  $K$ , keeping it constant as temperature changes. In practice this means that at different (reduced) temperatures the ion concentrations might vary in order to ensure that screening parameter  $K$  has the imposed value.

### 4.2.2 Lindemann criterion

Due to the contribution of entropy, crystals will not be dense-packed at nonzero temperatures, as argued before. Coexistence with a fluid or a gas phase could therefore cause these structures to become quite dilute, i.e. having considerably large lattice spacings.

In reality, the colloidal thermal motions will often be too big to ensure that the lattice structure is retained at low density, to such an extent that the solid cannot be called crystalline anymore. This is very common in ordinary crystals and it has even led to the Lindemann criterion [39], which is a somewhat heuristic measure for the stability of crystalline structures that highly depends on temperature and density. It states that a crystal can only be stable if

$$\sqrt{\langle s^2 \rangle} < 0.1 \rho^{-1/3} \quad (4.52)$$

is roughly satisfied, where the left hand side is the root mean square of the particle's displacement  $s$  from its average lattice position.

In the approach shown in subsection 4.1.1, we calculate this for a single particle  $q$  using

$$\langle s_q^2 \rangle = \frac{1}{v_q^*} \int_0^{l^{\text{RWS}}} ds \, 4\pi s^4 \exp \left[ -\frac{\kappa^2 \beta u_M^{(q)}}{3} s^2 \right], \quad (4.53)$$

which evaluates into an analytic expression that we will not display.

Although our system is not completely equivalent to an ordinary crystal, we still apply the Lindemann criterion to determine in a simple way at what packing fraction the crystal becomes thermally unstable and call this the Lindemann packing fraction,  $\eta_L$ . For  $\eta < \eta_L$  the crystal is considered necessarily unstable and for that matter we do not pay any attention to the theoretical results in this range.

Not only is the crystal structure falling apart at large lattice spacings, our theory also starts to break down in such cases because the second order Taylor expansion in equation (4.5) becomes more and more inaccurate. Applying the Lindemann criterion makes sure though that we do not need to worry about that.

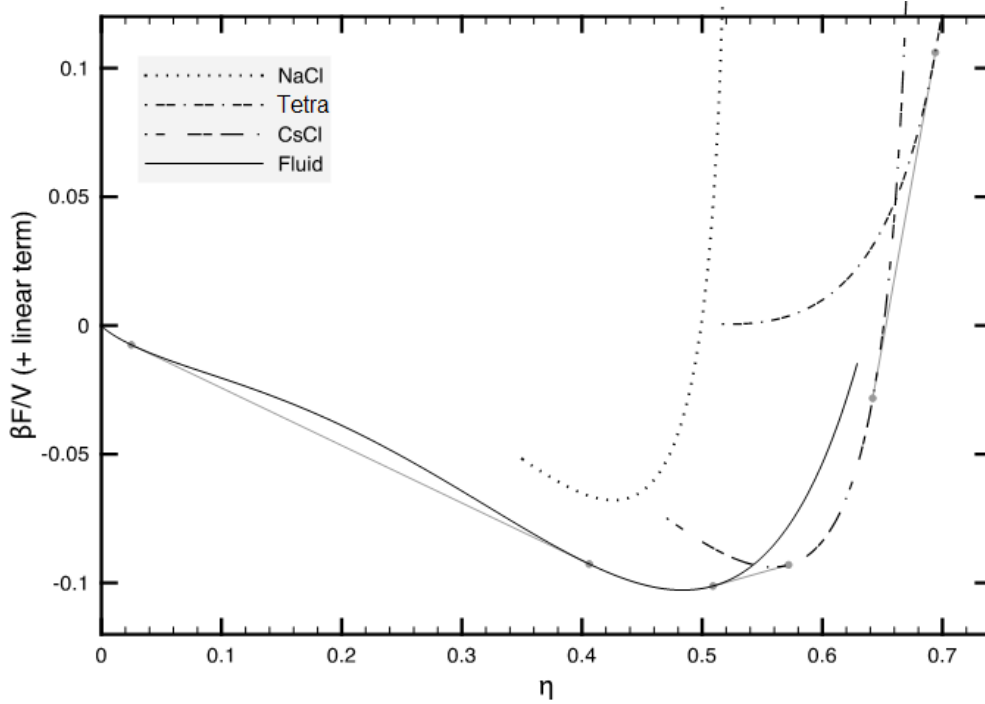


Figure 4.3: Helmholtz free energies  $\beta F/V$  (not dimensionless) as function of packing fraction  $\eta$ , for 3 different crystal structures and the ‘fluid’ phase, the latter being separated into a dilute gas phase and a liquid phase. Common Tangent lines (straight grey lines) denote gas-liquid, liquid-solid and solid-solid phase transitions. It is clear that NaCl is metastable in this situation. Note that the crystal free energies asymptotically go to infinity due to the lack of entropic degrees of freedom of dense-packed crystals. Calculations were performed at  $K = 3$  and  $T^* = 0.15$  for the symmetric case (using  $F_{\text{crystal}}$  and  $F_{\text{fluid}}^{(0)}$ ). For clarity, a linear term  $-\beta p_0 + (\beta \mu_0 / \tilde{v})\eta$  has been added to  $\beta F/V$ . This does not change the Common Tangent method, but  $\mu$  and  $p$  cannot be read off directly from the tangent lines in this diagram. To give an idea: free energy differences  $\beta F/N$  are of the order of a few  $k_B T$ .

### 4.2.3 Common Tangent Construction

Thermodynamic equilibrium in the  $NVT$  ensemble requires that coexisting phases  $\alpha$  and  $\beta$  have equal chemical potentials  $\mu$  and pressures  $p$ :

$$\mu_\alpha = \mu_\beta = \mu \quad (4.54)$$

$$p_\alpha = p_\beta = p. \quad (4.55)$$

We will now derive the Common Tangent Construction method for determining phase coexistence, from the definitions of  $\mu$  and  $p$ :

$$\mu[N, V, T] \equiv \frac{\partial F[N, V, T]}{\partial N} \quad (4.56)$$

$$p[N, V, T] \equiv \frac{\partial F[N, V, T]}{\partial V}. \quad (4.57)$$

Writing  $\mu$  and  $p$  in terms of the free energy per volume  $f[\rho, T] \equiv F[N, V, T]/V$  and the density  $\rho \equiv N/V$ , gives:

$$\mu[\rho, T] = \frac{\partial f[\rho, T]}{\partial \rho} \quad (4.58)$$

$$p[\rho, T] = -f[\rho, T] + \rho\mu[\rho, T]. \quad (4.59)$$

Looking at phases  $\alpha$  and  $\beta$  as two coexisting subsystems, whose properties are marked by the proper subscripts, the thermodynamic equilibrium conditions lead us to:

$$\mu = \frac{\partial f_\alpha}{\partial \rho_\alpha} = \frac{\partial f_\beta}{\partial \rho_\beta} \quad (4.60)$$

$$\rho_\alpha \mu - f_\alpha = \rho_\beta \mu - f_\beta \quad (4.61)$$

and eliminating  $\mu$  from these equations, we arrive at:

$$\frac{\partial f_\alpha}{\partial \eta_\alpha}[\eta_\alpha] = \frac{\partial f_\beta}{\partial \eta_\beta}[\eta_\beta] = \frac{f_\alpha[\eta_\alpha] - f_\beta[\eta_\beta]}{\eta_\alpha - \eta_\beta} \quad (4.62)$$

where we were allowed to replace the density  $\rho$  by the packing fraction  $\eta$  since they are proportional with factor  $\tilde{v} \equiv \frac{\eta}{\rho} = \frac{4\pi}{3}((1-x)a_A^3 + xa_B^3)$  (see equation (4.51)).

Equation (4.62) implies that for coexisting phases  $\alpha$  and  $\beta$ , the tangent lines to points  $(\eta_\alpha, f_\alpha[\eta_\alpha])$  and  $(\eta_\beta, f_\beta[\eta_\beta])$  in an  $f[\eta]$ -plot are coinciding. This can easily be seen from figure 4.3, in which we plotted the  $\beta F/V$  for 3 different phases, that are connected via common tangent lines. The system tends to minimize its total free energy and it is clear that, when the system's packing fraction  $\eta$  is between  $\eta_\alpha$  and  $\eta_\beta$ , this can only be done by separating into a phase  $\alpha$  at packing fraction  $\eta_\alpha$  and a denser phase  $\beta$  at  $\eta_\beta$ .

Note that in an  $f[\eta]$ -plot the (common) tangent line to a point is characterized by slope  $\frac{\partial f}{\partial \eta} = \frac{\mu}{\tilde{v}}$  and intercept  $f - \eta \frac{\partial f}{\partial \eta} = -p$ .

## 4.3 Results and discussion

After first showing a comparison of the most important models for the Helmholtz free energy, that were defined in the theory section of this chapter, we will present and discuss the results of several sub-investigations that were done for the finite temperature symmetric case. But

before actually looking at these results, let us first give an idea about which subsections are relevant to the main line of research and which can be regarded as mere side tracks.

Subsection 4.3.1 (mobility of single colloids) shows some more detail about  $F_{\text{crystal}}$  and also serves to validate its approach. Sub 4.3.2 (gas-liquid binodal) looks at first sight as a side track, but by comparing its results to other research it also becomes relevant for the validity of  $F_{\text{fluid}}^{(0)}$ . Subs 4.3.3 (NaCl-CsCl boundary) and 4.3.4 (Phase diagrams in  $\eta - T$  plane) present the phase diagrams we are actually interested in and the latter can even be considered as the most important part of this research. Sub 4.3.5 (CuAu-CsCl phase transition) is regarded as a side step that gives more detail about the  $\eta - T$  phase diagram and is also interesting in itself. Finally, sub 4.3.6 (variable cell volume) is important as well because it can improve the crystal model by shedding more light on the contribution of entropy on the final  $\eta - T$  phase diagram.

We finish this section with a few general remarks about these results all together.

### 4.3.1 Mobility of single colloids

Let us look at what happens inside a colloidal crystal by focusing on a single particle in the lattice. When we fix all other particles on their lattice sites and move this particle around, we obtain its (quadratically approximated) potential energy

$$\beta u^{(1)}[\mathbf{s}] = \beta u_M + \frac{\kappa^2 \beta u_M}{3} \mathbf{s}^2 \quad \text{for } |\mathbf{s}| \leq s_{\text{max}} \quad (4.63)$$

as a function of its displacement vector  $\mathbf{s}$ . This is the same expression as  $F_{\text{crystal}}^{(1)}$  is based on, contrary to  $F_{\text{crystal}}^{(0)}$ , which neglects the quadratic term. In stable crystals particles are likely to be surrounded by neighbors of opposite charges and these attractive neighbor-neighbor interactions make sure that  $\beta u^{(1)}$  has its maximum at  $\mathbf{s} = \mathbf{0}$ , as mentioned earlier.

In figure 4.4 this potential energy is plotted for variable packing fraction and the consequences of varying this packing fraction are quite clear. In the first place, a less dense crystal has less negative Madelung energy because of weaker interactions (see also figure 3.3).

Secondly, the maximum displacement  $s_{\text{max}}$ , that we take to be the nearest neighbor distance in this plot, increases of course with decreasing packing fraction. To be precise, for equal sized particles its relation with  $\eta$  is  $s_{\text{max}} = 2a \left( (\eta_{\text{max}}/\eta)^{1/3} - 1 \right)$ .

And thirdly, note that the curvature of the graphs in figure 4.4 is proportional to the Madelung energy  $u_M$ . This is because of the approximation we derived in equation (4.13), that holds for isotropic crystals and relatively small displacements  $\mathbf{s}$ .

From these intermediate results it is immediately clear that there has to be a certain value for  $\eta$  for which entropy and electrostatics together have a maximal contribution to the partition sum. At  $\eta = \eta_{\text{max}}$  we obviously find a vanishing  $\int d\mathbf{s}$  integral in equation (4.15) because of the vanishing integration volume (since  $s_{\text{max}} = 0$ ), whereas at lower  $\eta$  it is the integrand  $\exp[-\beta u]$  that becomes much smaller.



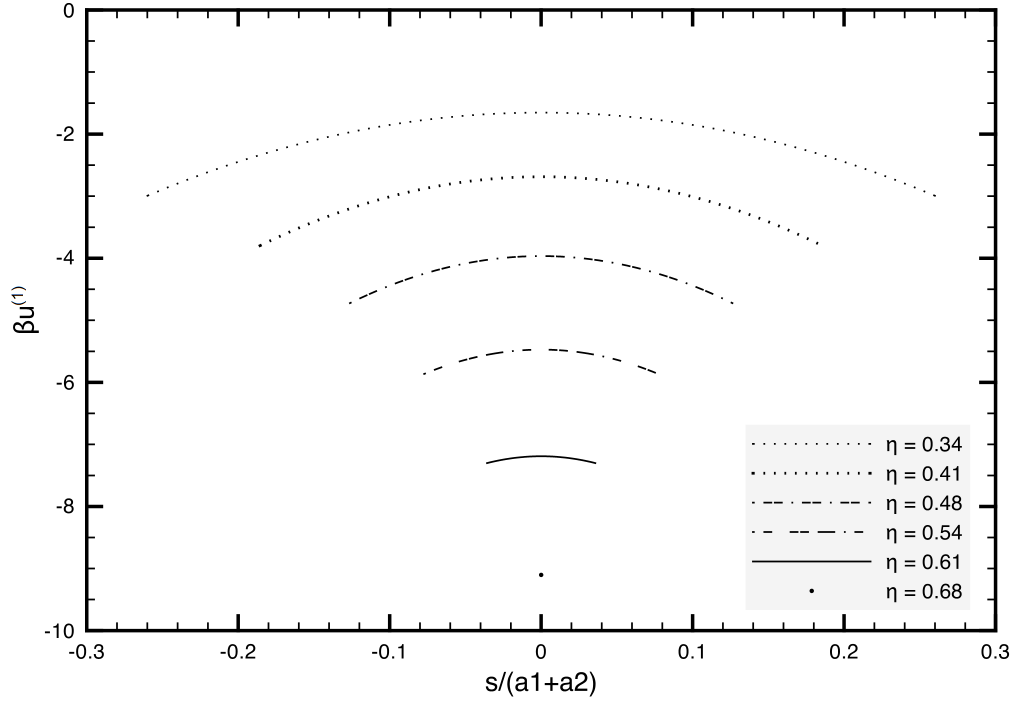


Figure 4.4: Potential energy  $\beta u^{(1)}$  of a single particle as function of its displacement  $s$  away from its lattice site, while all other particles are kept fixed at the sites of a CsCl lattice. The displacement is taken along one of the standard lattice vectors (recall that CsCl is isotropic and has a cubic unit cell, see figure 3.8(b)). The calculations were done for fixed  $K = 6$ ,  $Q = 1$ ,  $q = 1$  and the packing fraction was varied from  $\eta_{\max}^{\text{CsCl}}/2$  to  $\eta_{\max}^{\text{CsCl}} \approx 0.68$ . The potential walls that arise due to hard-sphere repulsions at  $s = s_{\max}$  have not been drawn, for clarity. Note that, according to the Lindemann criterion, the crystal becomes unstable at  $\eta \lesssim 0.5$ .

We find that the Lindemann packing fraction  $\eta_L$  typically lies around  $0.7\eta_{\max}$  for Tetragonal, CsCl and NaCl, implying that these crystals become thermally unstable at lattice spacings  $\gtrsim 113\%$  that of the dense-packed structure. In figure 4.4 this amounts to  $\eta_L^{\text{NaCl}} \approx 0.5$ .

At first sight, the potential maximum at  $s = 0$  seems to indicate an unstable crystal in which particles are likely to move away from their lattice sites towards their neighbors. A related property would be that the system theoretically has a larger root mean squared value  $\sqrt{\langle s^2 \rangle}$  at low temperatures, which could play a role in coagulation in such circumstances. However, in our temperature regime the thermal energy of the system makes sure that there is enough mobility of particles, since the energy difference between a colloid sitting at the lattice site and one at maximal displacement is generally of the order of  $1 k_B T$  or less. Low packing fractions might give larger differences, but these are irrelevant because of the Lindemann criterion. On average the colloids will still be situated at  $s = 0$ .

Precisely because of the fact that the just mentioned energy difference is usually not more than  $1 k_B T$ , we are allowed to conclude that  $F_{\text{crystal}}^{(0)}$  is only slightly less precise for most

circumstances, though being much simpler than  $F_{\text{crystal}}$ . During this research we have been using  $F_{\text{crystal}}$  as the standard method and with hindsight we can say that this was not really necessary. However, many of the results of the next sections have been done with this model and this is the way they are presented (after all, they are slightly more precise).

### 4.3.2 Gas-liquid binodal

In order to assess the precision of the simple model  $F_{\text{fluid}}^{(0)}$  that we use for the Helmholtz free energy of the fluid, we will now focus briefly on the phase behavior of the fluid alone, or in other words on the gas-liquid phase separation that takes place for low screening.

Diagram 4.5(a) shows some results of this investigation. Using  $F_{\text{fluid}}^{(0)}$  we find a gas-liquid binodal for screening up to the critical value  $K_{\text{cr}} = 5.3$ . Below that value we observe that, while increasing the screening, the binodal first shifts to higher reduced temperatures and at  $K \approx 2.7$  starts to go downwards again. The critical reduced temperature  $T_{\text{cr}}^*$  accordingly goes from 0.19 at  $K = 1$  to 0.23 and back to 0.20 and the critical packing fraction  $\eta_{\text{cr}}$  rises monotonically with  $K$ , to a maximum of 0.3 at the critical screening length. At the same time, the gas-liquid coexistence becomes more and more metastable with respect to gas-solid (CsCl) coexistence (see also figure 4.9(a), in which the gas-liquid-solid triple point can be seen moving towards higher  $T^*$ ). Finally, at  $K = 5.3$  the triple point temperature reaches the critical temperature, implying that the binodal completely disappears from the  $\eta$ - $T^*$  phase diagram due to becoming metastable w.r.t. the gas-CsCl coexistence.

Because of the non-monotonic behavior of  $T_{\text{cr}}^*[K]$ , plotting an  $\eta$ - $K$  diagram for fixed reduced temperature (for example at  $T^* = 0.21$ ) would show a fluid phase for  $K \approx 1$ , a gas-liquid transition for  $K \approx 3$  and a reentrant fluid phase for  $K \approx 5$ .

However, from the definition of the reduced temperature (equation 4.50) is it clear that  $T^*$  depends on  $K$ , so this comparison at fixed  $T^*$  is of little practical use. Instead, we define an alternative reduced temperature

$$\tilde{T} \equiv \frac{2a}{Z^2 \lambda_B} \quad (4.64)$$

such that  $\tilde{T}$  does not depend on  $K$ . When using this version, we find monotonically decreasing  $\tilde{T}_{\text{cr}}$  as  $K$  increases, as shown in figure 4.5(b).

We have to keep in mind that these results are not very valuable on their own, since they are based on a very simple approximation for the fluid free energy, but they rather serve to validate our method for eventually finding the stability regions of the crystal phases, which is after all what we are interested in. We will therefore compare our results to in particular those of Fortini *et al.* [40] and Leote de Carvalho *et al.* [41].

By performing Monte Carlo simulations for the screened Coulomb restricted primitive model of equally sized, oppositely charged hard spheres, Fortini *et al.* find a stable gas-liquid binodal in the same region as our simple fluid model does, although there are some quantitative

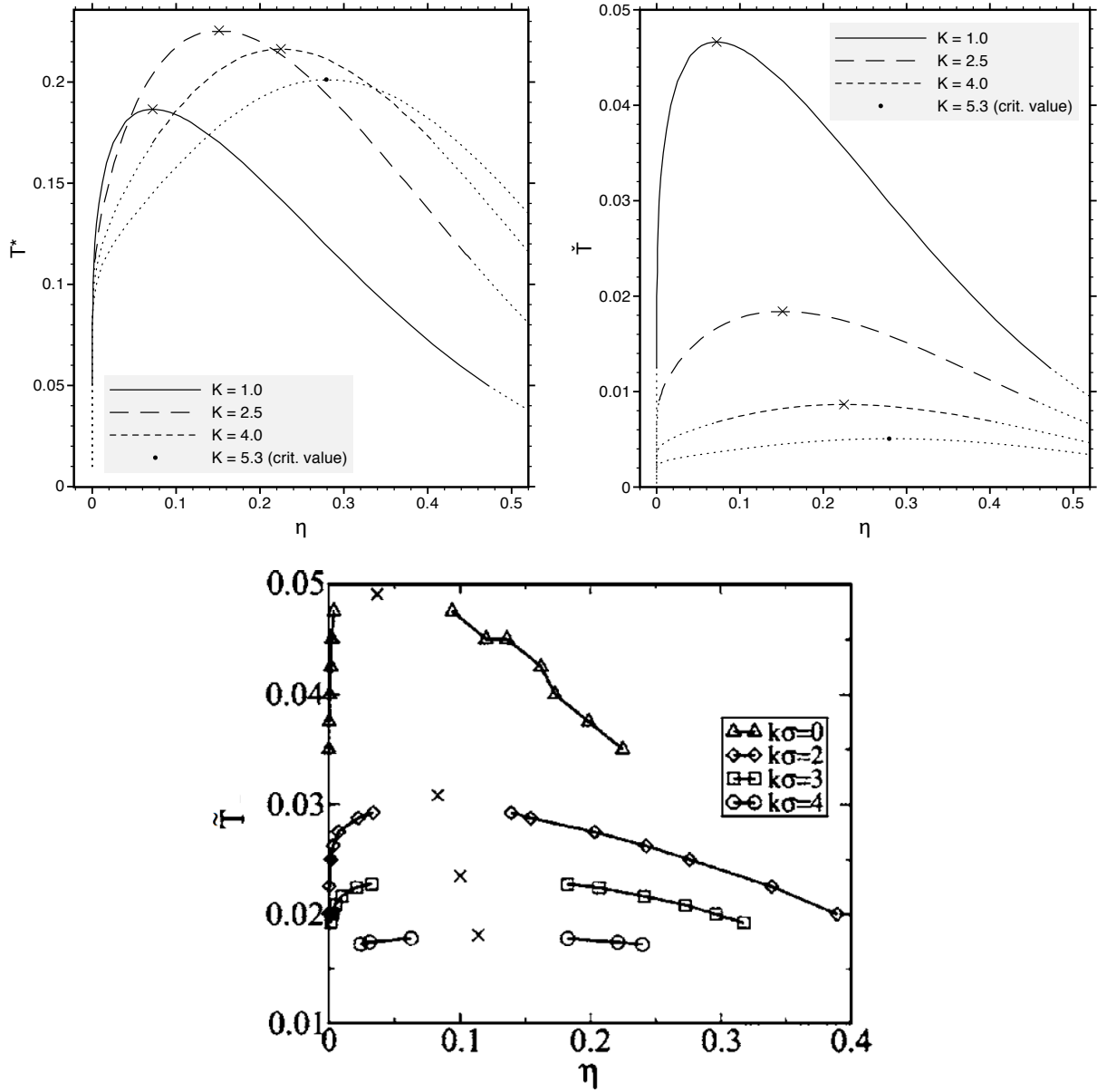


Figure 4.5: (a) and (b) Gas-liquid binodal based on  $F_{\text{fluid}}^{(0)}$  and  $F_{\text{crystal}}^{\text{CsCl}}$ , for several inverse Debye screening lengths  $K$ . At low temperatures gas-solid(CsCl) coexistence dominates the gas-liquid binodal and this effect gets more prominent with increasing  $K$ , until the binodal disappears completely at  $K \geq 5.3$ . The point where this happens is marked by a big dot and the metastable parts of the binodals are denoted by dotted curves. For clarity, the critical points have been marked with crosses. Both diagrams display the same graphs, but (a) has the reduced temperature  $T^*$  on the  $y$ -axis, whereas (b) uses the  $K$ -independent temperature  $\tilde{T}$ . (c) Gas-liquid binodal as calculated by Fortini *et al* [40] through MC simulations, also displayed in the  $\eta - \tilde{T}$  representation.

differences. For more details, see figure 4.5(c). Note that, in the  $K$ -independent  $\eta - \tilde{T}$  representation, the critical temperatures and packing fractions both decrease with increasing screening length, i.e. decreasing  $K$ , again agreeing with our results. Their calculations predict that this binodal becomes metastable with respect to a fluid-solid transition at  $K \gtrsim 4$ , which is remarkably close to our critical value  $K_{\text{cr}} = 5.3$ . In this respect the binary fluid seems to resemble the one-component hard-core Yukawa fluid, for which previous simulation studies predicted a stable gas-liquid transition at  $K = 3.9$  and a metastable one at  $K = 7$  [42], [35].

Additional information comes from references [15] and [13], whose experimental system did not display a gas-liquid phase separation for  $K \approx 7$ , again agreeing with the above.

Furthermore, a theoretical treatment of the system using the one-pole generalized mean-spherical approximation gives critical temperatures and densities that are very close to the just mentioned MC simulation results [41].

After this brief comparison we believe it is safe to say that  $F_{\text{fluid}}^{(0)}$  gives reasonable, though not perfect, results in the low temperature regime, certainly given the simplicity of its expression. Therefore we will indeed use it as for further calculations that will enable us to determine coexistence with ICC's.

### 4.3.3 NaCl-CsCl boundary in $K - Q$ diagram

In this subsection we study the influence of entropy on the phase boundaries of NaCl and CsCl. The reason for choosing specifically these two is that these are the most important structures of stoichiometry 1:1. Both play a prominent role in the low  $Q$ , higher  $K$  region of the ground state phase diagram 3.5(a) and furthermore they have been observed in experiments, as mentioned before.

Our investigation of the NaCl-CsCl boundary at nonzero temperatures is somewhat different than the rest of this chapter, because we temporarily drop the  $Q = 1$  restriction for the system in order to be able to draw a  $K$ - $Q$  phase diagram that could be compared to the results of chapter 3. And secondly, we still treat the colloidal suspension, with which the crystal is in coexistence, as an infinitely dilute gas instead of a fluid.

The main results are shown in figure 4.6. We find that the melting line of NaCl shifts towards the higher  $K$  direction upon increasing the reduced temperature, in other words generating a larger instability region. We conclude that entropy causes NaCl to become less stable, which was to be expected because a higher temperature will cause larger instability in virtually all physical and chemical systems. At higher temperatures the structures disappear completely from our phase diagram, first NaCl around  $T^* \approx 0.34$  and subsequently CsCl at  $T^* \approx 0.4$ . For these temperatures, the packing fraction drops below the Lindemann packing fraction  $\eta_L$  due to thermal motions of the particles, making the crystal unstable by our definition.

Comparing these theoretical results with Monte Carlo simulations (figure 4.7) from reference [17] shows that the latter exhibits a shift of the NaCl melting line in the same direction as temperature increases, but only somewhat quicker. We conclude that the Lindemann

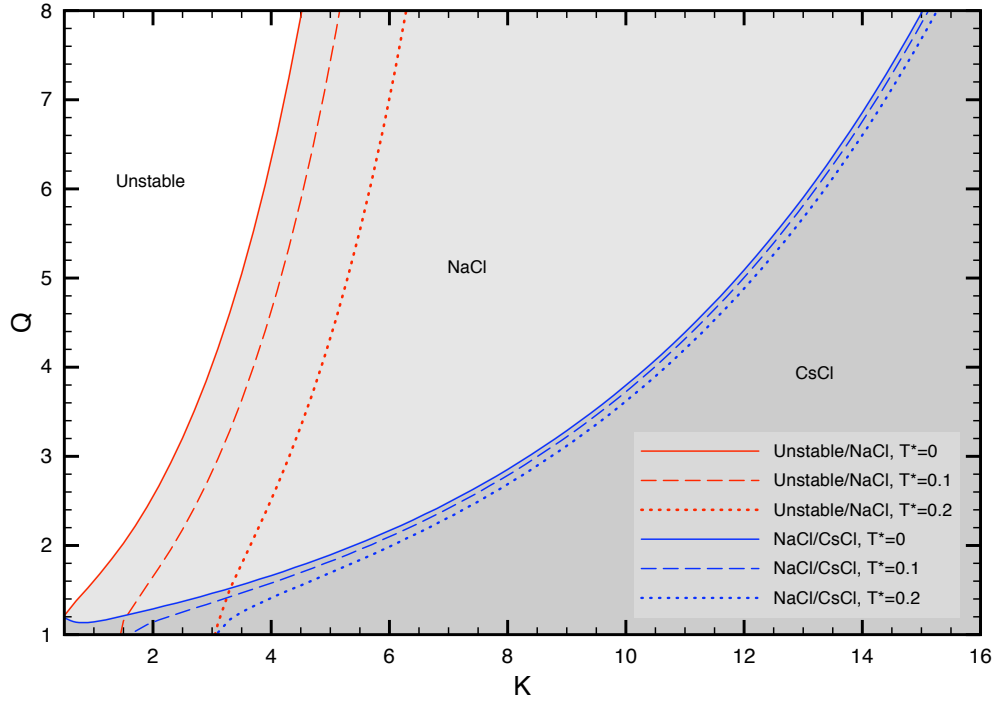


Figure 4.6: Finite temperature NaCl-CsCl phase diagram in the  $K$ - $Q$  representation, for variable reduced temperatures  $T^*$ . The NaCl-CsCl boundary line is determined from  $F_{\text{crystal}}$  and shows which phase is coexisting with a dilute gas phase, whereas the NaCl melting line is calculated using the Lindemann criterion. For the  $T^* = 0$  case, the boundary line has already been calculated in chapter 3 (see figure 3.5(a)) and the NaCl melting line is actually obtained by taking the  $T^* \downarrow 0$  limit, because the Lindemann criterion cannot be applied for dense-packed crystals at zero temperature. In the low  $K$  region other stable structures can be found, but these are not displayed here.

criterion indeed presents a good way to determine when ICC's become unstable, although a slightly lower constant (instead of 0.1) in equation (4.52) would actually give improved results. It is not so strange to expect this constant to be a little different in reality, since the Lindemann criterion is a heuristic measure generally applied to regular atomic crystals.

At the same time, while the NaCl stability region is reduced because of melting at relatively low  $K$ , it is expanded towards the CsCl direction, albeit not very much. Still, this shows that entropy seems to favor the NaCl over the CsCl lattice.

Again, the simulation results show a shift in the same direction, but this time there is a much larger temperature dependence of the NaCl-CsCl boundary. A possible explanation for this difference would be that the volume we associate with entropy does not take into account the precise shape of the Wigner Seitz cell, such that the NaCl and CsCl structures are not very different in this model, except for their packing fractions. The simple conclusion would then be that NaCl benefits more from a temperature increase because of its less dense

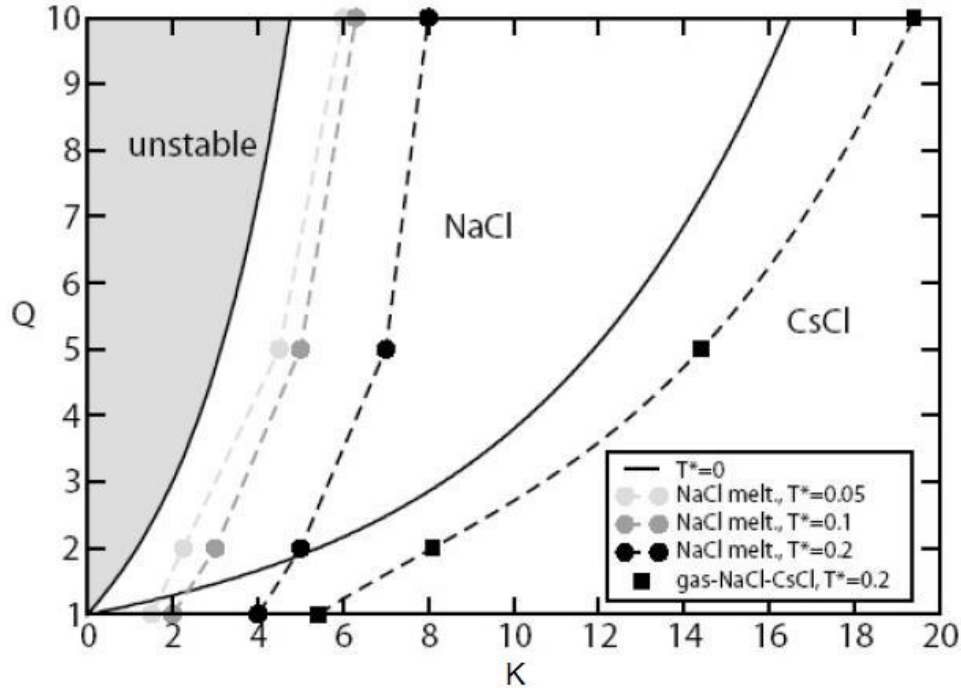


Figure 4.7: NaCl-CsCl phase diagram generated by Monte Carlo simulations, provided by Hynninen *et al.* [17]. The ground state NaCl-CsCl boundary line ( $T^* = 0$ ) is the same as in figure 4.6, because it was determined using similar Madelung energy calculations.

structure, but we have to admit that the theory might not be considered accurate enough to draw solid conclusions for this situation.

A remarkable point is that everywhere on the NaCl-CsCl boundary line, the factor  $\eta/\eta_{\max}$  turns out to be the same for both structures, which leads us to believe that packing is the main quantity responsible for the relative stability of lattices.

Whereas in chapter 3 almost all stable structures were dense-packed, we now find that the packing fraction of a crystal (whether it is coexisting with a fluid or a dilute gas) decreases drastically when screening is reduced, as is shown in figure 4.8. So we conclude that entropy indeed causes crystals to become less dense and in this respect also less stable, but particularly for long ranged interactions. Besides the screening-packing relation, we know from the previous chapter that a larger charge discrepancy, i.e. further away from charge neutrality, causes less dense structures as well.

We have to remark that the zero-density gas approximation favors coexistence with structures at lower packing fractions. At higher temperatures ( $T^* \gtrsim 0.2$ ), the  $\rho \log[\rho] - \rho$  terms in the *realistic* expression for the free energy per volume of the gas will cause coexistence with a *nonzero* density gas phase, such that the common tangent line in a  $F/V$  vs.  $\rho$  diagram lies lower and is therefore more likely to be connected to the higher density phase, in this case CsCl. This is why we expect the NaCl-CsCl boundary line to shift towards the NaCl side,

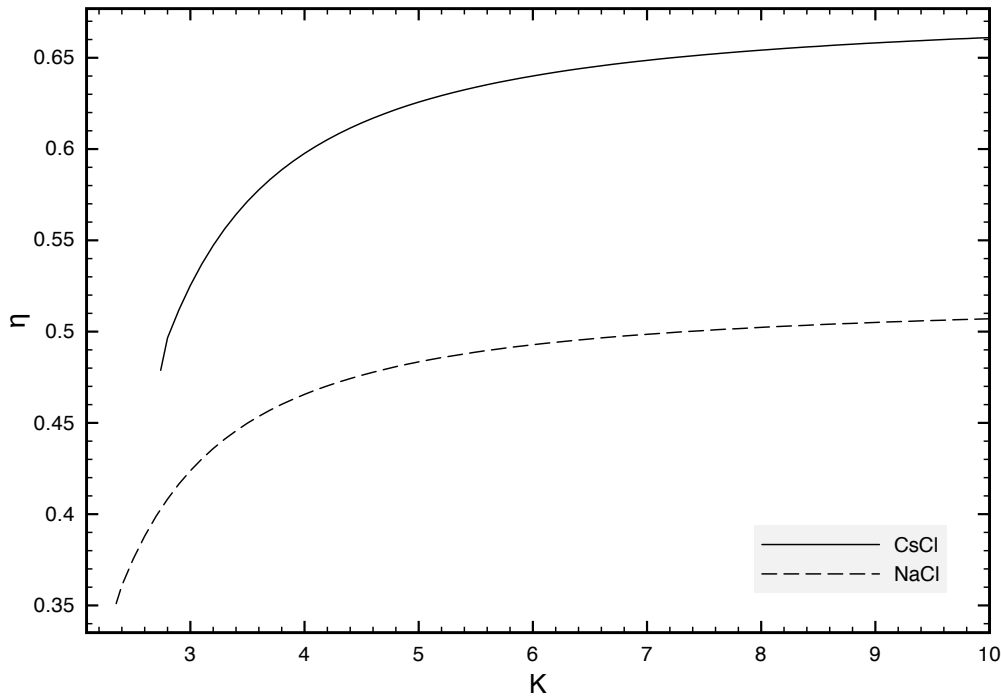


Figure 4.8: Crystal packing fraction  $\eta$  as function of screening parameter  $K$ , determined using common tangent construction at fixed  $T^* = 0.1$  and  $Q = 1$ . For these circumstances both crystal phases are coexisting with a dilute gas phase. Note that the packing fraction decreases so much at low screening that the crystals fall apart due to Lindemann instability (unstable points have not been plotted here).

when also taking this nonzero-density gas into account at higher temperatures. The latter effect will counteract the shift that we found in figure 4.6.

#### 4.3.4 Phase diagrams in $\eta$ - $T^*$ plane

We now arrive at the most important results of this chapter, which are summarized by the phase diagrams of figure 4.9. These diagrams display which phases and structures coexist for a given (reduced) temperature and screening parameter. Together, they describe a large part of the complete phase diagram for the symmetric case.

One of the distinguishing features of the  $K = 3$  diagram is the fact that, below critical temperature  $T_{\text{cr}}^* = 0.225$ , the fluid phase separates to form a gas-liquid binodal, which becomes metastable with respect to the gas-solid (CsCl) transition at even lower temperatures (see subsection 4.3.2). At high packing fractions we find the Tetragonal structure.

In addition to the fluid, CsCl and Tetragonal phases, the  $K = 6$  screening case gives rise to a stable phase called  $\text{CuAu}^{(\gamma)}$ , a modified version of the CsCl structure that has a variable lattice parameter  $\gamma$  (see subsection 4.3.5). The gas-liquid binodal is now completely

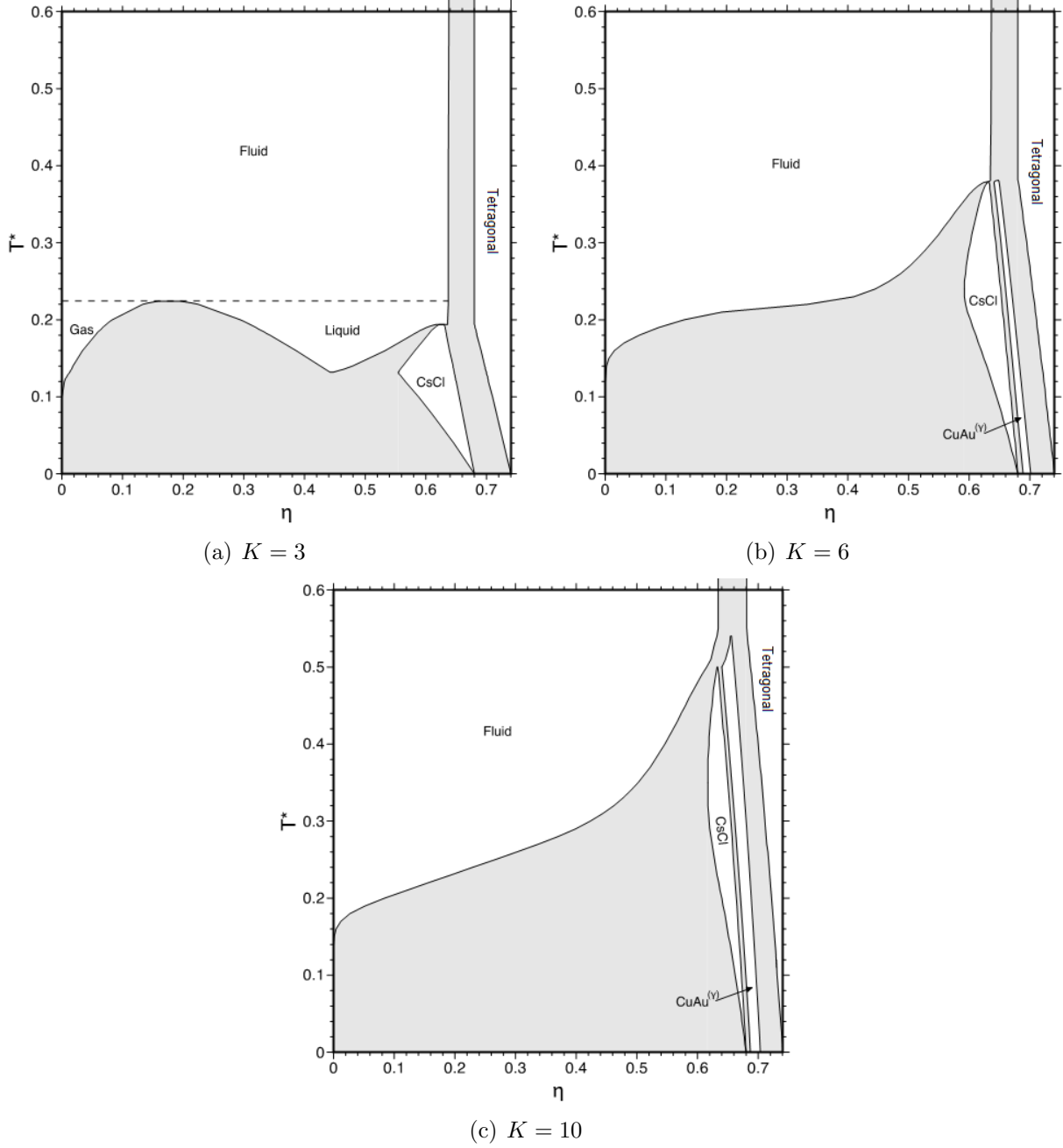


Figure 4.9: Phase diagrams based on Helmholtz free energies  $F_{\text{fluid}}^{(0)}$  and  $F_{\text{crystal}}$ , in the  $\eta$ - $T^*$  representation. Calculations were done for the symmetric case at fixed screening  $K$ . The shaded areas mark the regions where two phases, connected by horizontal tie lines, coexist.



metastable with respect to the fluid-solid (CsCl) transition and has therefore disappeared.

Compared to the previous diagrams, the CsCl and  $CuAu^{(\gamma)}$  stability regions in the  $K = 10$  diagram have been extended to higher  $T^*$  and the latter has become much broader as well, now consisting of structures with a larger continuous range of lattice parameters  $\gamma$ .

We notice that in all three diagrams the zero temperature limit yields a gas-solid coexistence between an infinitely dilute gas phase and a dense-packed CsCl crystal phase. This is exactly what would be expected from the results of the ground state Madelung calculations: diagrams 3.5(a) and (b) indeed show a stable CsCl structure everywhere on the line  $Q = 1$  for  $K > 0.5$ . Furthermore these results confirm the method that we used in the previous chapter, of choosing an infinitely dilute gas phase with which the crystal is in coexistence at zero temperature.

At the other end of the temperature scale, in the high temperature limit ( $T^* \gg 1$ ), electrostatics becomes irrelevant because of the dominant contribution of entropy, reducing the system to the single-component hard-sphere case. This is immediately clear from the fact that all phase diagrams 4.9 converge very quickly to the same packing fractions in this regime, irrespective of their screening range. We find higher packing fractions  $\eta_{\text{fluid}} = 0.638$  and  $\eta_{\text{solid}} = 0.680$  than expected, which is a shortcoming of our crystal model. In subsection 4.3.6 we investigate this a little further, by modifying  $F_{\text{crystal}}$  such that individual particles have a larger volume to move in, which causes some shifts in the phase diagrams.

We also observe that the crystal stability regions (in particular CsCl) become broader as screening decreases. This has already been recognized from figure 4.8 and is now getting clear. Based on that same diagram we expect NaCl to become stable at even lower screening values ( $2.4 < K < 2.8$ ), but this specific parameter range has not been looked at in detail.

Comparing our phase diagram for  $K = 6$  to results from Monte Carlo simulations (figure 4.10) we notice a number of qualitative agreements: the CsCl, CuAu and Tetragonal structures are all found to be stable by both methods. Indeed, no gas-liquid transition is observed for the fluid at this screening parameter and furthermore, the boundary between CsCl and CuAu does also seem to exhibit a first order phase transition, but that will be looked into in the next subsection. A (preliminary) study of the disordered phase did not show this to be stable, however.

Quantitatively there seem to be some rather big discrepancies for the crystal phase. First, simulation results show CsCl and CuAu to be stable up until  $T^* \approx 1$ , whereas our theory predicts this to be only true for  $T^* \lesssim 0.4$ . And second, fluid-solid coexistence takes place at higher packing fractions in our model, which we already mentioned. We suspect both differences to be caused by underestimating the volume  $v^*$  in 4.21 that determines the entropic contribution to the Helmholtz free energy of the crystal phase. This is something that will be investigated as well (see subsection 4.3.6). Note that the temperature at which the fluid goes from dilute to dense (around  $T^* \approx 0.2$ ) is practically the same for our model and the simulation results, indicating that our theory predicts the critical temperature reasonably well.

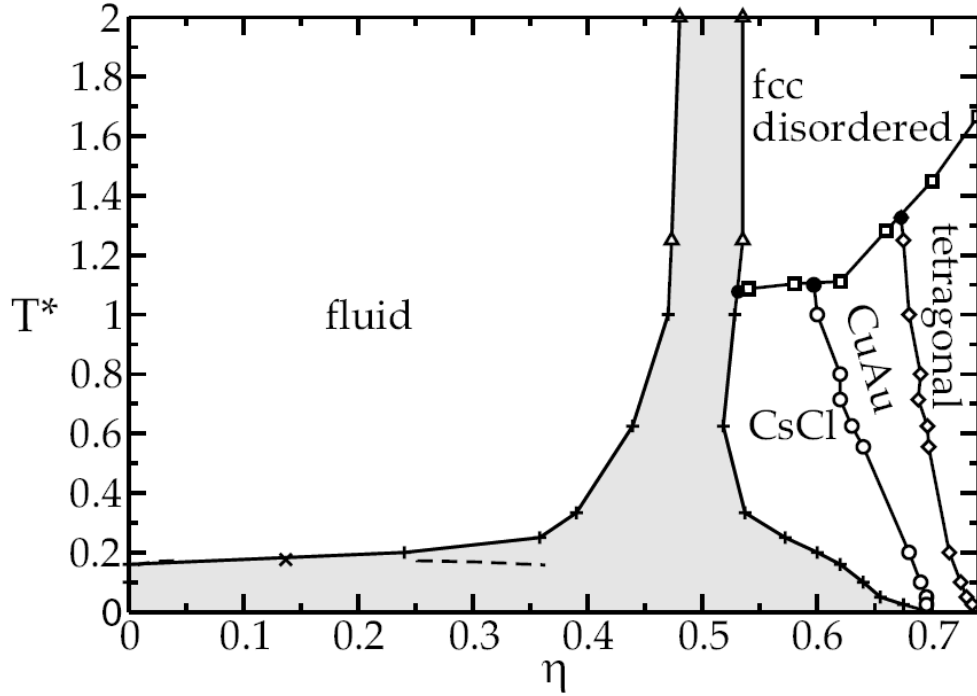


Figure 4.10:  $\eta - T^*$  phase diagram similar to figure 4.9(b), but determined using Monte Carlo simulations. Image borrowed from A.-P. Hynninen [17].

#### 4.3.5 CsCl-CuAu phase transition

In phase diagrams 4.9(b) and (c) one notices the phase  $CuAu^\gamma$ , that turns out to be stable at slightly higher packing fractions than CsCl. This new phase is in fact an intermediate structure between CsCl and CuAu. As is shown in figure 4.11, the CuAu lattice possesses an fcc lattice and can be formed out of the cubic CsCl lattice by distorting it with a factor  $\sqrt{2}$  in the (100) direction. We do not find the CuAu structure to be stable for the investigated circumstances, but the continuous distortion between CsCl and CuAu allows us to consider the intermediate structures as well, which we call  $CuAu^\gamma$ . For this purpose we introduce a parameter  $\gamma$  that shifts linearly between 1 and  $\sqrt{2}$ , such that  $CuAu^{(1)}$  corresponds to CsCl and  $CuAu^{(\sqrt{2})}$  to CuAu. Of course, this parameter is just the height/width ratio of a distorted CsCl unit cell.

The free energy curves for a number of these structures (only the relevant ones) have been plotted in figure 4.12 and using a Common Tangent construction we find that, for  $K = 6$  at  $T^* = 0.2$ , only the intermediate structures with  $1.16 < \gamma < 1.22$  are stable.

We get a much clearer picture of this CsCl- $CuAu^{(\gamma)}$ -CuAu transition when we plot the order parameter  $\gamma$  versus the packing fraction  $\eta$ , as is done in figure 4.13. In this diagram we distinguish a lower (CsCl) and an upper branch ( $CuAu^{(\gamma)}$ ), separated by a discontinuity in both  $\gamma$  and  $\eta$ , thus showing a first order phase transition between these two crystal

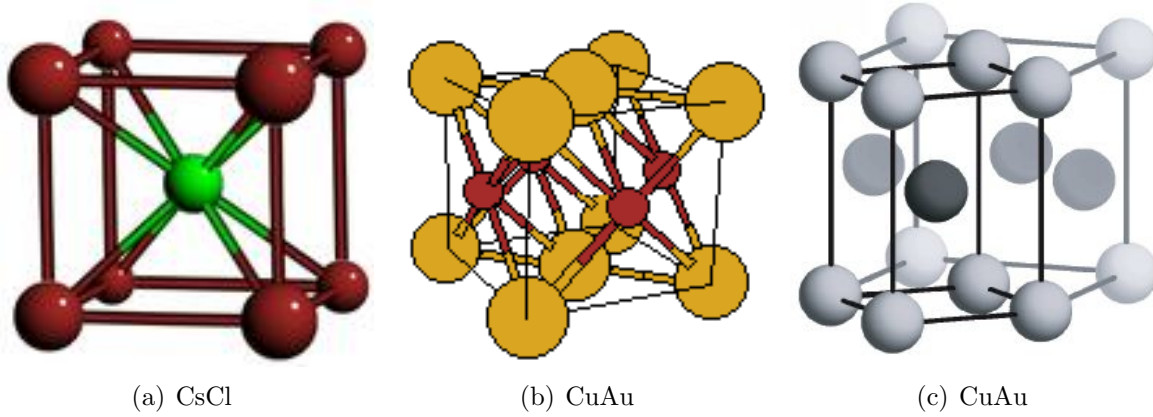


Figure 4.11: Standard unit cell of CsCl and two equivalent representations of the CuAu lattice. Comparing (a) and (c), it is obvious that CuAu has the same structure as CsCl, but is elongated by a factor  $\sqrt{2}$  in the (100) direction. (Pictures (a) and (b) taken from the Crystal Lattice Structures Web page, <http://cst-www.nrl.navy.mil/lattice/>, provided by the Center for Computational Materials Science of the United States Naval Research Laboratory, and (c) from reference [17], provided by A.-P. Hynninen.)

structures.

For  $K = 10$  and at the same reduced temperature ( $T^* = 0.2$ ) we find a much broader stability region for the intermediate structures, ranging from  $\text{CuAu}^{(1.13)}$  to  $\text{CuAu}^{(1.36)}$  (not shown in diagram 4.13). This seems to suggest that  $\text{CuAu}^{(\gamma)}$  gets more stable with respect to Tetragonal at higher screening  $K$ .

### 4.3.6 Variable cell volume

To investigate the influence of the integration volume in equation (4.18) on the crystal's Helmholtz free energy, we replace it with the more generic volume

$$v_\alpha^R \equiv \alpha v^{\text{RWS}} = \alpha \frac{\tilde{v}}{\eta} \left( 1 - \left( \frac{\eta}{\eta_{\text{max}}} \right)^{1/3} \right)^3 \quad \text{with} \quad 1 \leq \alpha \leq \frac{4\pi}{3}, \quad (4.65)$$

which can be varied via parameter  $\alpha$ . The Wigner Seitz case is given by  $\alpha = 1$ , but this clearly underestimates entropy, since it does not allow particles to move outside their own Wigner Seitz cell whatsoever. The upper limit corresponds to a spherical volume with radius  $L$ , where  $L = (V/N)^{1/3}$  is the average lattice spacing. In reality,  $\alpha$  should be chosen somewhere in the middle of the range  $1 \leq \alpha \leq \frac{4\pi}{3}$ .

Multiplying the volume by factor  $\alpha$  gives the crystal more entropy and will lower  $\beta F_{\text{crystal}}/N$  by an amount  $\log[\alpha]$  and possibly more, depending on the curvature of the local potential energy (see equation (4.15)).

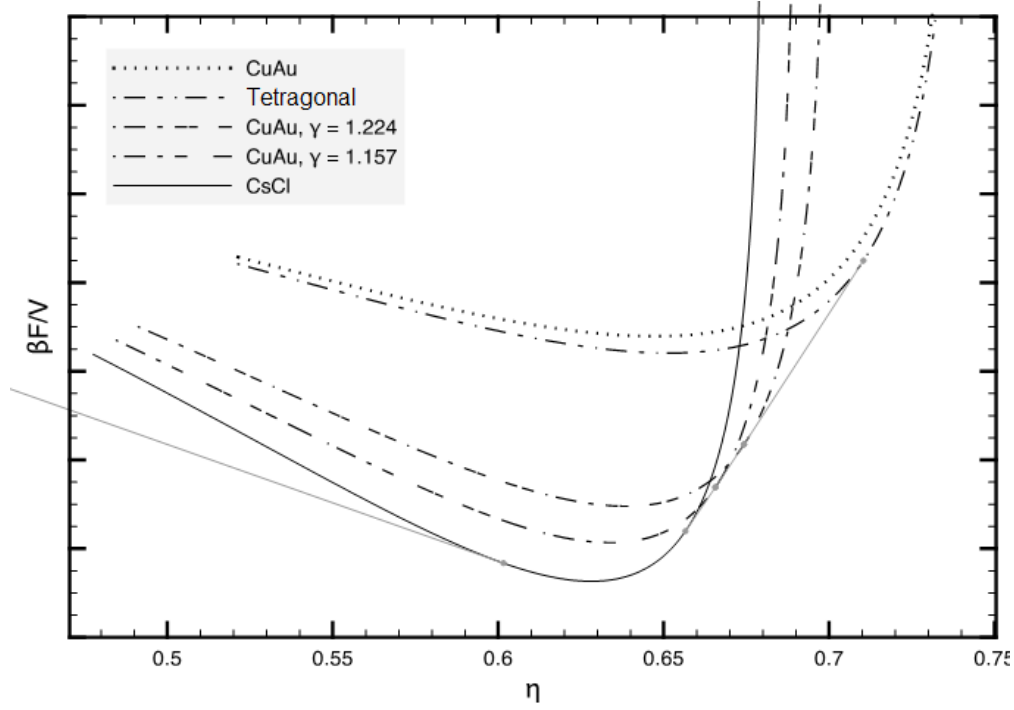


Figure 4.12: Helmholtz free energies of several crystal structures, connected by Common Tangent lines, as calculated for  $T^* = 0.2$  and  $K = 6$ . We observe fluid-solid coexistence with the CsCl phase and two solid-solid transitions, namely CsCl-CuAu<sup>(1.16)</sup> and CuAu<sup>(1.22)</sup>-Tetragonal. For clarity, the continuous transition between CuAu<sup>(1.16)</sup> and CuAu<sup>(1.22)</sup> is not shown here, only the free energy curves of these two structures themselves. In fact, it would yield a slightly concave piece in the free energy curve of CuAu<sup>( $\gamma$ )</sup> for  $0.665 < \eta < 0.675$ . The structures CuAu<sup>( $\gamma$ )</sup> with  $1.22 < \gamma < \sqrt{2} \approx 1.41$  (only CuAu<sup>( $\sqrt{2}$ )</sup> depicted) all have curves above the CuAu<sup>(1.22)</sup>-Tetragonal Common Tangent line and are therefore metastable.

The results for choosing  $\alpha = 4\pi/3$  are shown in figure 4.14. We find a fairly big influence on the fluid-solid coexistence regions: the CsCl stability region is enlarged quite a lot and lower packing fractions are observed in the high temperature limit, thus agreeing more with the simulation results of figure 4.10.

Solid-solid transitions are hardly affected by  $\alpha$  and the gas-liquid is not changed at all (since we only change the crystal free energy expression), but disappears more easily, i.e. the critical  $K$  is lower.

Although this method is too simple to give definite answers about the real phase diagram, it does seem to suggest that the expression for  $F_{\text{crystal}}$  structurally underestimates entropy. Preliminary results obtained using an alternative integration volume also point in that direction.

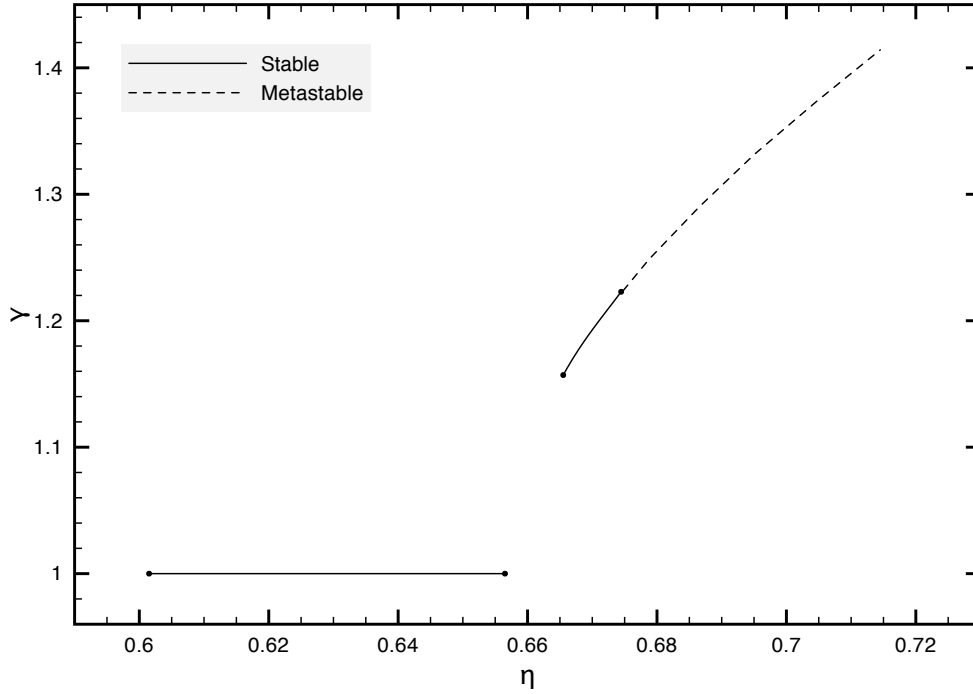


Figure 4.13: Order parameter  $\gamma$  for the CsCl-CuAu phase transition as a function of packing fraction  $\eta$ , at  $T^* = 0.2$  and  $K = 6$ . The lower branch at  $\gamma = 1$  represents the stable CsCl structure and the upper branch corresponds to the intermediate structures between CsCl and CuAu. A large part of the upper branch is metastable with respect to the Tetragonal structure (see also figures 4.9(b) and 4.12). We observe that only between  $\gamma = 1.16$  and  $\gamma = 1.22$  there is a continuum of stable structures. The gap around  $\eta = 0.66$  stems from phase coexistence between the two branches.

## 4.4 Conclusions

In this most important chapter we investigated the phase behavior at nonzero temperature and pressure, but with the restriction that both colloidal species are of the same size and opposite charge. We did this using Helmholtz free energy calculations in the canonical ensemble, for both the crystal and fluid phases. Subsequently, coexistence between these phases was calculated via Common Tangent constructions and the Lindemann criterion was applied as a measure for distinguishing stable and unstable crystals.

Our research comprised investigating several crystal and fluid models and comparing them, in order to choose the best method to determine ICC phase behavior. The fluid models were all based on the Carnahan-Starling expression for hard spheres plus different expressions for the electrostatic interactions. On the other hand, the crystal models were built upon the Madelung energy of chapter 3, plus an additional term for the effective cell volume around colloids, thus taking entropy into account. For this volume term we looked at two alternative models as well.

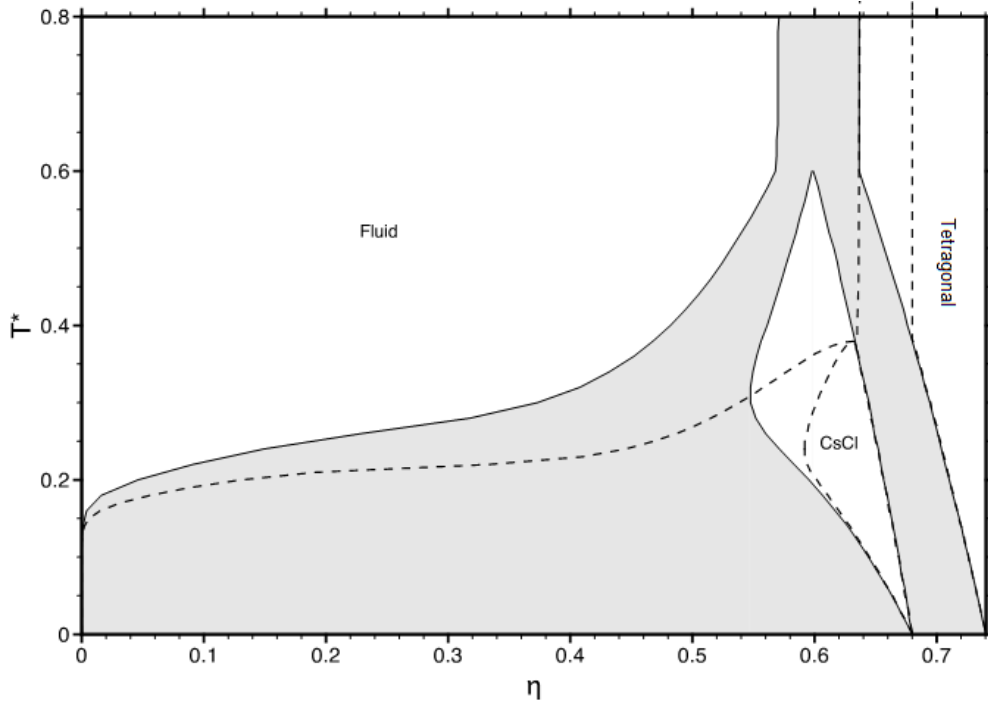


Figure 4.14: Fluid-CsCl-Tetragonal phase diagram for  $K = 6$ , similar to figure 4.9, but now for higher volume parameter  $\alpha = 4\pi/3$ . The dashed lines represent the situation  $\alpha = 1$  (as shown in 4.9(b)). Although stable, the intermediate structure  $\text{CuAu}^{(\gamma)}$  is not shown here. Fluid-solid coexistence in the high temperature limit takes place at packing fractions  $\eta_{\text{Fluid}} \approx 0.57$  and  $\eta_{\text{Tetragonal}} \approx 0.64$ .

Studying the mobility of single colloids on a crystal lattice, we found that the lattice sites in most ICC's are actually maxima in the potential energy, in contrast to the standard example of an Einstein crystal. We also found that the curvature of this potential energy 'hill' is approximately proportional to the Madelung energy itself, and, additionally, that the phase diagram results do not change very much when the curvature is not taken into account, in calculations that were done using the previously mentioned alternative versions of the effective volume term. This allowed us to conclude that our simplest model ( $F_{\text{crystal}}^{(0)}$ ) for the crystal free energy was sufficiently accurate.

As an important side step, we examined our simple model  $F_{\text{fluid}}^{(0)}$  and found gas-liquid coexistence, as was also predicted by other MC simulation research and theory (Fortini, Leote de Carvalho), which gave us more confidence on the validity of our model. Since our results were qualitatively similar and were laying in same regime as well, we considered  $F_{\text{fluid}}^{(0)}$  to be fairly realistic, especially for low reduced temperature  $T^*$ . Benefiting from its relatively simple expression, we continued to use this model for further research.

After this, we turned our attention to some of the actual phase diagrams that this research project was supposed to obtain. For the the NaCl-CsCl boundary that had already been

determined for the ground state, we conclude that an increased temperature tends to favor NaCl over CsCl. This has also been predicted by MC simulations, but our research found the shift to be much smaller. We have to note that these calculations were still done for asymmetric charges and coexistence with a dilute gas phase instead of a fluid, contrary to the rest of this chapter.

As a general feature of the system, we also observe that lower screening, i.e. longer interaction range, causes the crystal to become less dense and therefore less stable. We conclude that entropy becomes more important compared to electrostatics for a system dominated by long range interactions.

Determining phase diagrams in the  $\eta - T^*$  representation was one of our major goals and these turned out to be qualitatively similar to previous MC simulation research, both of which find stability regions for CsCl, CuAu and Tetragonal crystals. As a nice detail in our phase diagrams, we also found a first order phase transition between the structures CsCl and CuAu. However, quantitatively there was a large discrepancy between our results and the ones generated through simulations, the main difference being that we find these stability regions at lower temperature.

We suspected that this discrepancy could be due to our specific choice for the effective volume around each colloid, in the crystal model that we have been using. We have been able to confirm that this volume indeed has considerable influence on fluid-solid coexistence region. Further results suggest that our models underestimate the contribution of entropy to the Helmholtz free energy.





## Summary and outlook

### 5.1 Summary

In the introductory chapter we briefly talked about colloid science, explained what Ionic Colloidal Crystals are, gave a short overview of other research relevant to this topic and outlined the scope of this thesis.

Then we described the system in more detail, elaborated on which effects would be playing a role and which not and, more importantly, looked at the expression for the interaction between two colloids (DLVO theory), which can be regarded as one of the cornerstones for this area of research. Furthermore, we briefly discussed the validity and precision of this interaction potential.

Next, we looked at the simplified situation in which the system has zero temperature and pressure (the ground state) and used numerical Madelung energy calculations to determine the phase behavior of an Ionic Colloidal Crystal. This was done for different size ratios, charge ratios, screening lengths and applied to various crystal structures of different stoichiometries, such that a large part of the  $T = 0$ ,  $p = 0$  intersection of parameter space is covered by these results. We discovered a large variety of crystal structures, among which several ones that were not known to be stable until now. We also discussed these results and gave a few simple rules of thumb that explain the general phase behavior in terms of the main system parameters. Comparing our results to other theoretical and experimental research, we found reasonable agreements, as far as the data allowed us to make a fair comparison.

In the following and most important chapter, we extended the theory to the nonzero temperature regime by including entropic contributions as well. Although we made the restriction of (mostly) looking at a symmetric system, with equal sizes and (absolute) charges, we now considered the general case of a colloidal crystal being in coexistence with a colloidal fluid with finite pressure and density. Looking at the system from the canonical ensemble viewpoint, we first derived different approximations for the Helmholtz free energy of both fluid

and crystal. From two sub-investigations we were able to choose the appropriate approximations for fluid and crystal, and these models were used for the research in the rest of the chapter. In order to determine coexistence between phases we used the Common Tangent method and furthermore we applied the Lindemann criterion to establish whether a crystal is considered stable or not. After calculating the (equal size, unequal charge) phase diagram for the abundant crystal structures NaCl and CsCl, we found that entropy tends to favor NaCl. Furthermore, we determined the phase behavior of the symmetric system by drawing  $\eta - T^*$  intersections for several screening lengths, thereby covering a large part of parameter space. A comparison to Monte Carlo simulation results shows qualitatively similar results, but our stability regions seem to occur at lower temperatures. This quantitative discrepancy is very likely caused by underestimating the contribution of entropy in our crystal model. Further research may give a definite answer to this.

While our free energy calculation method is a quick and also powerful tool, it works best in combination with other methods such as MC simulations or more advanced methods based on genetic algorithms. The latter two have the advantage that they make it possible to discover new non-existing structures, whereas our method always requires a certain structure as input and can subsequently calculate if it is stable or not.

## 5.2 Future research

The first that springs to mind when thinking about future research is the fact that our models might be improved in order to obtain more exact results. From chapter 4 it is clear that we already spent quite a lot of effort on improving the models for the crystal and fluid Helmholtz free energies, but these remain coarse approximations of reality. Two of the most likely paths towards a better theory are:

- Solving the  $g[r]$  problem (that generates unphysically high densities at short distances) for the fluid phase at low temperatures in a more elegant way than we have attempted, for example by elaborating on our 'Better Ansatz' method which also has a more analytic approach.
- Constructing a more exact function for the cell volume in which individual colloids are allowed to move when they are located on a crystal lattice. A preliminary exploration of this option was indeed pointing towards more realistic phase behavior (not presented in this thesis).

Moreover, it is always possible to give a more complete picture of this research, for example by examining an even larger variety of crystal structures than we did in chapter 3. We think that this would not yield major new findings though.

On the other hand, detailed research on the asymmetric case at finite temperature could certainly bring interesting new results. Because of time constraints we investigated only a minor part of this system (not presented either).

A generalization of the colloidal crystal concept, such as the extension from binary crystals to crystals consisting of multiple different species of colloids, is also possible. After all, ionic analogues like  $\text{CaTiO}_3$  and  $\text{Fe}_3\text{W}_3\text{C}$ , though complicated, do exist in nature. Given the fact that colloidal charges and size can be tuned in a continuous way this would undoubtedly lead to a enormous variety of structures. The question remains if this extra variety is meaningful enough to start new research on.

Another fairly easy modification of our algorithm would be to consider the 2-dimensional version of ICC's, which can give further information about the structure of thin binary layers, that could act again as the starting point for the growth of 3D structures, for instance.

Additionally, applying external fields to ICC's would of course bring us to a whole new topic of research, that could provide even more interesting results.

## 5.3 Potential applications

Not only can we look at ICC's as a nice model system, it can also be of great importance to new practical applications and other fields of research. One of the major goals of related research projects is to produce efficient photonic crystals, with all kinds of special optical properties [6]. Creating crystals with a full photonic bandgap could lead to new electro-optical components such as efficient LEDs, microscopic lasers and waveguides, mirrors, optical information storage devices, narrow bandwidth filters, optical sensors, optical switches, etc [43, 44].

Other applications lie for example in the biomedical area, where ICC's can serve as drug releasing agents, 3D micro-environments for cell cultures [45] or as substrates for neuronal networks [46].

The high tunability of their 3D structure might also be interesting for industrial products like porous materials and membranes that can be used for filtering purposes [43, 44].

Finally, colloidal crystals can be seen as templates for new materials. Advanced coating with thin metallic films that can guide surface plasmons or with catalytic chemicals which give it photo-catalytic properties belong to the options [43]. And filling the space in between colloids with specific polymers can give rise to applications such as chemical sensors or pressure sensors, the latter of which exploits the special rheological properties of this combination [44].

Of course, in many of these cases ordinary colloidal crystals composed of one single species will be sufficient, but exploiting the fact that ICC's have a larger parameter space will also lead to a larger variety in structures. Extra properties such as easier disassembly of the crystal using an electric field or regulation by salt concentration are definitely benefits.



# Appendix **A**

## Notations and symbols

### A.1 Notations

- Vectors are printed boldface.
- We always write an argument of a function between squared brackets. For example:  $f[x]$ . This is to distinguish it from ordinary round brackets, that we only use for grouping together mathematical expressions.
- We write  $\mathbf{r}_{ij} \equiv \mathbf{r}_i - \mathbf{r}_j$  and  $r \equiv |\mathbf{r}|$  for shorter notations.
- We define the set of all particles and its subsets as

$$\mathcal{N} \equiv \{1, 2, \dots, N\} \quad (\text{A.1})$$

$$\mathcal{A} \equiv \{i \in \mathcal{N} | \text{particle } i \text{ is of species A}\} \quad (\text{A.2})$$

$$\mathcal{B} \equiv \{i \in \mathcal{N} | \text{particle } i \text{ is of species B}\}. \quad (\text{A.3})$$

The corresponding sets describing their positions are respectively

$$\{\mathbf{r}\}_{\mathcal{N}} \equiv \{\mathbf{r}_1, \mathbf{r}_2, \dots, \mathbf{r}_N\} \quad (\text{A.4})$$

$$\{\mathbf{r}\}_{\mathcal{A}} \equiv \{\mathbf{r}_i | i \in \mathcal{A}\} \quad (\text{A.5})$$

$$\{\mathbf{r}\}_{\mathcal{B}} \equiv \{\mathbf{r}_i | i \in \mathcal{B}\}. \quad (\text{A.6})$$

- Notations:  $i, j, \dots \in \{1, 2, \dots, N\}$  for particle numbers.  $\sigma, \tau \in \{1, 2, 3\}$  for  $x$ -,  $y$ - and  $z$ -coordinates.

### A.2 Symbols

$$\beta \equiv \frac{1}{k_B T} \quad (\text{A.7})$$

Debye screening length  $\kappa^{-1}$ :

$$\kappa^{-1} \equiv (8\pi\lambda_B c_s)^{-\frac{1}{2}} \quad (\text{A.8})$$

Bjerrum length  $\lambda_B$ :

$$\lambda_B \equiv \frac{e^2}{4\pi\epsilon\epsilon_0 k_B T} \quad (\text{A.9})$$

Thermal wavelength  $\Lambda$ :

$$\Lambda \equiv \frac{\hbar}{\sqrt{2\pi m k_B T}} \quad (\text{A.10})$$

Reduced temperature  $T^*$ :

$$T^* \equiv \frac{(1 + \kappa a_A)(1 + \kappa a_B)(a_A + a_B)}{Z_A Z_B \lambda_B} \quad (\text{A.11})$$

Packing fraction  $\eta$ :

$$\eta \equiv \frac{\sum_{i=1}^N \frac{4\pi}{3} a_i^3}{V} = \frac{4\pi}{3} \frac{N_A a_A^3 + N_B a_B^3}{V} = \frac{4\pi\rho}{3} ((1-x)a_A^3 + x a_B^3) \quad (\text{A.12})$$

where  $i$  sums over all particles.

Density  $\rho$ :

$$\rho \equiv \frac{N}{V} \quad (\text{A.13})$$

Proportionality factor  $\tilde{v}$  between  $\eta$  and  $\rho$  (dimension: volume):

$$\tilde{v} \equiv \frac{\eta}{\rho} = \frac{4\pi}{3} ((1-x)a_A^3 + x a_B^3) \quad (\text{A.14})$$

Dimensionless screening length  $K$ :

$$K \equiv \kappa(a_A + a_B) \quad (\text{A.15})$$

Charge ratio  $Q$ :

$$Q \equiv -\frac{Z_A}{Z_B} \quad (\text{A.16})$$

Size ratio  $q$ :

$$q \equiv -\frac{a_B}{a_A} \quad (\text{A.17})$$

Mixing ratio  $x$ :

$$x \equiv \frac{N_B}{N_A + N_B} \quad (\text{A.18})$$

Mass ratio  $y$ :

$$y \equiv \frac{m_B}{m_A + m_B}. \quad (\text{A.19})$$

One particle density  $\rho_A^{(1)}[\mathbf{r}]$  (and similarly  $\rho_B^{(1)}[\mathbf{r}]$ ):

$$\rho_A^{(1)}[\mathbf{r}] \equiv \left\langle \sum_{i \in A} \delta(\mathbf{r} - \mathbf{r}_i) \right\rangle \quad (\text{A.20})$$

Two particle density correlation function  $\rho_{AA}^{(2)}[\mathbf{r}, \mathbf{r}']$  (and similarly  $\rho_{AB}^{(2)}[\mathbf{r}, \mathbf{r}']$ ,  $\rho_{BB}^{(2)}[\mathbf{r}, \mathbf{r}']$ ):

$$\rho_{AA}^{(2)}[\mathbf{r}, \mathbf{r}'] \equiv \left\langle \sum_{i \in A} \sum_{\substack{j \in A \\ j \neq i}} \delta(\mathbf{r} - \mathbf{r}_i) \delta(\mathbf{r}' - \mathbf{r}_j) \right\rangle \quad (\text{A.21})$$

Correlation functions  $g_{kl}[r]$  are defined as:

$$\rho_{kl}^{(2)}[\mathbf{r}, \mathbf{r}'] = \rho_k \rho_l g_{kl}[|\mathbf{r} - \mathbf{r}'|] \quad \text{for } k, l \in \mathcal{A}, \mathcal{B} \quad (\text{A.22})$$





# Appendix B

## Mathematical identities and special functions

### B.1 Identities

Gauss's theorem:

$$\int_V (\nabla \cdot \mathbf{F}) dV = \oint_S \mathbf{F} \cdot d\mathbf{a} \quad (\text{B.1})$$

Gradient  $\nabla$  in spherical coordinates:

$$\nabla f = \frac{\partial f}{\partial r} \hat{\mathbf{r}} + \frac{1}{r} \frac{\partial f}{\partial \theta} \hat{\theta} + \frac{r}{r \sin \theta} \frac{\partial f}{\partial \phi} \hat{\phi} \quad (\text{B.2})$$

Laplacian  $\nabla^2$  in spherical coordinates:

$$\nabla^2 f = \frac{1}{r^2} \frac{\partial}{\partial r} \left( r^2 \frac{\partial f}{\partial r} \right) + \frac{1}{r^2 \sin \theta} \frac{\partial}{\partial \theta} \left( \sin \theta \frac{\partial f}{\partial \theta} \right) + \frac{1}{r^2 \sin^2 \theta} \frac{\partial^2 f}{\partial \phi^2} \quad (\text{B.3})$$

Note that 
$$\frac{1}{r^2} \frac{\partial}{\partial r} \left( r^2 \frac{\partial f}{\partial r} \right) = \frac{1}{r} \frac{\partial^2}{\partial r^2} (rf)$$

Hyperbolic functions:

$$\begin{aligned} \cosh[x] - 1 &\equiv \frac{e^x + e^{-x}}{2} - 1 = \frac{1}{2} (e^x + e^{-x} - 2) = \frac{1}{2} (e^{\frac{x}{2}} - e^{-\frac{x}{2}})^2 = 2 \left( \frac{e^{\frac{x}{2}} - e^{-\frac{x}{2}}}{2} \right)^2 \\ &\equiv 2 \sinh^2 \left[ \frac{x}{2} \right] \end{aligned} \quad (\text{B.4})$$

### B.2 Special functions

Error function:

$$\text{erf}[z] \equiv \frac{2}{\sqrt{\pi}} \int_0^z \exp[-t^2] dt \quad \text{for } z \in \mathbb{C} \quad (\text{B.5})$$

Imaginary error function:

$$\operatorname{erfi}[z] \equiv \frac{\operatorname{erf}[\imath z]}{\imath} = \frac{2}{\imath\sqrt{\pi}} \int_0^{\imath z} \exp[-t^2] dt = \frac{2}{\sqrt{\pi}} \int_0^z \exp[t^2] dt \quad \text{for } z \in \mathbb{C} \quad (\text{B.6})$$

# Appendix C

## Derivations

### C.1 Solving the spherically symmetric linear Poisson-Boltzmann equation

The linear differential equation

$$\nabla^2 \psi[r] = \kappa^2 \psi[r] \quad (\text{C.1})$$

with  $\psi[r]$  depending only on the radial component  $r$ , can be solved by writing out the Laplacian using equation (B.3) and discarding the angular terms:

$$\frac{1}{r} \frac{\partial^2}{\partial r^2} (r\psi[r]) = \kappa^2 \psi[r]. \quad (\text{C.2})$$

Defining  $f(r) \equiv r\psi(r)$  we have reduced the problem to:

$$\frac{\partial^2 f[r]}{\partial r^2} = \kappa^2 f[r], \quad (\text{C.3})$$

which has the solution:

$$f[r] = c_1 \exp[\kappa r] + c_2 \exp[-\kappa r]. \quad (\text{C.4})$$

Therefore we find the general solution of equation (C.1) to be:

$$\psi[r] = \frac{c_1 \exp[\kappa r] + c_2 \exp[-\kappa r]}{r}. \quad (\text{C.5})$$

### C.2 Partition function derived from microscopic level

The microscopic atoms or molecules within the colloidal particles have masses  $\mu_{ij}$ , positions  $\rho_{ij}$  and momenta  $\pi_{ij}$ , where  $i$  denotes the colloid they are part of. The same properties for

mesoscopic colloids are defined as:

$$m_i \equiv \sum_{j \in \mathcal{M}_i} \mu_{ij} \quad (\text{C.6})$$

$$\mathbf{r}_i \equiv \sum_{j \in \mathcal{M}_i} \frac{\mu_{ij}}{m_i} \rho_{ij} \quad (\text{C.7})$$

$$\mathbf{p}_i \equiv \sum_{j \in \mathcal{M}_i} \pi_{ij}. \quad (\text{C.8})$$

Here  $\mathcal{M}_i \equiv \{1, 2, \dots, M_i\}$  is the set of microscopic particles within colloid  $i$  and we define  $\mathcal{M} \equiv \{(i, j) | i \in \mathcal{N}, j \in \mathcal{M}_i\}$  as the set of all these particles, whose total number is denoted by  $M \equiv \sum_{i \in \mathcal{N}} M_i$ .

The complete Hamiltonian is now expressed as:

$$H = \underbrace{\sum_{i \in \mathcal{N}} \frac{\mathbf{p}_i^2}{2m_i} + U[\{\mathbf{r}\}_{\mathcal{N}}]}_{\text{colloids}} + \underbrace{\sum_{i \in \mathcal{N}} \sum_{j \in \mathcal{M}_i} \frac{\left(\pi_{ij} - \frac{\mu_{ij}}{m_i} \mathbf{p}_i\right)^2}{2\mu_{ij}} + \sum_{i \in \mathcal{N}} U_{\text{int}}[\{\rho\}_{\mathcal{M}_i}]}_{\text{internal atoms}} \quad (\text{C.9})$$

where the first two terms constitute the kinetic and potential energies of the macroscopic colloids and the latter two terms are the internal energies of the microscopic atoms or molecules within the colloids. Salt ions and solvent molecules have already been included in the colloid-colloid pair potential by the DLVO theory (see chapter 2).

From the Hamiltonian we obtain the canonical partition function:

$$Z = \frac{1}{h^{3M}} \int d\pi^{\mathcal{M}} \exp \left[ -\beta \sum_{i \in \mathcal{N}} \frac{\mathbf{p}_i^2}{2m_i} - \beta \sum_{i \in \mathcal{N}} \sum_{j \in \mathcal{M}_i} \frac{\left(\pi_{ij} - \frac{\mu_{ij}}{m_i} \mathbf{p}_i\right)^2}{2\mu_{ij}} \right] \\ \times \int d\rho^{\mathcal{M}} \exp \left[ -\beta U[\{\mathbf{r}\}_{\mathcal{N}}] - \beta \sum_{i \in \mathcal{N}} U_{\text{int}}[\{\rho\}_{\mathcal{M}_i}] \right] \quad (\text{C.10})$$

where we have to keep in mind that the  $\mathbf{m}_i$  and  $\rho_i$  still depend on the integration variables.

The internal potential energy  $U_{\text{int}}[\{\rho\}_{\mathcal{M}_i}]$  is invariant under translations of the whole colloid and depends only on the  $M_i - 1$  *relative* positions of the internal particles. By expressing these as  $\rho'_{ij} \equiv \rho_{ij} - \rho_{i1}$  for  $j \in \tilde{\mathcal{M}}_i \equiv \{2, 3, \dots, M_i\}$  and performing a change of variables  $\rho_{i1}, \rho_{i2}, \dots, \rho_{iM_i} \rightarrow \mathbf{r}_i, \rho'_{i2}, \dots, \rho'_{iM_i}$  for each  $i \in \mathcal{N}$ , we are able to integrate out the internal degrees of freedom. The Jacobian belonging to this transformation equals  $J_i^{(r)} = \left| \frac{\partial(\mathbf{r}_i, \rho'_{i2}, \dots, \rho'_{iM_i})}{\partial(\rho_{i1}, \dots, \rho_{iM_i})} \right| = \dots = \left( \sum_{j \in \mathcal{M}_i} \frac{\mu_{ij}}{m_i} \right)^3 = 1$ .

We use a similar change of variables  $\pi_{i1}, \pi_{i2}, \dots, \pi_{iM_i} \rightarrow \mathbf{p}_i, \pi'_{i2}, \dots, \pi'_{iM_i}$  for the momenta, with  $\pi'_{ij} \equiv \pi_{ij} - \frac{\mu_{ij}}{m_i} \mathbf{p}_i$  for  $j \in \tilde{\mathcal{M}}_i$ . Again, the associated Jacobian turns out to be  $J_i^{(p)} = \left| \frac{\partial(\mathbf{p}_i, \pi'_{i2}, \dots, \pi'_{iM_i})}{\partial(\pi_{i1}, \dots, \pi_{iM_i})} \right| = \dots = |(-1)^{j-1}| = 1$ .

Integrating out these degrees of freedom and evaluating the (macroscopic) momentum integral gives us:

$$\begin{aligned}
Z &= \frac{1}{h^{3N}} \int d\mathbf{p}^{\mathcal{N}} \exp \left[ -\beta \sum_{i \in \mathcal{N}} \frac{\mathbf{p}_i^2}{2m_i} \right] \int d\mathbf{r}^{\mathcal{N}} \exp[-\beta U[\{\mathbf{r}\}_{\mathcal{N}}]] \\
&\quad \times \frac{1}{h^{3(M-N)}} \int d\pi^{\tilde{\mathcal{M}}} \exp \left[ -\beta \sum_{i \in \mathcal{N}} \sum_{j \in \tilde{\mathcal{M}}_i} \frac{(\pi'_{ij})^2}{2\mu_{ij}} - \beta \sum_{i \in \mathcal{N}} \frac{\left( \sum_{j \in \tilde{\mathcal{M}}_i} \pi'_{ij} \right)^2}{2\mu_{i1}} \right] \\
&\quad \times \int d\rho^{\tilde{\mathcal{M}}} \exp \left[ -\beta \sum_{i \in \mathcal{N}} U_{\text{int}}[\{\rho'\}_{\tilde{\mathcal{M}}_i}] \right] \\
&= \frac{\exp[-\beta F_{\text{int}}]}{(\Lambda^*)^{3N}} \int d\mathbf{r}^{\mathcal{N}} \exp[-\beta U[\{\mathbf{r}\}_{\mathcal{N}}]], \tag{C.11}
\end{aligned}$$

where we used  $\tilde{\mathcal{M}} \equiv \{(i, j) | i \in \mathcal{N}, j \in \tilde{\mathcal{M}}_i\}$  for simpler notations, such that the  $d\pi^{\tilde{\mathcal{M}}}$ - and  $d\rho^{\tilde{\mathcal{M}}}$ -integrals are done over  $M - N$  (vectorial) variables. These two integrals are now replaced by the internal partition sum  $Z_{\text{int}} = \exp[-\beta F_{\text{int}}]$ . The  $d\mathbf{p}^{\mathcal{N}}$  integral is evaluated with  $(\Lambda^*)^{3N} \equiv \prod_{i \in \mathcal{N}} \left( \frac{h}{2\pi m_i k_B T} \right)^{3/2}$  as a result. Note that degenerate masses  $m_1 = m_2 = m$  cause  $\Lambda^*$  to be reduced to the normal thermal wavelength  $\Lambda \equiv \sqrt{\frac{h}{2\pi m k_B T}}$ . We see that the internal degrees of freedom only add a constant  $F_{\text{int}}$  to the free energy without actually changing the physics of the system, which is not surprising.

## C.3 Symmetric version of Ffluid3

### Symmetric case: Ffluid1

We now work out the Helmholtz free energy of a colloidal fluid consisting of equal but oppositely charged colloids, i.e. the symmetric case ( $N_1 = N_2 = N/2$ ;  $Z_1 = -Z_2 = Z$ ;  $a_1 = a_2 = a$ ), based on equation (4.44). This section therefore elaborates on subsection 4.1.2.3.

Using the fact that in the symmetric case  $\phi_{++}^{\text{DLVO}} = \phi_{--}^{\text{DLVO}} = -\phi_{+-}^{\text{DLVO}} = -\phi_{-+}^{\text{DLVO}} \equiv \phi$ ) we get

$$\left. \begin{aligned} g_{\lambda}^{++}[r] &= g_{\lambda}^{--}[r] = \exp[-\lambda\beta\phi[r]] \\ g_{\lambda}^{+-}[r] &= g_{\lambda}^{-+}[r] = \exp[+\lambda\beta\phi[r]] \end{aligned} \right\} \quad \text{for } r \geq 2a \tag{C.12}$$

$$g_{\lambda}^{++}[r] = g_{\lambda}^{--}[r] = g_{\lambda}^{+-}[r] = g_{\lambda}^{-+}[r] = 0 \quad \text{for } r < 2a \tag{C.13}$$

which leads to:

$$\begin{aligned}
\beta F^{\text{DLVO}} &= \frac{V}{2} \sum_{i,j=+,-} \rho_i \rho_j \int_0^1 d\lambda \int d\mathbf{r} g_{\lambda}^{ij}[\mathbf{r}] \beta \phi_{ij}^{\text{DLVO}}[\mathbf{r}] \\
&= \frac{V \rho^2}{4} \int_0^1 d\lambda \int d\mathbf{r} (g_{\lambda}^{++}[r] - g_{\lambda}^{+-}[r]) \beta \phi[r] \\
&= \frac{V \rho^2}{4} \int_0^1 d\lambda \int_{|\mathbf{r}| \geq 2a} d\mathbf{r} (-2 \sinh[\lambda \beta \phi[r]]) \beta \phi[r] \\
&= -\frac{V \rho^2}{2} \int_0^1 d\lambda \int_{2a}^{\infty} dr 4\pi r^2 \beta \phi[r] \sinh[\lambda \beta \phi[r]] \\
&= -2\pi V \rho^2 \int_{2a}^{\infty} dr r^2 \beta \phi[r] \left[ \frac{\cosh[\lambda \beta \phi[r]]}{\beta \phi[r]} \right]_{\lambda=0}^{\lambda=1} \\
&= -2\pi V \rho^2 \int_{2a}^{\infty} dr r^2 (\cosh[\beta \phi[r]] - 1) \\
&= -4\pi V \rho^2 \int_{2a}^{\infty} dr r^2 \sinh^2 \left[ \frac{\beta \phi[r]}{2} \right], \tag{C.14}
\end{aligned}$$

where we made use of identity (B.4) in the last step and  $\rho_i = \rho_j = \rho/2$  due to the symmetric case constraint. Combining these calculations we see that the general expression (4.44) evaluates to:

$$\boxed{\frac{\beta F^{\text{(fluid1)}}}{N} = \log[\rho \Lambda^3] - 1 - \log[2] + \frac{4\eta - 3\eta^2}{(1 - \eta)^2} - 4\pi \rho \int_{2a}^{\infty} dr r^2 \sinh^2 \left[ \frac{\beta \phi[r]}{2} \right]}. \tag{C.15}$$

### Linearized version of Ffluid1: Ffluid1a

Expression (C.15) can be simplified a little further by linearizing the sinh function for sufficiently high temperatures, as we will now show. From the definition of the reduced temperature  $T^* \equiv \frac{(1+\kappa a)^2 2a}{Z^2 \lambda_B}$  in equation (4.50) we notice that

$$\beta \phi[2a] = Z^2 \lambda_B \left( \frac{\exp[\kappa a]}{1 + \kappa a} \right)^2 \frac{\exp[-\kappa(2a)]}{2a} = \frac{Z^2 \lambda_B}{(1 + \kappa a)^2 2a} \equiv \frac{1}{T^*}, \tag{C.16}$$

in other words that  $T^*$  is the inverse contact potential of 2 particles of the same species. This poses a clear boundary for  $\beta \phi$ :

$$0 \leq \beta \phi[r] \leq \frac{1}{T^*} \quad \text{for } r \geq 2a, \tag{C.17}$$

meaning that the condition  $T^* \gg 1/2$  provides sufficient accuracy for this linearization,

resulting in:

$$\begin{aligned} \int_{2a}^{\infty} dr \, r^2 \sinh^2 \left[ \frac{\beta\phi[r]}{2} \right] &\approx \frac{1}{4} \int_{2a}^{\infty} dr \, r^2 (\beta\phi[r])^2 = \frac{1}{4} \int_{2a}^{\infty} dr \, r^2 \left( (Z^*)^2 \lambda_B \frac{\exp[-\kappa r]}{r} \right)^2 \\ &= \frac{(Z^*)^4 \lambda_B^2}{4} \left[ \frac{\exp[-2\kappa r]}{-2\kappa} \right]_{r=2a}^{r \rightarrow \infty} = \frac{(Z^*)^4 \lambda_B^2}{8\kappa} \exp[-4\kappa a] = \frac{\lambda_B^2}{8\kappa} \left( \frac{Z}{1 + \kappa a} \right)^4. \end{aligned} \quad (\text{C.18})$$

Plugging this into equation (C.15) we arrive at:

$$\boxed{\frac{\beta F^{(\text{fluid1a})}}{N} = \log[\rho\Lambda^3] - 1 - \log[2] + \frac{4\eta - 3\eta^2}{(1 - \eta)^2} - \frac{\pi\rho\lambda_B^2}{2\kappa} \left( \frac{Z}{1 + \kappa a} \right)^4} \quad \text{for } T^* \gg \frac{1}{2}. \quad (\text{C.19})$$

## C.4 Truncated Boltzmann factor

As we found out that  $F_{\text{fluid}}^{(3)}$  gives unphysically high values for  $g_{ij}[r]$  at low temperature and small  $r$ , we devised an alternative method for  $F_{\text{fluid}}$  based on truncating this  $g[r]$  for these circumstances. We now look at equal sized particles ( $a_1 = a_2 \equiv a$ ), but charges are allowed to be unequal.

$$\beta F_{\text{fluid}}^{(4)} = \beta F_{\text{fluid}}^{\text{HS}} + V \sum_{k,l} \rho_k \rho_l B_{kl}[\eta] \quad (\text{C.20})$$

where:

$$B_{kk}[\eta] = B_{kk} = -2\pi \int_{2a}^{\infty} dr \, r^2 (\exp[-\beta V_{kk}[r]] - 1) \quad (\text{C.21})$$

For  $k \neq l$ :

$$B_{kl}[\eta] = \begin{cases} -2\pi \int_{2a}^{\infty} dr \, r^2 (\exp[-\beta V_{kl}[r]] - 1) & \text{for } \tilde{Q}_k \leq 12 \\ -2\pi \int_{4a}^{\infty} dr \, r^2 (\exp[-\beta V_{kl}[r]] - 1) + 2\pi \int_{2a}^{4a} dr \, r^2 \beta V_{kl}[r] \left( \frac{g_{kl}^*[\eta] - 1}{\log[g_{kl}^*[\eta]]} \right) & \text{for } \tilde{Q}_k > 12 \end{cases} \quad (\text{C.22})$$

with (still for  $k \neq l$ ):

$$g_{kl}^*[\eta] = \frac{3}{28\pi(2a)^3} \frac{1}{1-x} \left( \frac{12\tilde{v}}{\eta} - x\tilde{G}_{kk} \right) \quad (\text{C.23})$$

$$\tilde{G}_{kk} = 4\pi \int_{2a}^{4a} dr \, r^2 \exp[-\beta V_{kk}[r]] \quad (\text{C.24})$$

## C.5 Better Ansatz

Using the ‘Better Ansatz’ for the pair correlation functions:

$$g^{ij}[r] = \frac{2 \exp[-\beta \phi_{ij}^{\text{DLVO}}]}{\exp[-\beta \phi_{i+}^{\text{DLVO}}] + \exp[-\beta \phi_{i-}^{\text{DLVO}}]} g^{\text{HS}}[r] \quad (\text{C.25})$$

might give us a better approximation for the real correlation functions compared to 4.42, which was used in the derivation of  $F_{\text{fluid}}^{(3)}$ . Note that we again defined it such that  $\lim_{r \rightarrow \infty} g^{ij}[r] = 1$  because of  $\lim_{r \rightarrow \infty} \phi_{ij}^{\text{DLVO}}[r] = 0$  and  $\lim_{r \rightarrow \infty} g^{\text{HS}}[r] = 1$ .

We now get (still for the symmetric case):

$$g_{\lambda}^{++}[r] = g_{\lambda}^{--}[r] = \frac{2 \exp[-\lambda \beta \phi_{++}^{\text{DLVO}}[r]]}{\exp[-\lambda \beta \phi_{++}^{\text{DLVO}}[r]] + \exp[-\lambda \beta \phi_{+-}^{\text{DLVO}}[r]]} g^{\text{HS}}[r] = \frac{\exp[-\lambda \beta \phi[r]]}{\cosh[\lambda \beta \phi[r]]} g^{\text{HS}}[r] \quad (\text{C.26})$$

$$g_{\lambda}^{+-}[r] = g_{\lambda}^{-+}[r] = \frac{\exp[+\lambda \beta \phi[r]]}{\cosh[\lambda \beta \phi[r]]} g^{\text{HS}}[r] \quad (\text{C.27})$$

Knowing that  $g^{\text{HS}}[r] = 0$  for  $r < 2a$  we find:

$$\begin{aligned} \beta F^{\text{DLVO}} &= \frac{V}{2} \sum_{i,j=+,-} \rho_i \rho_j \int_0^1 d\lambda \int d\mathbf{r} g_{\lambda}^{ij}[r] \beta \phi_{ij}^{\text{DLVO}}[r] \\ &= \frac{V \rho^2}{8} \int_0^1 d\lambda \int d\mathbf{r} (2g_{\lambda}^{++}[r] - 2g_{\lambda}^{+-}[r]) \beta \phi[r] \\ &= \frac{V \rho^2}{4} \int_0^1 d\lambda \int d\mathbf{r} \frac{\exp[-\lambda \beta \phi[r]] - \exp[+\lambda \beta \phi[r]]}{\cosh[\lambda \beta \phi[r]]} g^{\text{HS}}[r] \beta \phi[r] \\ &= -\frac{V \rho^2}{2} \int_0^1 d\lambda \int d\mathbf{r} \tanh[\lambda \beta \phi[r]] g^{\text{HS}}[r] \beta \phi[r] \\ &= -\frac{V \rho^2}{2} \int d\mathbf{r} g^{\text{HS}}[r] \left[ \log[\cosh[\lambda \beta \phi[r]]] \right]_{\lambda=0}^{\lambda=1} \\ &= -\frac{V \rho^2}{2} \int_{|\mathbf{r}| \geq 2a} d\mathbf{r} g^{\text{HS}}[r] \log[\cosh[\beta \phi[r]]] \\ &= -2\pi V \rho^2 \int_{2a}^{\infty} dr r^2 g^{\text{HS}}[r] \log[\cosh[\beta \phi[r]]]. \end{aligned} \quad (\text{C.28})$$

A (failed) attempt to work this out analytically leads to the following.

Because we do not know  $g^{\text{HS}}[r]$  analytically we could integrate equation(C.28) numerically. But it is possible to determine its Fourier transform  $\hat{g}^{\text{HS}}[k]$  though, so we use:

$$g^{\text{HS}}[r] = \frac{1}{(2\pi)^3} \int d\mathbf{k} \hat{g}^{\text{HS}}[\mathbf{k}] \exp[i\mathbf{k} \cdot \mathbf{r}] = \dots = \frac{1}{2\pi^2 r} \int_0^{\infty} dk k \hat{g}^{\text{HS}}[k] \sin[kr] \quad (\text{C.29})$$



such that we get:

$$\begin{aligned}
\beta F^{\text{DLVO}} &= -\frac{V\rho^2}{\pi} \int_{2a}^{\infty} dr \, r \int_0^{\infty} dk \, k \, \hat{g}^{\text{HS}}[k] \sin[kr] \log [\cosh [\beta\phi[r]]] \\
&= -\frac{V\rho^2}{\pi} \int_0^{\infty} dk \, \hat{g}^{\text{HS}}[k] \left( k \int_{2a}^{\infty} dr \, r \log [\cosh [\beta\phi[r]]] \sin[kr] \right) \\
&= -4V\rho^2 \int_0^{\infty} dk \, \hat{g}^{\text{HS}}[k] \mathcal{F} [\log [\cosh [\beta\phi[r]]]] [k].
\end{aligned} \tag{C.30}$$

However, so far I have not been able to calculate the Fourier transform in eqn. (C.30).

Another option is to keep the  $\lambda$ -integral and first do the  $\mathbf{r}$ -integral:

$$\begin{aligned}
\beta F^{\text{DLVO}} &= -\frac{V\rho^2}{2} \int_0^1 d\lambda \int_{|\mathbf{r}| \geq 2a} d\mathbf{r} \tanh [\lambda\beta\phi[r]] g^{\text{HS}}[r] \beta\phi[r] \\
&= -\frac{V\rho^2}{2} \int_0^1 d\lambda \int_{2a}^{\infty} dr \, 4\pi r^2 \tanh [\lambda\beta\phi[r]] g^{\text{HS}}[r] \beta\phi[r] \\
&= -2\pi V\rho^2 \int_0^1 d\lambda \int_{2a}^{\infty} dr \, r^2 \beta\phi[r] \tanh [\lambda\beta\phi[r]] \left( \frac{1}{2\pi^2 r} \int_0^{\infty} dk \, k \, \hat{g}^{\text{HS}}[k] \sin[kr] \right) \\
&= -2\pi V\rho^2 \int_0^1 d\lambda \int_{2a}^{\infty} dr \, r^2 \beta\phi[r] \tanh [\lambda\beta\phi[r]] \left( \frac{1}{2\pi^2 r} \int_0^{\infty} dk \, k \, \hat{g}^{\text{HS}}[k] \sin[kr] \right) \\
&= -\frac{V\rho^2 (Z^*)^2 \lambda_B}{\pi} \int_0^1 d\lambda \int_0^{\infty} dk \, \hat{g}^{\text{HS}}[k] k \int_{2a}^{\infty} dr \exp[-\kappa r] \tanh \left[ \lambda (Z^*)^2 \lambda_B \frac{\exp[-\kappa r]}{r} \right] \sin[kr].
\end{aligned} \tag{C.31}$$

So to determine  $\beta F^{\text{DLVO}}$  analytically for the 'Better Ansatz' we have to solve one of the integrals A and B:

$$A = \int_{2a}^{\infty} dr \, r \log \left[ \cosh \left[ \alpha \frac{\exp[-\kappa r]}{r} \right] \right] \sin[qr] = \dots \quad ? \tag{C.32}$$

$$B = \int_{2a}^{\infty} dr \exp[-\kappa r] \tanh \left[ \alpha \frac{\exp[-\kappa r]}{r} \right] \sin[qr] = \dots \quad ? \tag{C.33}$$

but this is not really an option.

It therefore seems that the only reasonable choice is to determine  $g^{\text{HS}}[r]$  numerically and use:

$$\boxed{\frac{\beta F_{\text{fluid}}^{(2)}}{N} = \log[\rho\Lambda^3] - 1 - \log[2] + \frac{4\eta - 3\eta^2}{(1 - \eta)^2} - 2\pi\rho \int_{2a}^{\infty} dr \, r^2 g^{\text{HS}}[r] \log [\cosh [\beta\phi[r]]]} \tag{C.34}$$

to compute  $\beta F$ .



# Appendix D

## Mansoori potential

The Mansoori potential is a generalized version of the Carnahan-Starling expression, namely for 2 species of hard spheres with different radii [38]:

$$\begin{aligned} \frac{\beta F^{(\text{BMCSL})}}{N} = & \log[\rho\Lambda^3] - 1 + x_{\text{mix}} \log[x_{\text{mix}}] + (1 - x_{\text{mix}}) \log[1 - x_{\text{mix}}] \\ & - \frac{3}{2}(1 - y_1 + y_2 + y_3) + \frac{3y_2 + 2y_3}{1 - \eta} + \frac{3}{2} \frac{1 - y_1 - y_2 - y_3/3}{(1 - \eta)^2} + (y_3 - 1) \log[1 - \eta] \end{aligned} \quad (\text{D.1})$$

$$\text{with } \eta_1 = \frac{4\pi a_1^3}{3} \rho x_{\text{mix}} \quad (\text{D.2})$$

$$\eta_2 = \frac{4\pi a_2^3}{3} \rho (1 - x_{\text{mix}}) \quad (\text{D.3})$$

$$\delta_{12} = \frac{\sqrt{\eta_1 \eta_2 x_{\text{mix}} (1 - x_{\text{mix}})}}{\eta} \frac{(a_1 - a_2)^2}{a_1 a_2} \quad (\text{D.4})$$

$$y_1 = \delta_{12} \frac{a_1 + a_2}{\sqrt{a_1 a_2}} \quad (\text{D.5})$$

$$y_2 = \delta_{12} \frac{\sqrt{a_1 a_2}}{\eta} \left( \frac{\eta_1}{a_1} + \frac{\eta_2}{a_2} \right) \quad (\text{D.6})$$

$$y_3 = \left( \frac{\eta_1^{2/3} x_{\text{mix}}^{1/3} + \eta_2^{2/3} (1 - x_{\text{mix}})^{1/3}}{\eta^{2/3}} \right)^3 \quad (\text{D.7})$$



# Bibliography

- [1] D.R. Hofstadter. *Gödel, Escher, Bach: An Eternal Golden Braid*. Basic Books, 1980.
- [2] W.B. Russel, D.A. Saville, and W.R. Schowalter. *Colloidal Dispersions*. Cambridge University Press, 1992.
- [3] A. van Blaaderen. Colloids get complex. *Nature*, 439:545, 2006.
- [4] D. Frenkel. Plenty of room at the top. *Nature Mater.*, 5:85, 2006.
- [5] Y.-H. Ye, F. LeBlanc, A. Haché, and V.-V. Truong. Self-assembling three-dimensional colloidal photonic crystal structure with high crystalline quality. *Appl. Phys. Lett.*, 78:52, 2001.
- [6] A.-P. Hynninen, J.H.J. Thijssen, E.C.M. Vermolen, M. Dijkstra, and A. van Blaaderen. Self-assembly route for photonic crystals with a bandgap in the visible region. *Nature*, 6:202, 2007.
- [7] P.N. Pusey and W. van Megen. Phase behaviour of concentrated suspensions of nearly hard colloidal spheres. *Nature*, 320:340, 1986.
- [8] A.D. Dinsmore, A.G. Yodh, and D.J. Pine. Phase diagrams of nearly hard-sphere binary colloids. *Phys. Rev. E (3)*, 52:4045, 1995.
- [9] A. Yethiraj and A. van Blaaderen. A colloidal model system with an interaction tunable from hard sphere to soft and dipolar. *Nature*, 421:513, 2003.
- [10] F. Sciortino, S. Mossa, E. Zaccarelli, and P. Tartaglia. Equilibrium cluster phases and low-density arrested disordered states: The role of short-range attraction and long-range repulsion. *Phys. Rev. E (3)*, 93:055701, 2004.
- [11] K.N. Pham, A.M. Puertas, J. Bergenholtz, S.U. Egelhaaf, A. Moussaïd, P.N. Pusey, A.B. Schofield, M.E. Cates, M. Fuchs, and W.C.K. Poon. Multiple glassy states in a simple model system. *Science*, 296:104, 2002.

- [12] A.M. Islam, B.Z. Chowdhry, and M.J. Snowden. Heteroaggregation in colloidal dispersions. *Adv. Colloid Interface Sci.*, 62:109, 1995.
- [13] M.E. Leunissen, C.G. Christova, A.-P. Hynninen, C.P. Royall, A.I. Campbell, A. Imhof, M. Dijkstra, R. van Roij, and A. van Blaaderen. Ionic colloidal crystals of oppositely charged particles. *Nature*, 437:235, 2005.
- [14] P. Bartlett and A.I. Campbell. Three-dimensional binary superlattices of oppositely charged colloids. *Phys. Rev. Lett.*, 95:128302, 2005.
- [15] A.-P. Hynninen, A. van Blaaderen M.E. Leunissen, and M. Dijkstra. CuAu structure in the restricted primitive model and oppositely charged colloids. *Phys. Rev. Lett.*, 96:018303, 2006.
- [16] A.-P. Hynninen, C.G. Christova, R. van Roij, A. van Blaaderen, and M. Dijkstra. Prediction and observation of crystal structures of oppositely charged colloids. *Phys. Rev. Lett.*, 96:138308, 2006.
- [17] A.-P. Hynninen. *Phase Behaviour of Charged Colloids and the Effect of External Fields*. PhD thesis, Utrecht University, Utrecht, 2005.
- [18] G.R. Maskaly. *Attractive Electrostatic Self-Assembly of Ordered and Disordered Heterogeneous Colloids*. PhD thesis, MIT, Boston, 2005.
- [19] G.R. Maskaly, R.E. García, W. C. Carter, and Y.-M. Chiang. Ionic colloidal crystals: Ordered, multicomponent structures via controlled heterocoagulation. *Phys. Rev. E (3)*, 73:011402, 2006.
- [20] G. Bryant, S. R. Williams, L. Qian, I. K. Snook, E. Perez, and F. Pincet. How hard is a colloidal hard-sphere interaction? *Phys. Rev. E (3)*, 66:060501, 2002.
- [21] Z. Cheng, P.M. Chaikin, J. Zhu, W. B. Russel, and W.V. Meyer. Crystallization kinetics of hard spheres in microgravity in the coexistence regime: Interactions between growing crystallites. *Phys. Rev. Lett.*, 88:015501, 2002.
- [22] B. Derjaguin and L. Landau. Theory of the stability of strongly charged lyophobic sols and of the adhesion of strongly charged particles in solution of electrolytes. *Acta Physicochim. URSS*, 14:633, 1941.
- [23] E.J.W. Verwey and J.T.G. Overbeek. *Theory of the Stability of Lyophobic Colloids*. Elsevier, Amsterdam, 1948.
- [24] R. Hogg, T.W. Healy, and D.W. Fürstenau. Mutual coagulation of colloidal dispersions. *Trans. Faraday Soc.*, 62:1938, 1966.
- [25] G.R. Wiese and T.W. Healy. Effect of particle size on colloid stability. *Trans. Faraday Soc.*, 66:490, 1970.

- [26] A.-P. Hynninen, M. Dijkstra, and R. van Roij. Effect of three-body interactions on the phase behavior of charge-stabilized colloidal suspensions. *Phys. Rev. E* (3), 69:061407, 2004.
- [27] P.E. Dyshlovenko. Evidence of many-particle interactions in two-dimensional charge-stabilized colloidal crystals. *Phys. Rev. Lett.*, 95:038302, 2005.
- [28] D. Reinke. Comment on “evidence of many-particle interactions in two-dimensional charge-stabilized colloidal crystals”. *Phys. Rev. E* (3), 97:119801, 2006.
- [29] N.W. Ashcroft and N.D. Mermin. *Solid State Physics*. Holt, Rinehart and Winston, 1976.
- [30] U.S. Naval Research Laboratory Center for Computational Materials Science. Database of crystal lattice structures. <http://cst-www.nrl.navy.mil/lattice/>.
- [31] R.M. Fleming, M.J. Rosseinsky, A.P. Ramirez, D.W. Murphy, J.C. Tully, R.C.Haddon, T. Siegrist, R. Tycko, S.H. Glarum, P. Marsh, G. Dabbagh, S.M. Zahurak, A.V. Makhija, and C. Hampton. Preparation and structure of the alkali-metal fulleride  $A_4C_{60}$ . *Nature*, 352:701, 1991.
- [32] L. Forró and L. Mihály. Electronic properties of doped fullerenes. *Rep. Progr. Phys.*, 64:649, 2001.
- [33] T. Yildirim, O. Zhou, J.E. Fischer, N. Bykovetz, R.A. Strongin, M.A. Cichy, A.B. Smith III, C.L. Lin, and R. Jelinek. Intercalation of sodium heteroclusters into the  $C_{60}$  lattice. *Nature*, 360:568, 1992.
- [34] W.B. Pearson. *The crystal chemistry and physics of metals and alloys*. John Wiley & Sons, 1972.
- [35] M. Dijkstra. Phase behavior of hard spheres with a short-range yukawa attraction. *Phys. Rev. E* (3), 66:021402, 2002.
- [36] L. Pauling. *The Nature of the Chemical Bond and the Structure of Molecules and Crystals: An Introduction to Modern Structural Chemistry*. Cornell University Press, third edition, 1960.
- [37] N.F. Carnahan and K.E. Starling. Equation of state for nonattracting rigid spheres. *J. Chem. Phys.*, 51(2):635, 1969.
- [38] G.A. Mansoori, N.F. Carnahan, K.E. Starling, and T.W. Leland. Equilibrium thermodynamic properties of the mixture of hard spheres. *J. Chem. Phys.*, 54:1523, 1971.
- [39] F.A. Lindemann. The calculation of molecular vibration frequencies. *Phys. Z.*, 11:609, 1910.

- 
- [40] A. Fortini, A.-P. Hynninen, and M. Dijkstra. Gas-liquid phase separation in oppositely charged colloids: Stability and interfacial tension. *J. Chem. Phys.*, 125:094502, 2006.
  - [41] R.J.F. Leote de Carvalho and R. Evans. The screened Coulomb (Yukawa) charged hard sphere binary fluid. *Molecular Phys.*, 92:211, 1997.
  - [42] M.H.J. Hagen and D. Frenkel. Determination of phase diagrams for the hard-core attractive yukawa system. *J. Chem. Phys.*, 101:4093, 1994.
  - [43] O.D. Velev and A.M. Lenhoff. Colloidal crystals as templates for porous materials. *Current Opinion Colloid Interface Sci.*, 5:56–63, 2000.
  - [44] M. Yanagioka and C.W. Frank. Structure, stability and applications of colloidal crystals. *Korea-Australia Rheology J.*, 20(3), 2008.
  - [45] J. Lee, S. Shanbhag, and N.A. Kotov. Inverted colloidal crystals as three-dimensional microenvironments for cellular co-cultures. *J. Mater. Chem.*, 16:3558, 2006.
  - [46] S. Pautot, C. Wyart, and E.Y. Isacoff. Colloid-guided assembly of oriented 3d neuronal networks. *Nature Methods*, 5(8):735, 2008.